Swan, Shona (2025) Modelling the dynamic distribution of geochemical signatures in shallow continental magma bodies. MSc(R) thesis.

https://theses.gla.ac.uk/85254/

Modelling the Dynamic Distribution of Geochemical Signatures in Shallow Continental Magma Bodies

Shona Swan
BSc(Hons) University of Glasgow

June 2, 2025

Abstract

Continental arcs are critical geological settings due to their role in recycling the Earth's crust through subduction and magma generation. These regions are characterised by intense volcanic activity and host some of the world's largest ore deposits. Extensive studies of continental arcs have produced large geochemical databases and widely accepted conceptual models. Despite this wealth of data, there is still ongoing debate within the literature on which processes are the dominant control on the diverse range of geochemical signatures observed in continental arcs. This ongoing debate is partially due to these systems being incredibly complex and their spatially and temporally inaccessible nature. This study models the uppermost sections of volcanic plumbing systems, located just below the volcanic edifices, to explore the dynamics that govern magma mixing and fractional crystallisation within these shallow magma bodies. The aim is to understand how these processes affect the geochemical signatures within shallow systems and to determine whether these signatures can be preserved over time. A two-dimensional (2D) computational numerical model was employed to simulate shallow melt-rich magma bodies, tracking fluid dynamics, thermochemical evolution, and geochemical changes. Another objective of this research was to determine if two mixing end-member compositions can be reconstructed after magma mixing and fractionation. Machine learning techniques were utilised to reconstruct the initial input compositions. The results of this study show that the volatile content is the primary control of the system dynamics. Lower volatile contents led to faster crystallisation and cooling, while higher volatile contents in the recharging magma triggered vigorous convection, mixing and homogenising of the initial geochemical signatures. The machine learning analysis revealed that a single overturn event could overwrite the original geochemistry. However, it was possible to backtrack to the original geochemical signatures in the simulations without overturn. This study highlights the importance of numerical modelling for testing hypotheses about active volcanic systems. Numerical modelling combined with machine learning could help improve field sampling strategies by identifying zones where parental geochemical signatures are most likely to be preserved within a system.

Acknowledgements

I would like to express my gratitude to my supervisors, Dr. Tobias Keller, Dr. Antoniette Greta Grima and Dr. Iain Neill for their unwavering support and encouragement throughout this project.

In addition, I extend my thanks to Dr. Joshua Einsle and Prof. Dr. Paul Tackley for granting me access to supercomputer clusters, without which I would not have been able to complete my research.

I am also grateful to Dr. Sammy Griffin, Dr. Paul Eizenhöfer and Fakhri Bintang for their valuable advice and support throughout this project. A special thanks goes to all the members of the PGR office, especially my close friends Chloe, Careen, and Neeve, for their companionship and support.

I must acknowledge my parents, who have supported me immensely throughout my master's degree and career. I also want to recognise my brother Gordon, whose support and computational expertise were invaluable when I faced particularly challenging problems. Thank you to the rest of my amazing family as well.

I am grateful to my friends, who have supported me throughout my master's degree, always providing a good laugh. A special thanks to Cammy.

Finally, thank you to Geoff, Gavin, Andrew, Eric, and Nick, who have filled my year with laughter.

Contents

List of Figures

List of Tables

Chapter 1

Introduction

1.1 Background and Scientific Context

Shallow crustal magma bodies within continental arc settings are dynamic reservoirs situated at the interface between the crustal magmatic system and volcanic plumbing system connecting to the surface. These reservoirs play a crucial role in the formation of economically valuable ore deposits and in fueling volcanic eruptions [Sillitoe, 1972, Tilling, 2009, Pettke et al., 2010, Huber et al., 2019, Chelle-Michou and Rottier, 2021, Park et al., 2021, Popa et al., 2021]. Located in subduction zones, where oceanic crust is recycled into the mantle, these reservoirs contribute to the generation and evolution of diverse magmas [Karlstrom et al., 2010, Park et al., 2021]. As magmas rise through the crust, they may stall and collect in shallow reservoirs, where processes like fractionation, assimilation, recharge, and magma mixing alter their geochemical signatures [Annen et al., 2006].

As shallow magma bodies cool upon contact with surrounding rock, they begin to fractionate, with minerals crystallising and altering the composition of the remaining melt. Interaction with country rock can lead to the assimilation of surrounding geochemical signatures into the magma [Hildreth and Moorbath, 1988, Annen et al., 2006]. Additionally, recharge events, where more primitive magmas from deeper in the volcanic system enter shallow reservoirs, can trigger mixing with existing magmas, causing further geochemical changes [Hildreth and Moorbath, 1988, Annen et al., 2006].

Previous work on continental arcs has considerably increased our understanding of their structure and internal dynamics. Our present knowledge of these systems is derived from a combination of approaches, including geophysical, geochemical, geochronological, and geodynamic studies [Turner and Langmuir, 2015a, Magee et al., 2018, Keller and Suckale, 2019, Contreras-Reyes et al., 2021, Rosenbaum et al., 2021, Zhang and Miller, 2021, Zhao et al., 2021, Mallea-Lillo et al., 2022, Chen et al., 2024, Liu et al., 2024]. Despite the wealth of data, there is still open debate in the literature regarding the relative roles of different processes (magma mixing, assimilation, and fractionation) and reservoirs (subducting slab, mantle wedge, and crust) that lead to the geochemical diversity observed at the surface [Rawson et al., 2016].

Several challenges make the study of these internal processes difficult. Active plumbing systems are not directly observable, and their large spatial scale and long geological timescales add complexity [Gerya, 2022]. We therefore must rely on indirect evidence from geophysical surveys, and field and laboratory evidence from exhumed or erupted rocks [Magee et al., 2018, Zhang and Miller, 2021, Adams, 2022, Cornet et al., 2022, Mallea-Lillo et al., 2022, Oyarzún et al., 2022]. However, these methods have limitations. Geophysical studies do not capture detailed geochemical information or active internal dynamics, and field studies provide limited spatial density due to sampling and time constraints, offering only a snapshot view of a single moment in time. Some zircon dating approaches can distinguish between different facies in plutons; however, these approaches operate at best on 100 kyr timescales, which is well beyond the time frame of volcanic eruption cycles [Michel et al., 2008]

This research addresses this gap by investigating the controlling processes within shallow systems, including fractionation and magma mixing between two magma compositions, using a numerical geodynamic model.

1.1.1 Andean Geology and Tectonic Context

This study focuses on the Andean continental arc. The Andean orogenic system is located along the west coast of South America, where the oceanic Nazca plate is subducted beneath the South America plate [DeCelles et al., 2014]. The Andean orogenic system is subdivided into sections based on variations in tectonics, crustal thickness, and magmatic composition along strike [Hildreth and Moorbath, 1988, DeCelles et al., 2014, Vera et al., 2014]. These subsections include the central volcanic zone (CVZ), northern volcanic zone (NVZ) and southern volcanic zones (SVZ) [Bryant et al., 2006, Blum-Oeste and Wörner, 2016, Rawson et al., 2016]. This arc is the chosen focus of this study as it is well documented in the literature [Bryant et al., 2006, Tilling, 2009, Blum-Oeste and Wörner, 2016, Rawson et al., 2016, Martínez et al., 2018, Burns et al., 2020, Sainlot et al., 2020, Contreras-Reyes et al., 2021, Carrapa et al., 2022, Mallea-Lillo et al., 2022] and displays a wide variation in magmatic compositions and tectonics [Hildreth and Moorbath, 1988, DeCelles et al., 2014, Vera et al., 2014]. The model within this study is calibrated with data specifically from the Southern volcanic zone, as it contains several volcanic centres which contain compositionally diverse magmas that are spatially well resolved [Rawson et al., 2016, Mallea-Lillo et al., 2022]. These magmas are predominantly composed of basalt to andesites with 47-58 % SiO_2 [McMillan et al., 1989, Vera et al., 2014, Rawson et al., 2016, Mallea-Lillo et al., 2022].

1.1.2 Geodynamic Modeling

Many geodynamic models have been developed to simulate the evolution of magmatic systems [Dufek and Bachmann, 2010, Gutiérrez and Parada, 2010, Degruyter and Huber, 2014, Jackson et al., 2018, Keller and Suckale, 2019], but they often simplify or overlook key aspects of geochemical processes. Some models do not account for internal convection or phase segregation [Degruyter and Huber, 2014] and therefore cannot accurately simulate compositional evolution. While some models do incorporate multi-component thermochemical evolution [Dufek and Bachmann, 2010, Gutiérrez and Parada, 2010, Jackson et al., 2018], they typically resolve a simplified geochemical composition, limiting the level of complexity they can capture.

The model used in this research builds on the framework established by Keller and Suckale [2019]. It is a two-dimensional (2D), three-phase finite difference model implemented in MATLAB, which includes solid crystals, liquid melt, and volatile bubbles. Unlike earlier models, this approach simulates fluid mechanics and thermochemical evolution while tracking geochemical behaviour. It tracks geochemical evolution using four pseudo-components representing key mineral and major oxide systems, derived from compositions in the GEOROC database [Watt et al., 2013]. The model can simulate multiple volatile components; however, this study is limited to a single volatile component water (H_2O). In addition to the major oxides and water, the model tracks four unspecified trace elements that range from incompatible to compatible. These are not tied to specific real-world elements but are designed to capture generalised geochemical partitioning during magmatic processes such as fractionation and mixing. Finally, the model includes two generalised stable isotope ratios, which serve as proxies for mixing dynamics.

1.2 Aim and Objectives

The central aim of this study is to understand the dynamic controls on processes such as magma mixing and fractional crystallisation and how these processes contribute to the generation or destruction of geochemical heterogeneity within shallow magma bodies. The main objectives of this study are to:

(1) Model a single magma composition closed system body, which does not experience any external inputs into the system, other than cooling imposed from the wall rock contact. Then systematically vary parameters, including volatile content, chamber size and wall rock cooling rate, to analyse their impact on the dynamics and geochemistry.

(2) Simulate an open-system magma chamber experiencing recharge by a more primitive magma underplating the inital resident mamga. Systematically vary temperature, volatile content, and recharge volume to assess how geochemical signatures evolve during mixing and post-recharge convection, and whether these interactions generate or obscure geochemical signals.

(3) Determine if geochemical data within the open systems permits backtracking to the initial input compositions for magma end member identification.

(4) Explore the feasibility of using real-world rock geochemical data to identify magma chamber processes and provide recommendations for the spatial requirements of whole rock sampling.

Chapter 2

Literature Review

2.1 Continental Arcs and their importance

Continental arcs, also known as Cordilleran or Andean-type arcs [Ducea et al., 2015], form at the interface between two tectonic plates, where the oceanic lithosphere is subducted beneath the continental margin [McKenzie and Parker, 1967, White et al., 1970, James, 1971] (See Figure 2.1). Arc magmas form via the devolatisation of the subducting slab and sediments, which lowers the melting point of the overlying mantle wedge, facilitating partial melting and generating primitive melts [Coats, 1962, Green and Ringwood, 1968, Dickinson, 1970, Annen et al., 2006, Spandler and Pirard, 2013, Ducea et al., 2015]. These primitive melts have undergone minimal differentiation and retain a composition similar to their source material. They are typically basaltic in composition with high magnesium concentrations and low silica contents [Green and Ringwood, 1968, Dickinson, 1970, Annen et al., 2006, Spandler and Pirard, 2013].

As these melts ascend through the overlying continental crust (See Figure 2.1), they undergo significant evolution, usually becoming more felsic in composition [Hildreth and Moorbath, 1988, Annen et al., 2006]. This evolution involves processes such as fractional crystallisation, where minerals crystallise and settle out from the melt, thereby changing the composition of the remaining liquid [Bowen, 1928]. Magma mixing occurs between different magma reservoirs as they ascend through the continental crust [Eichelberger, 1975, Sparks and Marshall, 1986]. Additionally, crustal assimilation can take place, where the melts incorporate elements of the surrounding country rock, further altering their composition [DePaolo, 1981, Annen et al., 2006, Spandler and Pirard, 2013, Ducea et al., 2015, Turner and Langmuir, 2015a]. These magmas may solidify within the crust to form intrusive rocks or continue their ascent to the Earth's surface where they erupt as lavas [Annen et al., 2006].

Continental arcs are critical for understanding Earth's evolution and crustal formation. They are sites of significant crustal recycling and the addition of new material through magma production and processing [Tatsumi and Kogiso, 2003, Hawkesworth et al., 2010, 2020, Cornet et al., 2022]. Additionally, these systems are centres of extensive volcanic activity, posing significant threats to human life.

As the global population increases, more people are living in proximity to active volcanoes.

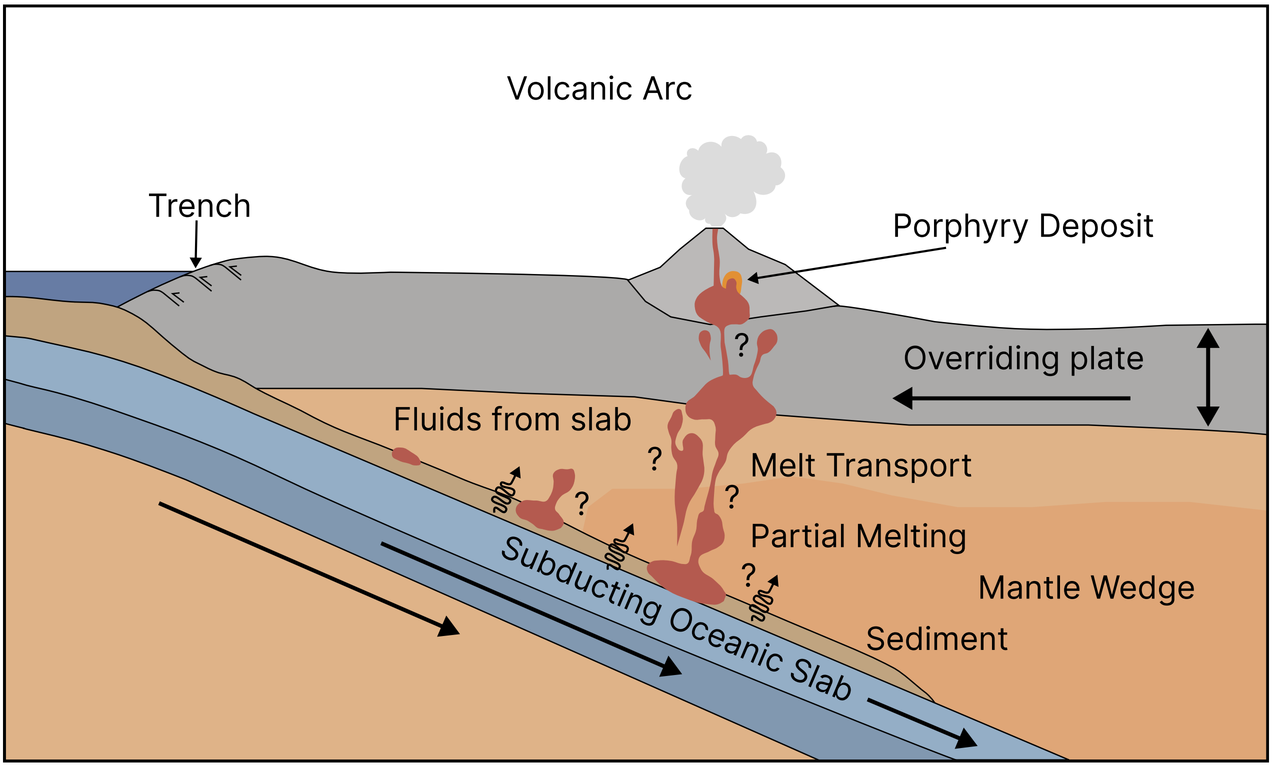

Figure 2.1: Schematic diagram illustrating the sources of geochemical diversity in subduction zone settings. Including the subducting slab, mantle wedge and overriding plate. Figure adapted from [Rawson et al., 2016]

For example, the northwest United States, Colombia, and Chile are home to several major continental arcs within densely populated areas [Freire et al., 2019]. By 2015, 14.3 % of the world's population lived within 100 km of Holocene volcanoes [Freire et al., 2019]. Over 20 million people in the Andes lived within 100 km of an active volcano as of 2004 [Stern, 2004]. This increasing number highlights the need for improved study and monitoring of volcanoes, especially in regions where they pose a serious risk to large populations. Volcanic events like pyroclastic density currents and lahars can affect wide areas and have devastating impacts. The 1985 eruption of Nevado del Ruiz in Colombia triggered a lahar that travelled 85 km and resulted in 23,000 deaths [Stern, 2004]. Further study of volcanoes and their associated crustal magmatic systems is essential for improving hazard prediction and management strategies.

Furthermore, continental arcs are economically significant because they host large porphyry ore deposits [Sillitoe, 1972, Singer et al., 2008, Sillitoe, 2010]. These deposits form from metal-rich fluids released during the cooling of shallow crustal magma bodies, contributing substantially to global reserves of copper, molybdenum, and gold [Chelle-Michou and Rottier, 2021]. Porphyry deposits alone account for 50–60 % of the world's copper supply and 90-95 % of its molybdenum supply [Lees, 2007, Singer et al., 2008, Sillitoe, 2010]. The complex physical and chemical processes involved in porphyry ore formation remain poorly understood; therefore, further research is needed. The formation and significance of continental arcs set the stage for understanding the broader geological context of these systems. The intricate processes within arcs dictate the diversity of magmatic and volcanic products we observe at the surface [Rawson et al., 2016]. To better understand the formation of ore deposits and the triggers of volcanic hazards in arc settings, it is important to develop a deeper understanding of the geochemical processes operating within these systems.

2.1.1 Geochemical Processes in Continental Arcs

Continental arcs display diverse ranges of geochemical signatures at the surface, reflecting the complex interactions within the crustal magmatic systems [Stern, 2004, Ducea et al., 2015, Rawson et al., 2016]. This geochemical diversity is present across both temporal and spatial scales [Stern, 2004, Jacques et al., 2014, Turner and Langmuir, 2015a,b, Rawson et al., 2016]. These geochemical variations can be observed globally between different continental arcs, regionally across a single arc and locally within subsections of an arc [Stern, 2004, Jacques et al., 2014, Turner and Langmuir, 2015a,b, Rawson et al., 2016]. The geochemical variations include differences in rock types, from basalts to rhyolites, as well as in major oxides and trace element compositions, with silica content ranging from 45-75 wt% [Rawson et al., 2016]. Variations are also seen in volatile contents and isotope values [Stern, 2004].

The Andean orogenic system is a prominent example where this geochemical diversity has been extensively studied and debated, particularly due to its economic copper deposits [McMillan et al., 1989, Stern, 2004, Samaniego et al., 2005, Bryant et al., 2006, Vera et al., 2014, Bucchi et al., 2015, Blum-Oeste and Wörner, 2016, Morgado et al., 2017, Martínez et al., 2018, Burns et al., 2020, Sainlot et al., 2020, Contreras-Reyes et al., 2021, Mallea-Lillo et al., 2022]. In the Andean system, where the Nazca plate subducts beneath the South American plate, significant variations in subduction style, such as differences in subduction speed, angle, and crustal thickness, are observed along its length [Bryant et al., 2006, Blum-Oeste and Wörner, 2016, Rawson et al., 2016].

The Andes exhibit diverse geochemical signatures; for instance, within the Southern Volcanic Zone (SVZ), the rocks are predominantly basalts to basaltic andesites [Stern, 2004, Bucchi et al., 2015, Mallea-Lillo et al., 2022]. In contrast, within the Northern Volcanic Zone (NVZ), andesites to dacites are more common [Stern, 2004, Bryant et al., 2006, Samaniego et al., 2005]. Additionally, the Central Volcanic Zone (CVZ) has higher ^{87}Sr/^{86}Sr and δ^{18}O values compared to the Southern Volcanic Zone (SVZ) [James, 1982, Sainlot et al., 2020].

Ongoing debates in the literature focus on the relative contributions of different reservoirs, including the subducting slab, mantle wedge, and crust, as well as processes such as fractional crystallisation, assimilation, and magma mixing, to the observed geochemical signatures in these arc environments [Hildreth and Moorbath, 1988, Plank and Langmuir, 1988, Annen et al., 2006, Miller et al., 2007, Ruscitto et al., 2012, Turner and Langmuir, 2015a,b, Rawson et al., 2016, Cashman et al., 2017, Ardila et al., 2019, Huber et al., 2019, Burns et al., 2020]. One hypothesis suggests that the geochemical diversity of arc magmas is primarily controlled by variations within the mantle source, including changes in temperature, composition, and volatile content, as well as properties of the subducting slab such as dip angle, age, obliquity to the trench, and subduction velocity [Plank and Langmuir, 1988, Ruscitto et al., 2012, Turner and Langmuir, 2015a,b]. A second hypothesis posits that the geochemical diversity arises during the migration of melts from the subduction zone to the surface as they interact with the continental crust. During ascent, magmas can stall within the lower continental crust in zones referred to as Hot Zones or Melting, Assimilation, Storage, and Homogenisation (MASH) zones [Hildreth and Moorbath, 1988, Huber et al., 2019]. Over millions of years, processes such as fractional crystallisation, crustal assimilation, and magma mixing can significantly alter the geochemical signatures of the magmas [Annen et al., 2006, Miller et al., 2007, Cashman et al., 2017, Ardila et al., 2019, Burns et al., 2020]. The complexity of arc systems, both at the arc scale and within individual magma reservoirs, poses significant challenges in interpreting geochemical data [Dufek and Bachmann, 2010, Karlstrom et al., 2010, Rawson et al., 2016]. Understanding the relative importance of different processes and reservoirs is crucial for deciphering the origins of geochemical diversity in continental arcs. Shallow crustal magma reservoirs are crucial because of their proximity to the surface and serve as the final storage stage before volcanic rocks erupt.

2.1.2 Shallow Crustal Magma Reservoirs in Arc Settings

Throughout the past century, conceptual models of shallow arc magmatism have evolved significantly. Initial conceptual models such as Daly [1911] envisaged a single melt-rich magma chamber supplied from below by a single conduit (See Figure 2.2 A). This "big tank" conceptual model portrayed a long-lived melt-rich reservoir chamber that gradually cooled over time and helped shape our understanding of volcanic processes and the formation of igneous rocks [Glazner, 2007, Annen et al., 2015].

Geophysical, geobarometry and zircon recycling studies began to challenge this conceptual model, leading to a shift in the literature [Coleman et al., 2004, Matzel et al., 2006, Lees, 2007, Schoene et al., 2012, Pritchard et al., 2018]. A study within the Andean subduction zone showed numerous complex magma ascent pathways, contradicting the idea of a single vertical conduit [Schurr et al., 2003]. A new conceptual model of a mush-rich system, known as the trans-crustal magmatic system (See Figure 2.2 B), has begun to emerge [Cashman et al., 2017, Edmonds et al., 2019, Sparks et al., 2019, Marxer et al., 2022]. This model proposes that melt-rich systems in the shallow crust may be short-lived, and that the magmatic plumbing system is made up of multiple reservoirs, envisioned as crystal-rich mush rather than melt-dominated magma. It suggests that most differentiation occurs deeper, within the mid to lower crust [Sparks et al., 2019], and highlights the dynamic nature of these systems across phases: molten melt, mush, volatile gas, and country rock [Sparks et al., 2019]. Previous studies looking at the shallow portions of trans-crustal plumbing systems have focused on the importance of recharge, the thermal state of the crust and the volatile content of the system in relation to the formation and lifespan of melt-rich magma bodies [Annen and Sparks, 2002, Schöpa and Annen, 2013, Karakas et al., 2017, Huber et al., 2019]. Additionally, the volatile content has been examined in relation to pressure within the system to assess the storage conditions of magma and the style of volcanic eruptions that will result from them [Popa et al., 2021].

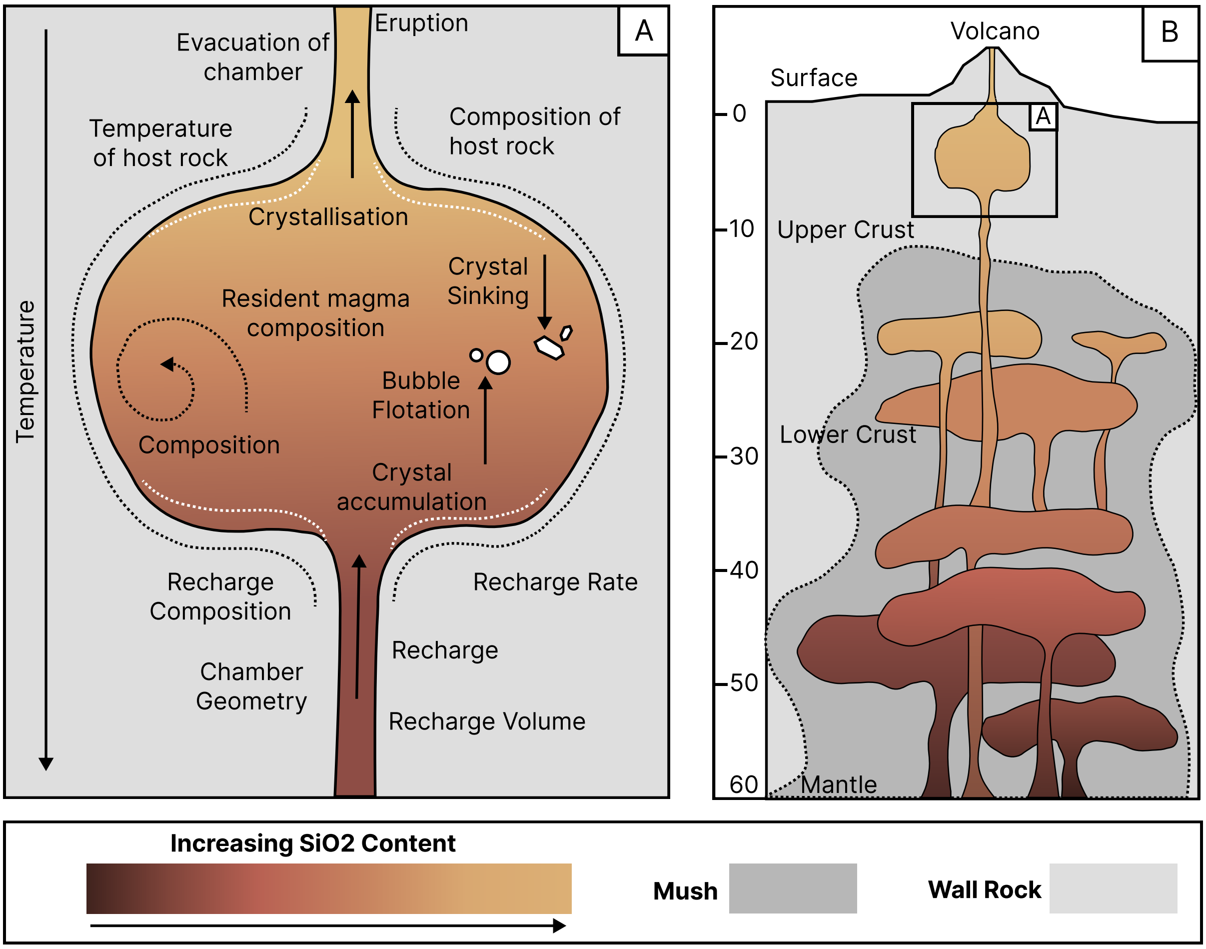

Figure 2.2: Conceptual model of the volcanic plumbing system and shallow crustal magma chamber. (A) This panel shows a shallow, melt-rich magma body and outlines the processes influencing geochemical signatures, such as fractionation and mixing. The arrow on the left indicates the thermal gradient, increasing temperature at greater depths. (B) Depicts the shallow magma reservoirs in the context of the larger trans-crustal magmatic system. The colour scale reflects increasing silica content, from low silica near the mantle to higher silica values in the upper crust, showing the evolution of magma composition with depth. Adapted from [Hildreth, 2004, Cashman et al., 2017, Chelle-Michou and Rottier, 2021].

This study focuses on the internal dynamics of these shallow portions and aims to understand how these dynamics influence the geochemical signatures fed into them from the deeper plumbing system. To achieve this goal, the project uses a state-of-the-art numerical model to simulate 2D shallow crustal magma bodies. By integrating fluid mechanics, thermochemical evolution, and geochemical processes, the model provides insight into how magma mixing, fractional crystallisation, and other dynamic processes shape the geochemical compositions found in shallow arc settings.

2.1.3 Computational Geodynamic modelling

The field of geodynamic modelling has grown significantly over recent decades with geodynamic numerical models being used to explore a diverse range of geological settings and processes from mid-ocean ridge, plume and subduction dynamics, to surface plate deformation and the formation of planetesimals [Tackley et al., 1993, Billen, 2008, Katz, 2010, van Hunen and Allen, 2011, Bouilhol et al., 2015, Dannberg and Gassmöller, 2018, Grima et al., 2020, Stein et al., 2020, Langemeyer et al., 2021, Bollino et al., 2022, Gerya, 2022, Hu et al., 2022, Grima and Becker, 2024]. One subgroup within geodynamic modelling is the field of magma dynamics and multiphase flow models. Models offer great insights into inaccessible processes across both temporal and spatial scales [Gerya, 2022]. Additionally, they serve as great tools for testing scenarios and hypotheses.

Some of the earliest work within multiphase modelling consisted of analytical approaches aimed at understanding the generation of magma and its transport [McKenzie, 1984]. Subsequent work in the 1970s and 1980s investigated two-phase flow between melt and solid residuals [Sleep, 1974, McKenzie, 1984, Fowler, 1985, Scott and Stevenson, 1986]. Much of this work aimed to test the theory surrounding microstructures and melt segregation from a porous matrix [Sleep, 1974]. Other analytical models were constructed to understand the transport of magma [Fowler, 1985, Scott and Stevenson, 1986]. These early studies advanced our understanding of fluid dynamics and established methods of implementing governing equations. The primary governing equations of these models consist of the conservation of mass, momentum, and energy [Ismail-Zadeh and Tackley, 2010]. Most of these two-phase flow models were porous flow models applied to low melt fractions and focused on processes such as mantle convection and magma dynamics. One limitation of these models is that they do not account for high melt fraction systems within suspension flow.

As computational resources expanded and numerical techniques evolved, these analytical models transitioned from conceptual frameworks to fully established computer simulations. These models have been implemented using various discretisation techniques of the governing equations. Primary methods include finite difference, finite volume, and finite element [Torrance and Turcotte, 1971, Stemmer et al., 2006, Alisic et al., 2016]. Other discretisation approaches include finite difference staggered grids [Gerya, 2022] and control volume finite element methods [Geiger et al., 2004, Al Kubaisy et al., 2023]. Each numerical method offers distinct advantages depending on the geophysical problem being modelled. For instance, control volume finite element methods are useful for simulating complex geometries and variable material properties, as they enable adaptive mesh refinement for higher resolution in areas of interest [Geiger et al., 2004, Al Kubaisy et al., 2023]. In contrast, finite difference staggered grid methods, such as mantle convection models, are preferred for large-scale systems due to their computational efficiency and simplicity [Gerya, 2022].

2.1.4 The Challenge of Scale Separation

One limitation of geodynamic models is the scale on which they are numerically resolved. The physics of magmatic systems spans from millimetre-scale phase interfaces to kilometre-wide magmatic systems [Keller and Suckale, 2019]. Current models cannot resolve entire systems while also capturing the wide range of spatial scales present within these systems.

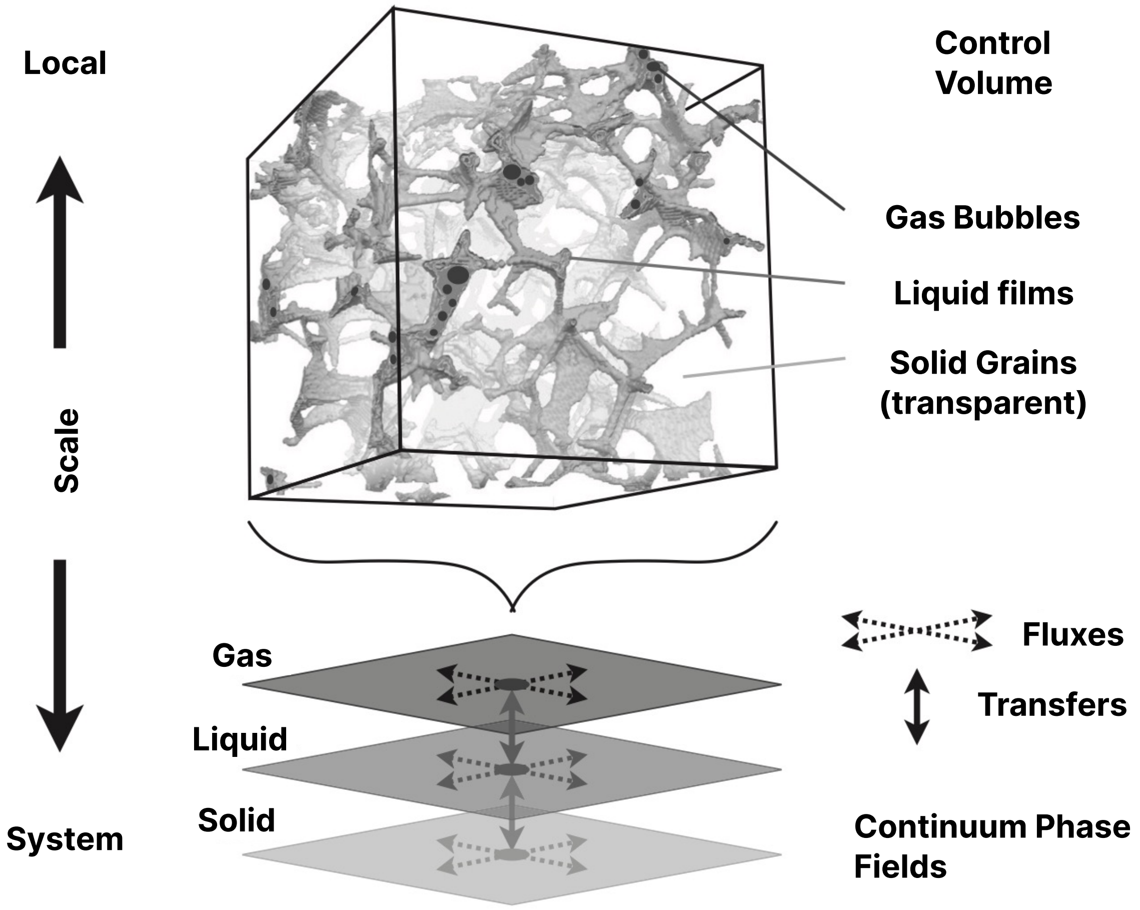

Figure 2.3: Schematic diagram illustrating a local-scale control volume, outlining the three phases present (solid, liquid, and gas), with corresponding system-scale phase fields shown below. Solid arrows represent transfers between phases, while dashed arrows indicate fluxes. Figure from [Keller and Suckale, 2019]

Numerical models presented in the literature are typically categorised based on the specific scales and assumptions they address. One group studies magma dynamics at the scale of phase interfaces [Parmigiani et al., 2011, Qin and Suckale, 2017]. Within this approach, the models investigate the complex interactions between two or three phases (gas bubbles, solid grains, and liquid films) on scales from millimetres to meters (See Figure 2.3). These models, known as direct numerical simulations (DNS), have been used to investigate flow dynamics and the effects of reactant transport [Parmigiani et al., 2011, Qin and Suckale, 2017].

An alternative approach and one that is utilised within this research is called the continuum mixture model. Continuum mixture models resolved magmatic dynamics at much larger system scales, ranging from tens of meters to kilometres [Oliveira et al., 2018, Keller and Suckale, 2019]. These models are based on Mixture Theory [Bowen, 1976], which assumes that the large-scale macroscopic behaviour results from the smaller-scale microscopic phase interactions. These models use a control volume to capture the local scale phase interactions between solids, liquids and gases and average these interactions across the volume. This control volume then represents a point within a set of continuum fields that describe the behaviour of the large-scale system. The three phases (solid, liquid, and gas) are individually resolved in their respective continuum fields. The transfer of mass, momentum and energy between the phases is crucial to the multiphase flow problem (See Figure 2.3).

The detailed microscopic interactions between phases are therefore simplified and represented by the fraction of volume each phase occupies within the control volume. As a result, specific details of phase interactions are not individually tracked but are instead averaged out, allowing the model to focus on the larger-scale behaviour of the system [Keller and Suckale, 2019]. System scale models are primarily used to understand processes occurring within magmatic systems, such as magma transport and magma chamber dynamics.

In addition to spatial scales, these models operate on different temporal scales depending on the processes being simulated. For instance, DNS models may capture relatively short-term interactions, whereas continuum mixture models are better suited to simulate long-term processes such as magma transport that span from hours to years [Parmigiani et al., 2011, Qin and Suckale, 2017, Oliveira et al., 2018, Keller and Suckale, 2019].

A wide range of phase proportions is exhibited throughout natural igneous systems from source to surface. These range from low melt fractions during partial melting within the mantle wedge, to magma mushes and high melt fractions within shallow crustal lenses where suspension flow occurs [Caricchi and Blundy, 2015, Cashman et al., 2017]. As mentioned previously, most early two-phase flow models were limited to porous flow within low melt fractions. To fully describe the wide spectrum of rheological conditions throughout continental arc systems, a framework was developed by [Keller and Suckale, 2019] to capture all of these phase proportions. This framework was later developed into a numerical model by [Wong and Keller, 2023].

It is impossible to simulate every possible process seen in nature at once due to the great complexity of natural systems. Therefore, models are often simplified to reduce complexity [Gerya, 2022]. Within magma reservoirs, one simplification is to consider the systems either open or closed.

Closed systems do not experience any inputs or outputs from external sources, while open systems do. Within the context of this study, closed system models refer to a single magma body that does not experience any recharge or assimilation. The open system simulations experience the addition of a second magma composition within the system as recharge.

A final factor models must consider is geometry and dimensionality. Many use simplified shapes and reduce 3D systems to 2D models to decrease computational complexity. Key examples of this are box models of magma chambers, which aim to study eruption frequency and heat loss to the surrounding country rocks [Jellinek and DePaolo, 2003, Karlstrom et al., 2010, Degruyter and Huber, 2014]. These reductions, however, may neglect significant dynamics and interactions that occur within three-dimensional space.

2.1.5 Shallow Magma Reservoir Simulation

Direct field observations of active magma reservoirs cannot be made. Therefore, numerical models provide insights into magma reservoir dynamics and their associated processes, including convection, fractional crystallisation, recharge, and assimilation (See Figure2.2) [Daly, 1911, Bowen, 1928, DePaolo, 1981].

Several numerical models have been constructed to study magma reservoirs. One common approach is the construction of spherically symmetrical box models [Jellinek and DePaolo, 2003, Karlstrom et al., 2010, Degruyter and Huber, 2014]. These box models simplify the geochemical complexity of magma chambers by representing them as one uniform and constant chemical composition. They often contain a singular pressure and temperature value across the model domain [Degruyter and Huber, 2014]. This style of model has been useful in studying time evolution, eruption frequencies and heat loss to the surrounding country rock [Degruyter and Huber, 2014]. One drawback to spherically symmetrical box models is that they do not capture the internal spatial resolution of processes or the geochemical evolution of the system they are simulating.

An alternative approach is utilised by Bohrson et al. [2020], Heinonen et al. [2020], which uses a thermodynamic model. The main aims of these models are to track the evolution of temperature, enthalpy, and the compositions within magma chambers over time [Bohrson et al., 2020, Heinonen et al., 2020]. However, these simulations do not consider the internal physical dynamics such as convection.

In recent years, researchers have increasingly applied multiphase flow models to the study of magma chambers to gain a deeper understanding of the internal flow mechanics and the complex interactions between different phases within these systems. Multiphase flow models can be resolved in one-dimensional column models [Solano et al., 2012, Jackson et al., 2018] and two-dimensional models [Dufek and Bachmann, 2010, Gutiérrez and Parada, 2010, Keller and Suckale, 2019]. These models often contain components of fluid mechanics, thermochemical evolution, and geochemical evolution [Keller and Suckale, 2019]. Therefore, they can model internal magma chamber dynamics such as convection cycles, fractional crystallisation, phase changes and geochemical heterogeneity. Two models with similar approaches to the one discussed in this research are [Dufek and Bachmann, 2010] and [Gutiérrez and Parada, 2010].

Gutiérrez and Parada [2010] constructed a 2D multiphase suspension flow model using the finite element method. Gutiérrez and Parada [2010] aimed to understand the processes that result in zonation and compositional variations within magma chambers. Their primary focus was on closed systems with varying geometries. They could simulate several chamber processes such as convection, crystallisation, crystal dispersion and volatile movement [Gutiérrez and Parada, 2010]. They found that stock-like geometries were the most eruptable and displayed the widest spectrum of eruptive material compositions [Gutiérrez and Parada, 2010]. Similarly, Dufek and Bachmann [2010] adapted a multiphase fluid dynamics model to explore how compositional gaps within a volcanic series occur. They concluded that the gaps are inherent to fractional crystallisation; however, additional processes such as magma mixing and crustal assimilation may overprint the signatures of fractional crystallisation, adding complexity.

Although these models provided useful insights, their source codes were never shared, and they are not described clearly enough to be reproduced. Also, there have been no updates or follow-up studies using these models in over ten years, limiting their relevance for the current work.

The model used in this study builds upon the framework established by Keller and Suckale [2019], integrating the geochemical evolution of major and trace elements along with stable isotope ratios. This enables us to assess how system dynamics evolve and influence geochemistry, allowing us to ultimately trace the original end-member compositions.

2.1.6 Determining the end member composition of mixed magmas

One of the primary objectives of this study is to utilise machine learning to identify end-member compositions of two magmas after they have undergone magma mixing and fractional crystallisation. Distinguishing the end-member compositions of a volcanic system has important implications for the genesis of the system, its evolution, and the overall formation of the continental crust [Burns et al., 2020]. Within active continental arc settings, the compositions of parental arc magmas are often poorly constrained due to the difficulty of directly sampling the original end members. This is further complicated by geological processes such as magma mixing, fractional crystallisation, and assimilation, which may erase or modify the original chemical signatures [Burns et al., 2020].

Recent developments in machine learning have seen an increase in applications of this technique in geoscience [Karpatne et al., 2018, He et al., 2022]. A study by Ueki et al. [2018] demonstrated that it is possible to distinguish between different tectonic settings using characteristic geochemical data identified via machine learning. This ability to classify tectonic environments using machine learning highlights its potential to enhance our understanding of volcanic systems. Machine learning approaches have also been applied to the prediction of end-member compositions.

Several studies have attempted to decipher end-member magma compositions within the Central Volcanic Zone (CVZ) of the Andes [Blum-Oeste and Wörner, 2016, Burns et al., 2020, Rout et al., 2021]. Blum-Oeste and Wörner [2016] identified three end-member compositions for the CVZ complex using polytopic vector analysis (PVA). PVA is a statistical technique that uses factor analysis to predict end members of mixed magma species [Blum-Oeste and Wörner, 2016]. Their method enabled the estimation of two-parent magma end members: a basalt enriched in incompatible trace elements and a medium-K calc-alkaline basaltic andesite [Blum-Oeste and Wörner, 2016]. A third end member was also identified as a high-K calc-alkaline rhyodacite, interpreted as a partial melt from lower to middle crustal lithology [Blum-Oeste and Wörner, 2016]. This highlights the usefulness of machine learning as a technique for deciphering end-member compositions.

In this study, with the original end members known and used as inputs to the model, there is a unique opportunity to backtrack to the compositions of the two mixing magmas. This approach allows us to evaluate how processes within shallow crustal magma bodies, such as fractional crystallisation and magma mixing, affect the accuracy of the machine learning technique in identifying the end-member compositions.

Chapter 3

Methods

3.1 Overview

In a similar approach to Keller and Suckale [2019], Keller [2025], this study applies the numerical model Nakhla to model magma chamber dynamics and chemical mixing. Implemented in the software MATLAB, the code simulates the dynamics of a three-phase multicomponent magma system. The model tracks three distinct phases: liquid melt (m), within which solid crystals (x) and volatile bubbles (f) are suspended. Within the scope of this study, the model is configured to replicate a shallow crustal system within a continental arc setting.

The petrological model is calibrated to volcanic and plutonic rocks from the Southern Volcanic Zone Andes case study area. The Andes is an excellent example of a continental arc that displays a wide range of geochemical signatures. The GEOROC Andean Arc Part 1 database [Watt et al., 2013] was used for this calibration. It was filtered to remove samples that had been altered or had incomplete major element compositions.

In natural systems, magmas contain a diverse range of major elements and volatile components, mainly due to the heterogeneity of the subducted slab, mantle wedge and continental crust. Resolving this level of detail in a numerical model presents significant challenges because of its inherent complexity and computational demands. Nakhla addresses the chemical heterogeneity by using four pseudo-components. The multicomponent melting model, designed to approximate local phase equilibria, is adapted from Keller and Katz [2016], Keller [2025]. These pseudo-components represent the bulk composition and influence the degrees of freedom in which the magma composition can evolve. They can be further resolved into mineral systems, mineral end members, and individual element oxides, specifically SiO_2, TiO_2, Al_2O_3, FeO, MgO, CaO, Na_2O, and K_2O. A full breakdown of the pseudo-components, mineral systems, mineral end members, and oxides is provided in Appendix 7.1. The chemical components can partition between the crystal and melt phases. One limitation of the model is that the pseudo-phase diagram uses linear solution-type phase relations, which allow all components to co-occur with one another—such as olivine and quartz—even though such combinations are not typically stable in natural systems.

Magmatic petrogenesis relies on the interplay of temperature (T), pressure (P), and bulk composition (C), which collectively influence the stability and composition of phases within a magmatic system. Nakhla employs a multicomponent phase diagram approach, adapted from Keller and Katz [2016] and further detailed by Keller [2025]. This approach simplifies the complex thermodynamic behaviour of the system into a multi-dimensional phase loop. The phase loop is used to calculate the proportions and compositions of solid and liquid phases at each point in time, providing an approximation of the local phase equilibria [Keller, 2025]. This simplified phase diagram approach allows the model to effectively track how the composition of the magma changes over time, predicting the crystallisation sequence and the evolution of mineral phases as the system cools and fractionates. In addition to the major oxides, the model also tracks volatile components. In this study, a single volatile component water (H_2O) is considered, which can partition between the bubble and melt phases.

The following sections will detail the model's key components, discuss the numerical implementation, and describe the analytical techniques utilised in this research.

Thermochemical Evolution

This section of the model tracks the evolution of temperature and composition, encompassing major elements and the water volatile [Keller and Suckale, 2019, Keller, 2025]. This section updates phase equilibrium and phase components, following the laws of mass and energy conservation.

The governing equations within this section are as follows:

$$\frac{\partial F^i}{\partial t} + \nabla \cdot (F^i \mathbf{v}^i) = -\nabla \cdot \mathbf{q}^i + \Gamma^i, \tag{3.1}$$

$$\frac{\partial C_j}{\partial t} + \nabla \cdot \left(\sum_i F^i c_j^i \mathbf{v}^i \right) = -\sum_i \nabla \cdot \mathbf{q}_j^i, \tag{3.2}$$

$$\frac{\partial S}{\partial t} + \nabla \cdot \left(\sum_i F^i s^i \mathbf{v}^i \right) = -\nabla \cdot \mathbf{q}_s + \Upsilon_s, \tag{3.3}$$

The first equation (Equation 3.1) solves for phase densities (F^i), where i, = phases (melt m, crystals x, fluid f). Equation 3.2 solve for component density (C_j), where ($j = 1, ..., n$) ,n = the number of pseudo component). The final equation (Equation 3.3) solves for entropy (S). Where:

$\partial / \partial t$ is the partial time derivative, $\nabla \cdot$ is the divergence operator, $\mathbf{v}^i$ is the phase velocity field; $\mathbf{q}^i$ is the diffusive flux of phase i; and Γ^i is the phase change rate. Within Equation 3.2, $\mathbf{q}_j^i$ is the diffusive flux of the various pseudo-components, $\sum_i$ is the sum of the phases and c_j^i is the values for the pseudo-components j of the different phases i. Finally within Equation 3.3, Υ_s is the entropy production or heat dissipation rate and $\mathbf{q}_s$ is the entropy flux.

The energy within the system is formulated in terms of specific phase entropies s^i and can be used to formulate sensible and latent heat content. This approach is not standard in geodynamic models; however, it accounts for sensible and latent heat content, and therefore captures the effects of latent heat during phase transitions like crystallisation. Standard thermodynamic theory is applied to express the system's heat in terms of temperature. The model excludes consideration of heat production from external sources such as radioactive decay.

On the left-hand side of the equations, the first term represents the rate of change of the phases, composition, and entropy densities (F^i, C_j and S). The second term is the advection term, which calculates the balance of advection fluxes carried by the phase velocity fields v^i. On the right-hand side of the equations is the diffusion balance term q_i, the phase change rate Γ^i and the entropy production or heat dissipation rate Υ_s.

Fluid Mechanics

The fluid mechanics model simulates the flow of magma and its internal phases within the system. It tracks convection and flow within the chamber domain and determines the segregation of different phases. The model addresses compressible flow and utilises the compressible Navier-Stokes equations to govern the dynamics. Specifically, it incorporates the conservation of momentum Equation 3.4 and the conservation of mass Equation 3.5. This model is specifically designed for Reynolds numbers below 100; therefore, it only accounts for laminar flow and cannot simulate turbulent flow.

$$\frac{\partial \bar{\rho}\mathbf{v}}{\partial t} = \boldsymbol{\nabla} \cdot \bar{\eta}\underline{\mathbf{D}}(\mathbf{v}) - \boldsymbol{\nabla} P + \Delta\bar{\rho}\mathbf{g} \ , \tag{3.4}$$

$$\frac{\partial \bar{\rho}}{\partial t} = -\boldsymbol{\nabla} \cdot (\overline{\rho \mathbf{v}}) \ , \tag{3.5}$$

The momentum equation (Equation 3.4) describes the change in fluid momentum over time. On the left-hand side, $\partial\bar{\rho}\mathbf{v}/\partial t$ represents the rate of change of momentum, where $\bar{\rho}$ is the mixture density, $\mathbf{v}$ is the mixture velocity vector and $\partial/\partial t$ is the partial time derivative. On the right hand side, the first term, $\nabla \cdot \bar{\eta}\underline{D}(\mathbf{v})$, accounts for the viscous stress contributions, where $\bar{\eta}$ is the effective viscosity and $\underline{D}(\mathbf{v})$ is the deviatoric strain rate tensor and $\nabla\cdot$ denotes the divergence operator. The second term, $-\nabla P$, represents the pressure gradient, which drives the fluid from high to low pressure regions. The final term, $\Delta\bar{\rho}\,\mathbf{g}$, is the buoyancy force, where $\Delta\bar{\rho}$ is the density difference from a reference density, and $\mathbf{g}$ is the gravitational acceleration vector.

The conservation of mass equation (Equation 3.5) governs the fluid's mass balance. On the left-hand side, $\partial\bar{\rho}/\partial t$ represents the rate of change of density over time. On the right-hand side, the term $-\nabla \cdot (\overline{\rho\mathbf{v}})$ describes the divergence of the mass flux, where $\overline{\rho\mathbf{v}}$ is the mass flux vector. The divergence operator $\nabla\cdot$ measures how mass is transported within the domain, ensuring conservation.

Geochemical Evolution

The geochemical evolution section tracks four trace elements and two stable isotope systems. Unlike the major oxides, trace elements and isotopes do not influence melting behaviours or thermochemical evolution. The four trace elements within this study are defined using Equation 3.6. The trace elements undergo partitioning between the melt and solid phases, controlled by their partitioning coefficients K_{tr}. The partition coefficients are calculated as the solid concentration divided by the melt concentration. A K_{tr} value $<<$ 1 designates an incompatible trace element, while a K_{tr} value $>>$ 1 represents a compatible trace element. In this study, four general trace elements were implemented and are categorised as incompatible, slightly incompatible, slightly compatible, and compatible and have corresponding partitioning coefficients of ($K_{tr} = 0.01, 0.10, 3.0, 10.0$). For this study, they are dimensionless relative concentrations normalised to a background concentration and not defined as exact real-world trace elements.

The model used within this work includes two isotope systems (si) as part of its framework; for this study, only one isotope ratio is necessary to act as a passive tracer of mixing. The two stable isotope systems are not defined as exact real-world systems but instead as dimensionless values. They follow the structure of delta notation (δ) commonly used in geochemistry [McKinney et al., 1950, Sharp, 2017]. In delta notation, the isotope ratio is compared to some reference standard and is expressed as a relative difference. From this, we see positive and negative values [McKinney et al., 1950, Sharp, 2017]. The stable isotopes within this study are not calculated using actual isotope ratios. They are instead assigned values of -1 (for isotope one) and +1 for (isotope two) to emulate the behaviours of delta notation. As the second isotope system is the inverse of the first, it exhibits identical patterns as isotope one but in reverse and does not provide additional insights. Therefore, only the results of the first isotope system are discussed in this study.

The isotopes do not partition between any of the phases (melt, crystals, or bubbles) and therefore function solely as passive tracers of mixing between the two magma compositions of the open simulations. They are also utilised within the machine learning analysis. The isotopes are defined using Equation 3.7.

$$\frac{\partial \Theta_{tr}}{\partial t} + \boldsymbol{\nabla} \cdot \bar{\rho}(\theta_{tr}^{m}\, m\mathbf{v}^{m} + \theta_{tr}^{x}\, x\mathbf{v}^{x}) = \boldsymbol{\nabla} \cdot \bar{\rho} m k_c \boldsymbol{\nabla} \bar{\theta}_{tr} \ , \tag{3.6}$$

$$\frac{\partial \Theta_{si}}{\partial t} + \boldsymbol{\nabla} \cdot \bar{\rho}(\bar{\theta}_{si}\, m\mathbf{v}^{m} + \bar{\theta}_{si}\, x\mathbf{v}^{x}) = \boldsymbol{\nabla} \cdot \bar{\rho} m k_c \boldsymbol{\nabla} \bar{\theta}_{si} \ , \tag{3.7}$$

The first geochemical Equation 3.6 tracks the evolution of the trace elements (tr). Where $\Theta_{tr} = \bar{\rho}\bar{\theta}_{tr}$ is the conserved bulk density of a trace elements (tr). Within the equation $\bar{\rho}$ is the mixture density and $\bar{\theta}_{tr}$ is the bulk (phase-averaged) concentration. The term $\partial/\partial t$ denotes the partial derivative with respect to time, representing the rate of change of this bulk concentration. The divergence operator $\nabla\cdot$ appears throughout to describe the net flux of material entering or leaving a volume. θ_{tr}^{m} and θ_{tr}^{x} are the concentrations of the trace element in the melt m and crystal x phases, respectively. These phase concentrations are advected by the corresponding phase velocities $\mathbf{v}^{m}$ melt and $\mathbf{v}^{x}$ crystal, and weighted by the volume fractions m and x. The right-hand side of the equation represents diffusive transport of the trace element within the melt phase m, where k_c is an effective chemical diffusivity and $\boldsymbol{\nabla}\bar{\theta}_{tr}$ is the gradient of the bulk concentration.

Equation (3.7) describes the evolution of stable isotopes (si). This equation is almost identical to the trace element equation (Equation 3.6) however, the stable isotopes do not fractionate between phases. This implies that $\theta_{si}^{m} = \theta_{si}^{x} = \bar{\theta}_{si}$, such that a single, phase-independent bulk concentration appears in both advection terms. As in the trace element case, stable isotopes are transported by melt and crystal advection and diffuse through the melt.

3.2 Numerical Implementation

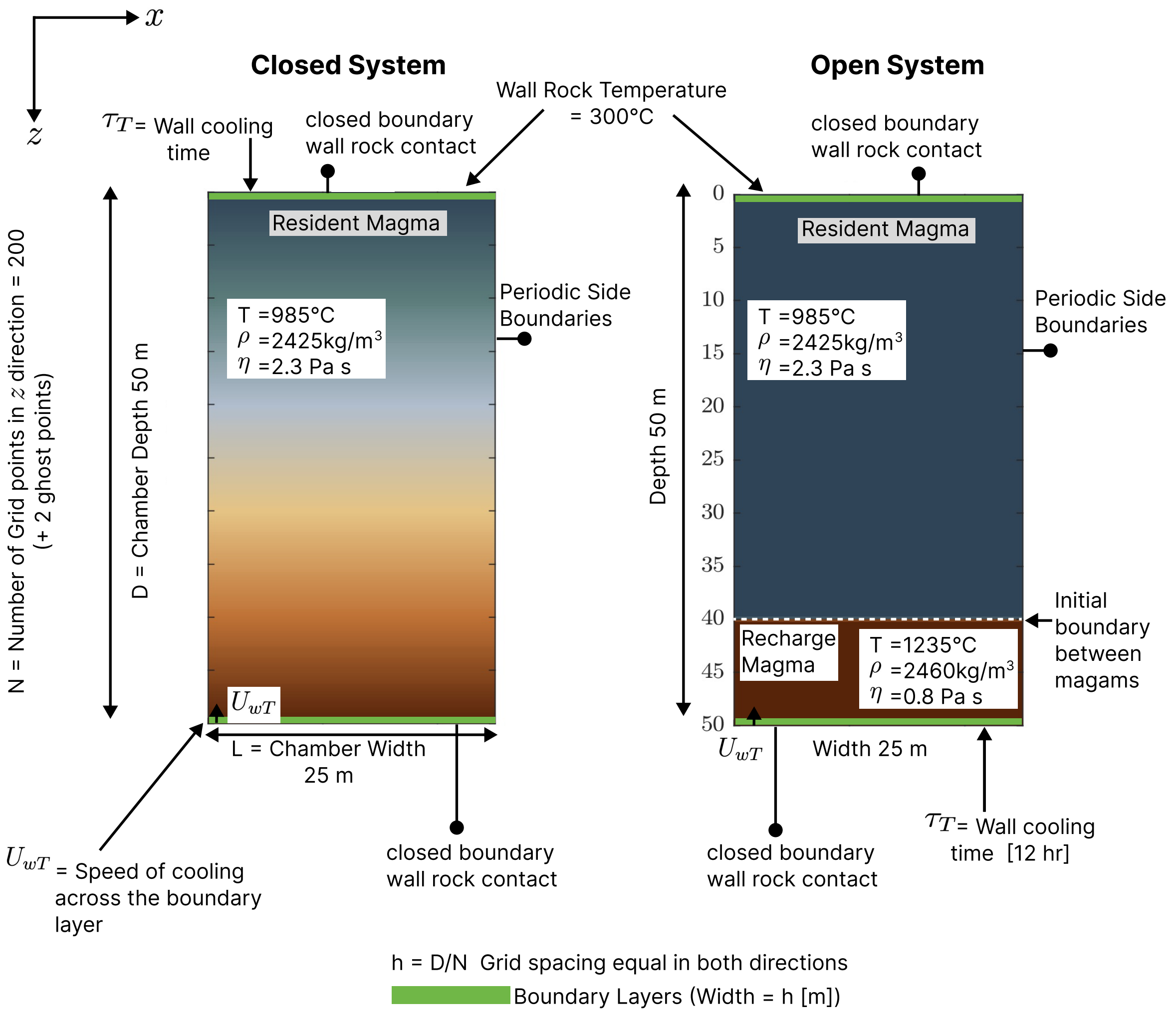

Figure 3.1: Diagram illustrating both a closed system (one magma composition) and an open system (two magma compositions) model setup. The figure outlines the initial temperature [T], density [ρ], and viscosity [η] values of the magmas. It also specifies the domain size and dimensions. The schematic indicates the wall rock contacts at the top and bottom boundaries of the model domain, along with the internal boundary layer where thermal boundary conditions, including wall rock cooling, are applied. Finally, it highlights the periodic side boundaries of the domain.

The governing equations set out above (Equations 3.1 to 3.7) are discretised using the finite difference staggered grid method [Gerya, 2022]. The coupled system of equations is solved with a non-linear iteration loop where thermo-chemical and fluid-mechanical variables are solved, and material coefficients are updated, until the norm of the non-linear residual drops below a prescribed tolerance.

3.3 Boundary Conditions

The model domain is a 2D rectangular Cartesian box representing a crustal magma body, approximating a sill (see Figure 3.1). The model domain spans 25 m horizontally and 50 m vertically, discretised into 100 grid cells in the horizontal direction and 200 grid cells in the vertical direction, resulting in a grid resolution of 0.25 m × 0.25 m. The top and bottom boundaries are closed, simulating wall rock contacts with zero-flux conditions for thermochemical variables and no-slip conditions for velocity and pressure variables. Rather than applying thermal boundary conditions directly at the external boundaries, an internal boundary layer within the domain allows for a more complex simulation of cooling effects. The side boundaries are periodic to avoid artificial forcing and to maintain natural flow dynamics within the model [Schmeling et al., 2008]. Additionally, the model allows for the placement of an internal boundary between two magmas, which can be set at varying depths to simulate different recharge volumes. This setup can simulate composition, density, and viscosity contrasts between the different magmas.

3.3.1 Dimensional Analysis

Dimensional analysis was performed on the governing equations to derive characteristic physical scales to understand the model outputs better. The characteristic velocity ratios can be used to define non-dimensional numbers and understand the controlling parameters within the system. These non-dimensional numbers help determine the relative significance of different physical processes. Several characteristic velocities can be identified within the governing equations, including the speed of advection, the crystal segregation speed, the diffusion velocity and the characteristic speed of cooling of the boundary layer, outlined below.

$$u_a = \frac{\Delta\rho_0 g_0 D_0^2}{\eta_0} \tag{3.8}$$

$$u_{s\chi} = \frac{\Delta\rho_0 g_0 d_0^2}{\eta_0} \tag{3.9}$$

$$u_d = \frac{k_T}{D_0} \tag{3.10}$$

$$u_{wT} = \frac{h_0}{\tau_T} \tag{3.11}$$

Where g_0 is the gravitational acceleration, crystal size d_0, characteristic magma viscosity η_0, thermal diffusivity k_T, boundary layer width h_0, wall rock cooling time τ_T characteristic length of the system D_0. The characteristic density contrast $\Delta\rho_0$ is proportional to factors such as crystallinity, bubble-derived density contrasts, thermal density contrast, and chemical density contrast. The non-dimensional numbers can then determine system behaviours and the relative importance of different physical processes. Within this work, three dimensionless values are defined. The Rayleigh number (Ra) is defined as the relationship between the characteristic advective velocity or convective speed (u_a) and the velocity of diffusion (u_d).

$$\text{Ra} = \frac{u_a}{u_d} = \frac{\Delta\rho_0 g_0 D_0^3}{k_T \eta_0} \tag{3.12}$$

The Rayleigh number (Ra) compares the relative importance of advective transport, driven by density differences and gravitational forces, to diffusive transport, indicating whether convective or diffusive processes dominate the system. High values of Ra suggest that advective transport is the dominant process. In this context, D_0 was chosen as 10% of the depth of the convecting layer. This characteristic length scale D in Stokes' law represents a sphere with a density contrast falling through a liquid. By taking 10% of this sphere's size, we approximate the size of a plume head, which provides an appropriate magnitude for the characteristic advective velocity. Thus, D_0 is set to $D_0 = \frac{D}{10}$ to represent this scale accurately.

The second non-dimensional value defined is Ru, which is the ratio between the settling speed of the crystals ($u_{s\chi}$) and the convective speed of the magma (u_a), which simplifies down to the crystal size versus the model size.

$$\text{Ru} = \frac{u_{s\chi}}{u_a} = \frac{d_0^2}{D_0^2} \tag{3.13}$$

Ru compares the relative importance of the magma buoyancy and crystals settling within the system. High Ru values indicate that crystal settling is the dominant process, while low values suggest convection is dominant.

The final non-dimensional value is defined as Rw which is the ratio between the convective speed of the magma (u_a) and the characteristic speed of cooling over the boundary layer (u_{wT}).

$$\text{Rw} = \frac{u_{wT}}{u_a} = \frac{\eta_0 h_0}{\tau_T \Delta\rho_0 g_0 D_0^2} \tag{3.14}$$

Where h_0 is the depth of the boundary layer and D_0 is 10% of the convecting layer depth.

For high values of Rw, cooling at the boundary will dominate, and when Rw is low, conductive transport will dominate over boundary cooling. Rw compares the rate of boundary cooling to the convective transport of heat.

3.3.2 Machine Learning

The final analytical technique used in this research is a machine learning-based approach using the MATLAB script UNMIX (developed by Dr. Tobias Keller). This tool performed principal component analysis (PCA) and factor analysis to extract end-member compositions from the geochemical data. The primary goal of this analysis was to evaluate whether it is possible to reconstruct the original magma compositions after two magmas have mixed within a system.

First, PCA was used to identify the directions in the dataset with the most variance. This helped reduce the complexity of the data by showing how many components are needed to explain the main patterns in the system, while still keeping the important information.

Once the required dimensions are established, the script proceeds with factor analysis or end-member extraction. This section determines whether pure mixing end-members can explain the data. Internal end members are found by taking the most extreme data points internal to the dataset and finding the maximum volume between the data points. Additional external end members are found by finding the vertical minimum volume that all the data points fit inside with no negative end member compositions. The routine for finding the end-member values is similar to the one used in Blum-Oeste and Wörner [2016]. This machine learning approach provided a quantitative framework for determining whether geochemical data from open systems can be used to backtrack to the initial input compositions for magma end-member identification.

Chapter 4

Results

4.1 Simulation Framework

Twenty-five simulations are conducted in this research, each running for one month of real-world time. The resulting in-model progression times vary between 7.66 hr and 83.50 hr due to the differing complexities of the simulations.

As discussed previously, several processes are thought to influence the dynamics within shallow magma bodies, including fractional crystallisation, assimilation, magma recharge, and convective mixing. In this study, the effects of assimilation are excluded, as the models do not accommodate this process.

Magma	**SiO_2**	**TiO_2**	**Al_2O_3**	**FeO**	**MgO**	**CaO**	**Na_2O**	**K_2O**	**Water**	**Units**
Resident	55.35	1.02	14.73	8.97	4.88	5.99	3.86	1.20	4.00	wt%
Recharge	51.03	1.13	17.98	9.46	5.66	9.13	2.98	0.63	2.00	wt%

Table 4.1: Initial major oxide and H_2O compositions of the Resident and Recharge magmas used as input data for the model scenarios. These compositions were calibrated using the GEOROC Andean Arc Part 1 database [Watt et al., 2013] filtered to exclude altered samples and those with incomplete major oxide or H_2O data.

The simulations are organised into two distinct groups. The first batch consists of ten models focusing on simplified closed system scenarios. These models were set up to simulate a magma body in the shallow crust that has already undergone some fractional crystallisation, and therefore has a more evolved composition. The initial magma composition is classified as an andesite, containing 55.35 wt% SiO_2 and 4.00 wt% H_2O. Table 4.1 outlines the full major oxide composition. This starting composition was derived from the GEOROC Andean Arc Part 1 database [Watt et al., 2013], filtered to exclude altered and incomplete samples. The water content was set at 4.00 wt%, consistent with water contents measured in melt inclusions from mafic arc volcanoes, which typically range between 2–6 wt% H_2O [Moore and Carmichael, 1998, Plank et al., 2013, Zellmer et al., 2016, Ruscitto et al., 2010]. The initial temperature was set to 985°C to represent a magma that has cooled slightly but remains above its solidus [Annen et al., 2006]. The initial crystallinity is 1 vol%, with no initial bubble phase. These simulations investigate the interplay between fractional crystallisation and convective mixing within the system.

The second group includes fifteen simulations incorporating instantaneous recharge of a second magma composition into the system (open systems). These models are designed to explore the added complexity of magma recharge and mixing between two magma compositions. They simulate the same resident magma composition and temperature as the closed system simulations, with the addition of a second, recharging magma beneath it. The recharge magma is hotter, with an initial temperature of 1235°C, and more primitive in composition. It is a basalt with 51.03 wt% SiO_2 (outlined in Table 4.1).

This less evolved composition is selected to simulate magma that has not experienced as much fractional crystallisation and is recharging the system from deeper within the crust. The baseline recharge magma contains 2.00 wt% H_2O to investigate the effects of a recharging magma that may have already undergone degassing as it rises. One of the following parameter tests explores the effects of higher water contents in the recharge magma, which is suggested to occur within natural systems [Moore and Carmichael, 1998, Ruscitto et al., 2010, Plank et al., 2013, Zellmer et al., 2016].

Three parameter tests are conducted across the fifteen open system models, varying the temperature and H_2O content of both magmas and the recharging magma volume. These tests examine how these variations affect internal dynamics such as magma mixing.

Within both groups, a reference run is established to serve as a control, allowing for the effects of parameter variations to be assessed. Each simulation varies a single parameter, enabling straightforward comparisons to the reference simulations and providing clear insights into how these changes influence internal dynamics and geochemistry.

4.2 Closed System Dynamics

The ten closed system simulations consist of a closed reference simulation and nine additional runs that vary across four key parameter tests, each designed to explore how internal dynamics respond to different conditions. The first test investigates varying wall rock cooling rates, ranging from 3 hr (fast) to 48 hr (slow), to simulate different thermal preconditioning states within the crust. The second test varies chamber sizes, with models spanning from 12.5 m × 25.0 m to 37.5 m × 75.0 m. The third test examines the impact of crystal size, comparing one simulation with larger crystals (3×10^{-3} m) and another with smaller crystals (3×10^{-4} m), to observe how crystal size affects system dynamics, such as crystal settling speeds. The final test reduces the H_2O content to 2.00 wt%, half that of the reference simulation. Despite these variations, all simulations display similar internal dynamics, including fractional crystallisation, convective mixing, crystal-driven downwellings, and cumulate layering at the system's base. Most of the parameter tests reflect variations in timescales and rates of dynamic behaviours. A summary of all ten simulations and their parameter variations is provided in Table 4.2.

Model ID	Wall rock cooling [hr]	Crystal size [m]	Chamber size [m]	Water content (H_2O) [wt %]
Closed_Reference	12	1×10^{-3}	25 × 50	4.00
Slow_Wall_rock_cooling	**48**	1×10^{-3}	25 × 50	4.00
Fast_Wall_rock_cooling	**03**	1×10^{-3}	25 × 50	4.00
Larger_Crystals	12	$\mathbf{3 \times 10^{-3}}$	25 × 50	4.00
Smaller_Crystals	12	$\mathbf{3 \times 10^{-4}}$	25 × 50	4.00
Smallest_Chamber_25	12	1×10^{-3}	**12.5 × 25**	4.00
Small_Chamber_40	12	1×10^{-3}	**20 × 40**	4.00
Large_Chamber_60	12	1×10^{-3}	**30 × 60**	4.00
Largest_Chamber_75	12	1×10^{-3}	**37.5 × 75**	4.00
Lower_Water	12	1×10^{-3}	25 × 50	**2.00**

Table 4.2: Closed system model IDs and parameter variation values. The varied parameters in each model are outlined in bold

4.2.1 Closed System Reference Simulation

The model outputs are depicted by parameter fields of dynamic and geochemical values, including temperature, density, viscosity, crystallinity, and major oxide values, all calculated at each point within the model domain, illustrated in Figure 4.1.

Throughout the reference simulation, four dynamic behaviours are observed: crystal drips, whole-system convection, crystal accumulation, and layering at the model's base. These behaviours are illustrated in Figure 4.1, highlighting the interconnected relationships between temperature, crystal volume, H_2O content, and velocity. All four parameter fields show the same dynamics, highlighting their coupled relationships.

At the onset of the simulation, cooler layers form at the top and base boundaries due to the imposed wall rock cooling, which results in crystal nucleation. These cooler layers, approximately 4°C below the ambient system temperature, lead to the formation of crystal downwellings that sink from the top boundary into the chamber. These crystal drips drive downwelling flow and can be seen within the crystallinity field (Figure 4.1 A)

The crystal drips persist throughout the simulation, continuously removing crystals from the top boundary and exposing the hotter melt below it to the wall rock contact. This exposure of hotter melt at the boundary, coupled with the latent heat produced from crystallisation, slows the cooling rate at the top boundary relative to the bottom of the system. The top boundary cools at a rate of 0.4 °C/hr while the bottom boundary cools by 16°C/hr. These persistent downwellings can be observed in model run videos within the Supplemental Material.

At the bottom of the system, crystals form due to contact with the cooler wall rock and accumulate due to the settling of crystals from the top of the system. These layers can be seen within Figuer 4.1 A–C. The base layering reaches 50 vol% crystallinity by 5.15 hr, and as the simulation progresses, it thickens as crystals accumulate. By the end of the simulation, the crystal layer is around 0.5 m thick and ranges from over 90 vol% crystals at the base to around 40 vol% at the top (See Figure 4.1 B).

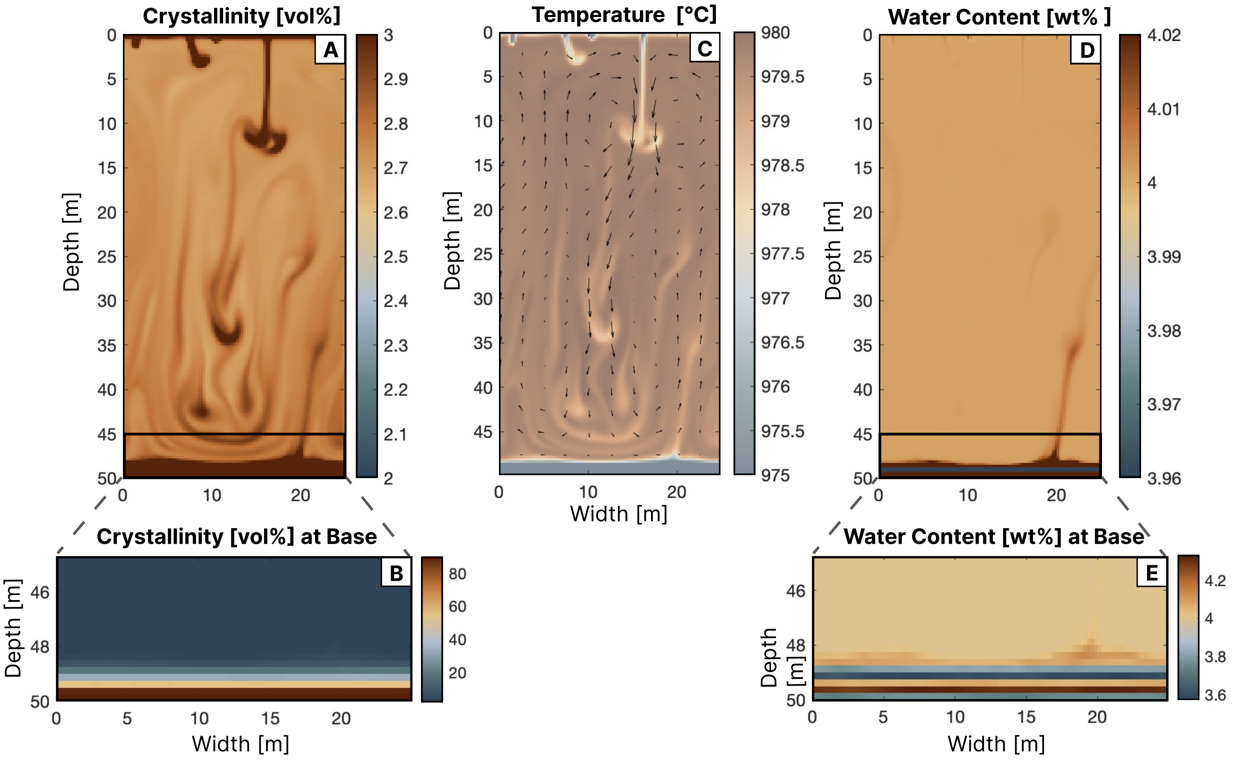

Figure 4.1: Parameter field from the closed system reference model at 28 hr of model time, showing crystallinity temperature and H_2O content. (A) Crystallinity parameter field, where the colour scale represents the system's crystal volume percentage (vol%). The scale range is clipped to display values between 2 vol% and 3 vol%. Darker colours indicate areas of higher crystal vol% highlighting the sinking crystal drips from the top of the systems and crystal accumulation at the base. (B) Crystallinity field without the clipped range of values, focusing on the bottom 5 m of the system. This highlights the high crystal vol% within the cumulate layering. (C) Temperature parameter field, where the colour scale represents temperature values between 975°C and 980°C. A velocity field is overlain as a quiver plot, indicating the direction and magnitude of flow. The flow aligns with the crystal drips, illustrating that these drips control the convective currents. (D) Water content parameter field, where the colour scale shows H_2O content values between 3.96 wt% and 4.02 wt%. This highlights the H_2O rich plumes, and the H_2O varied layer beneath them. (E) The water content field of the bottom 5 m shows the full range of H_2O content values, further highlighting the distribution of H_2O in the base layers and the formation of plumes.

The downwelling from the top of the model domain drives whole-system convection, as evidenced by the quiver plot in Figure 4.1 C. The quiver plot illustrates the direction and strength of the velocity field within the simulation, highlighting the convection currents. The convection persists throughout the whole model simulation with an average convective speed of 46 m/hr. There is no convection within the crystal-dense base layer.

As crystals form at the base of the domain, they exclude H_2O as the water cannot partition into the crystal phase. This exclusion of H_2O causes an increase in the H_2O concentration in the surrounding melt layer and a decrease within the crystal-rich layering. As a result of this crystal accumulation and loss of H_2O, the viscosity at the bottom cumulate layer increases (Figures 4.1 D and E). Once the saturation point is reached, bubbles begin to exsolve and become trapped by the high viscosity. By the end of the simulation, there is approximately 10 vol% trapped bubbles within the cumulate layer. Throughout the simulation, a thin layer of water-rich melt forms above the cumulate at the system's base (Figure 4.1 D). As the simulation progresses, the H_2O content of this layer increases, reaching an average of 4.1 wt% at 11 hr (See Figure 4.1 E).

This increase in H_2O content reduces the melt density and eventually creates a density contrast sufficient to cause small, water-rich plumes to rise into the chamber. These plumes migrate in response to the convection cells driven by the crystal downwellings from the top of the system; their ability to induce substantial convection is limited by the magnitude of the density contrast they create (Figures 4.1 D and E).

This model serves as a robust baseline from which the other models are varied, demonstrating crystal-driven downwellings, base layer accumulation, whole system convection, and water-rich melt plumes rising from the base.

4.2.2 Wall Rock Cooling Variations

The first parameter test of the closed system models investigates how variations in wall rock cooling times affect the internal dynamics of the magma reservoir. These cooling times at the system boundary simulate different thermal conditions of the surrounding country rocks. One simulation features a faster cooling time of 3 hr, representing cooler wall rocks with a smaller thermal aureole. In contrast, a second simulation uses a slower cooling time of 48 hr, simulating magma emplacement into warmer crust. Both simulations are compared to the reference simulation, which has a 12 hr cooling time, to assess how different wall rock cooling rates influence the system's internal behaviour and cooling dynamics. Table 4.2 provides details of these parameter variations.

The wall rock cooling time controls the internal cooling rate of boundary layers (see Figure 4.2). At the end of the fast wall rock cooling simulation, the cumulate layer is less than 400 °C, which is 400 °C cooler than in the slow cooling simulation (see Figure 4.2 A). The simulations reach different model times within the same real-world run times due to variations in internal complexities, such as convective speeds. The varied cooling rates at the system's base lead to different crystallisation rates across the simulations (see Figure 4.2). The faster cooling rate simulation results in more rapid crystallisation at the wall-rock contacts, leading to quicker formation of crystal drips. This process initiates convection more rapidly. The density contrast between the cooling magma at the boundary and the hotter inner system is greater in the faster cooling system, promoting more rapid convective currents. The average convective speeds observed are 99 m/hr for the fast-cooling system and 22 m/hr for the slow-cooling system.

In the slower cooling simulation (48 hr), slower crystallisation results in the cumulate layer reaching 50 vol% crystallinity by 25 hr of model time see Figure 4.2 B. This slower crystallisation allows water-rich melt to form above the cumulate layer, creating a density contrast that promotes plume formation. Consequently, the cumulate layer depletes in water (see Figure 4.2

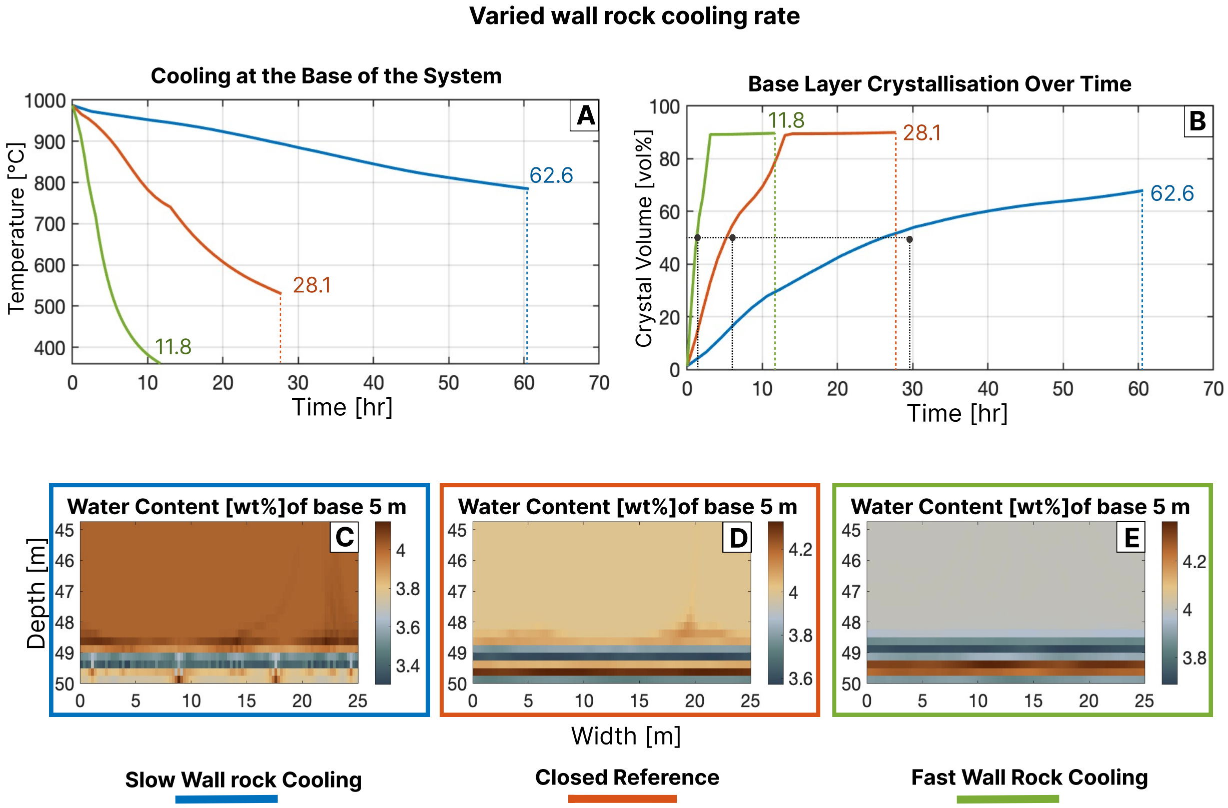

Figure 4.2: Varied wall rock cooling rate simulations compared to the reference simulation. (A) Plot showing the temperature values at the bottom of the system over time for each simulation. This illustrates the varied cooling rates across the parameter test and reference simulations. (B) Plot of crystal volume percentage (vol%) over time for the bottom layers of each model. Variations in wall rock cooling rate significantly alter the crystallisation rate within the system, as indicated by changes in crystal vol%. (C, D, E) Water content parameter fields for the bottom 5 m of each varied wall rock cooling rate simulation and the reference simulation. These panels represent the last time step within each respective model. The colour scale shows H_2O content in weight percentage (wt%). These panels highlight how different cooling rates lead to varied dynamics at the system base, affecting the formation of water-rich plumes or water-depleted zones.

C). By the end of this simulation, the base layer consists of 70 vol % crystals, 7 vol% bubbles, and is depleted in water compared to the reference simulation (see Figure 4.2 C and D). In the faster cooling simulation (3 hr), rapid crystallisation occurs, reaching 50 vol% crystallinity by 1.23 hr of model time, see Figure 4.2 B. This rapid crystallisation traps water and bubbles within the cumulate layer, preventing plume formation. By the end of this simulation, the cumulate layer contains 90 vol% crystals, 11 vol% bubbles, and variable H_2O concentrations, with one layer reaching 4.3 wt% H_2O (see Figure 4.2). In the reference simulation, water-rich plumes form at 14.9 hr of model time (see Figure 4.3). In the slower cooling simulation (48 hr), plumes form earlier, around 9.7 hr, are more frequent, and exhibit rounded morphologies (see Figure 4.3). These plumes contain approximately 4 wt% H_2O and 1–2 wt% crystals, similar to the reference simulation (see Figure 4.3). Conversely, the faster cooling simulation (3 hr) does not show plume formation throughout its run (see Figure 4.3).

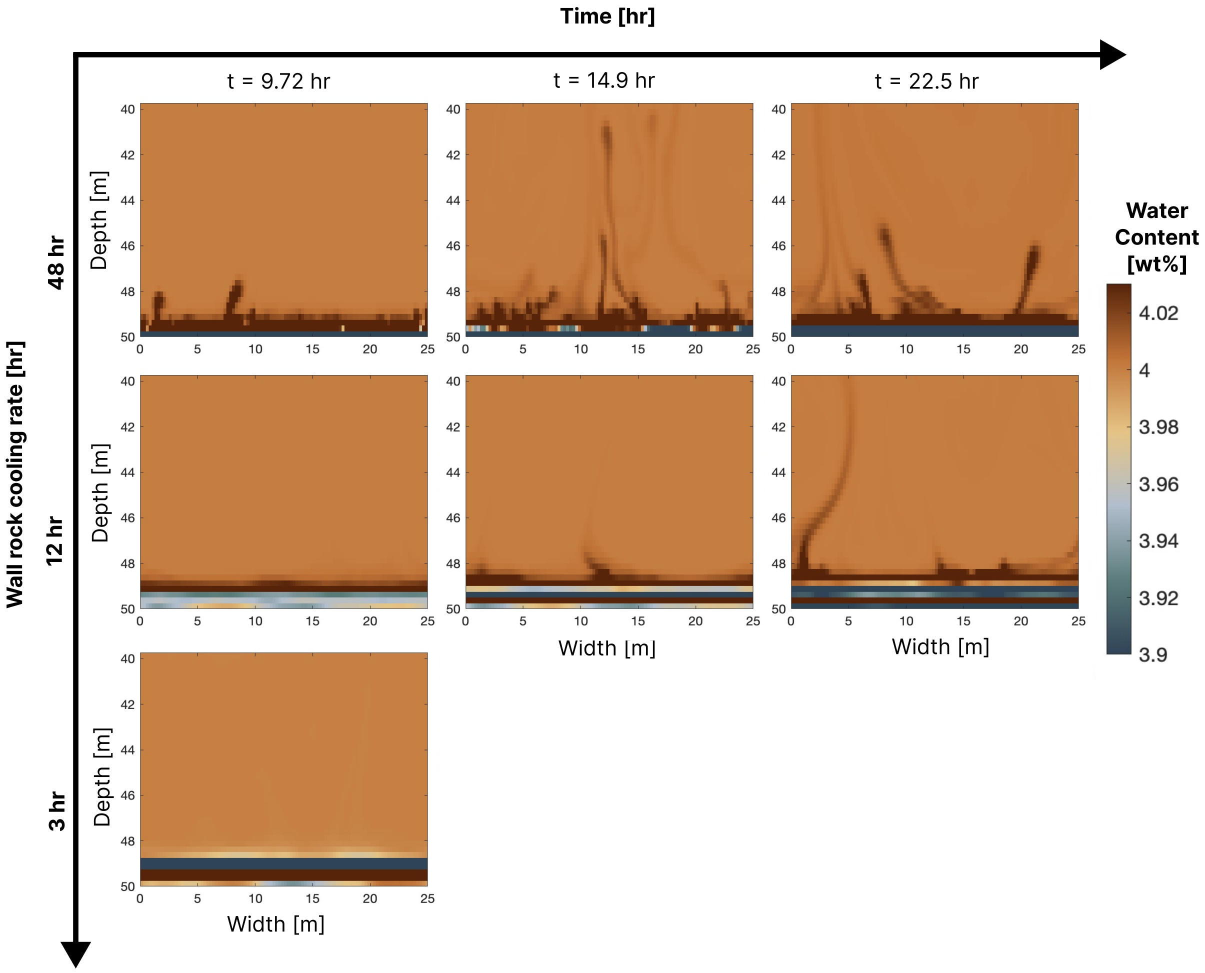

Figure 4.3: Water content (wt%) parameter fields from the two varied wall rock cooling rate models and the reference simulation, showing the bottom 5 m of the systems. The colour scale represents H_2O content values ranging between 3.9 wt% and 4.03 wt%. These values are clipped to this range to highlight the presence or absence of water-rich plumes. The x-axis indicates variations in time, showing the different onset times of plume formation across the simulations. The y-axis outlines the wall rock cooling rate variations, demonstrating that faster cooling rate simulation does not experience plume formation.

4.2.3 Crystal Size Variations

The second parameter test involves varying the crystal size from the Reference model by a factor of 3. The large crystal size simulation has an increased crystal size of 3×10^{-3} m, while the small crystal size simulation has a decreased size of 3×10^{-4} m (See Table 4.2). Both simulations exhibit similar dynamic behaviours to the reference simulation, including convective mixing, crystal downwelling, cumulate formation, and plumes forming at the bottom of the model. However, they display varied timescales for these dynamics.

The crystal settling speeds depend on the crystal size within the system and can be calculated using Stokes law (Equation 3.9). The length scale within Stokes' law can be set to the crystal size (d). This length scale is squared therefore varying the crystal size by a factor of 3 which varies the crystal settling speed by a factor of 9 (See Equation 3.9).

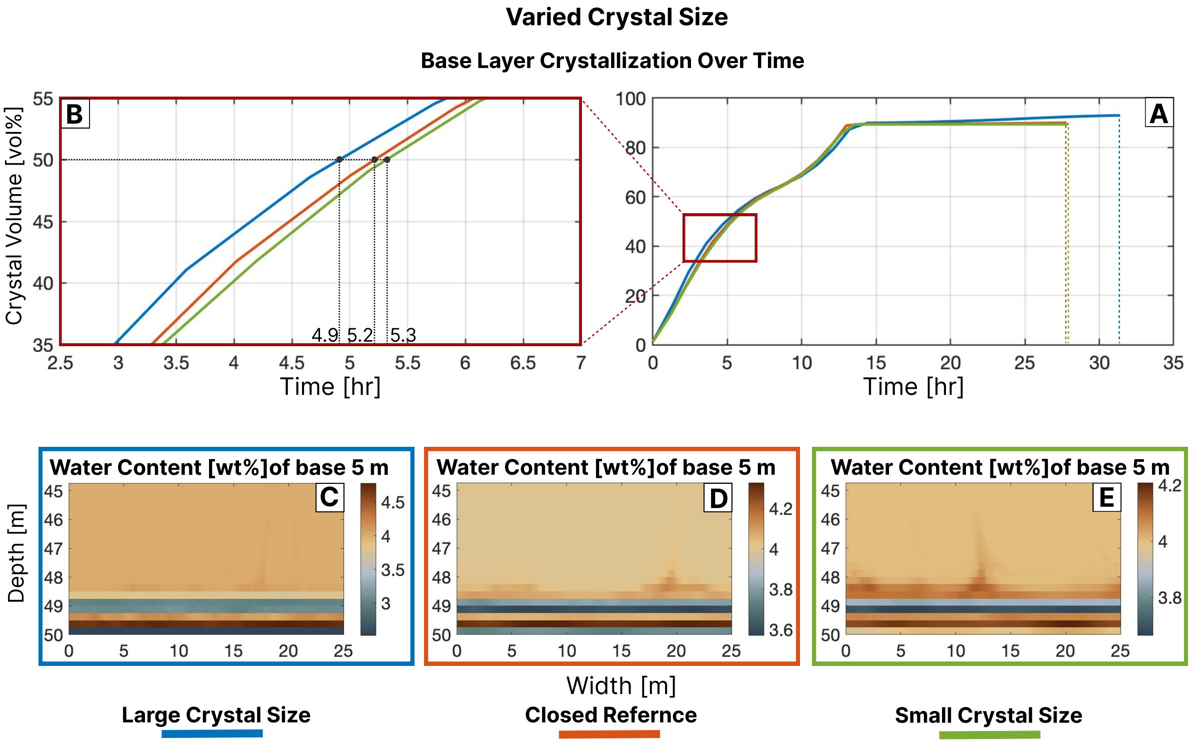

Figure 4.4: Varied crystal size simulations compared to the reference simulation. (A) Plot showing the crystal volume percentage (vol%) values at the bottom of the system over time for each simulation, highlighting the slight variation across the three simulations. (B) The zoomed-in section of plot (A) focuses on crystal volume percentage values between 35 vol% and 55 vol%. This highlights that the simulations reach 50 vol% crystallinity at slightly different times. (C, D, E) Water content parameter fields for the bottom 5 m of each varied crystal size simulation and the reference simulation. These panels represent the last time step within each respective model. The colour scale shows H_2O content in weight percentage (wt%). These panels illustrate how different crystal sizes affect the onset time of plume formation. In the large crystal size simulation, plumes form quickly, and by the end of the simulation, the base layer is depleted of water. In contrast, in the small crystal size simulation, plumes form later, and by the end of the allocated model run time, the base layer still has high H_2O content and plumes remain visible.

The larger crystals have a crystal settling speed of 4.40×10^{-5} m/hr, which is roughly 9 times faster than the settling speed in the reference model (4.93×10^{-6} m/hr). Conversely, the smaller crystals experience a slower crystal settling speed of 4.43×10^{-7} m/hr, roughly 9 times slower than the reference simulation.

The larger crystals' faster settling speed results in a slightly faster accumulation of crystals at the base of the chamber, which reaches 50 vol% crystallinity within 4.9 hr. In the smaller crystal size simulation, the cumulate layer reaches 50 vol% crystals within 5.24 hr, see Figure 4.2 A-B. The Ru values, which are derived from the input parameters (Equation 3.13), increase from 1.58×10^{-7} for smaller crystals to 1.08×10^{-5} for larger crystals. This indicates that while crystal settling speed does increase with crystal size, it remains much smaller than the convective speed in these simulations, even at the higher Ru value. The convective speeds do not vary significantly between these two simulations, relative to the reference simulation.

Both varied crystal size simulations experience the formation of plumes that rise from the base cumulate layer; however, they had varied initiation times and morphologies. Within the large crystal simulation, the H_2O rich plumes form within 1.7 hr. They have narrow stems with rounded heads. The plumes within the small crystal simulation appear much later, at around 24 hr, and are much less frequent. They have wide bases, short stems, and diffuse quickly back into the system after rising around 1-2 m.

By the end of the simulations, the large crystal run shows greater variation of H_2O content within the cumulate layer than the other two runs. This can be seen within the bottom five meters of the three simulations, Figure 4.2 C, D and E. The persistent plume behaviour throughout the large crystal size simulation depletes the bottom of the system of H_2O (Figure 4.2 C). The later plumes that form in the reference simulation and the smaller crystal size simulation are still visible within the H_2O parameter fields at the end of the simulations. They are fed from layers still rich in H_2O, which can be seen within Figure 4.2 D and E.

4.2.4 Chamber Size Variations

The third parameter test involves varying the chamber dimensions. This is achieved by changing the depth of the chamber, with the width being set to half the depth. The chamber size was varied from the reference parameter run, which has a chamber size of [50.0 m × 25.0 m]. The largest chamber variation is set to [75.0 m × 37.5 m], and the smallest chamber is [25.0 m × 12.5 m]. These simulations act as end members for this specific parameter variation group. The parameter variations within this group are outlined in Table 4.2. All four simulations exhibit the same dynamic behaviour as the reference simulation, with varied speeds and timescales.

The convective speed increases as the chamber size increases. This is due to the squared relationship between length scale and convective speed, as described by Stokes' law (Equation 3.8). Like the settling speed calculation, the chamber size can be set as the length scale within Stokes' law, which is squared. Therefore, increasing the domain size will increase the speed of convection. As mentioned previously, the length scale is divided by 10 to approximate the size of a plume head within the system. This allows for the calculation of the advective velocity within the system or convective speed. The largest domain convects four times faster (75 m/hr) than the smallest system (17 m/hr).

The larger system also cools faster at the bottom boundary compared to the smaller chamber. This can be attributed to the speed of cooling across the boundary layer u_{wT} (see Equation 3.11). The large chamber's boundary layer cools by 19°C/hr, while the smaller chamber's base cools by 11°C/hr (Figure 4.5 A). Both systems crystallise at the same rate at the base until reaching 60 vol% crystals (Figure 4.5 B).

Variability in plume dynamics is again observed across this parameter test. The smallest system experiences H_2O accumulation above the layering and plume formation at 5 hr, similar to the reference simulation (Figure 4.5 C and D). Conversely, the large domain simulation does not experience plume formation, instead showing high H_2O and bubble vol% trapped within

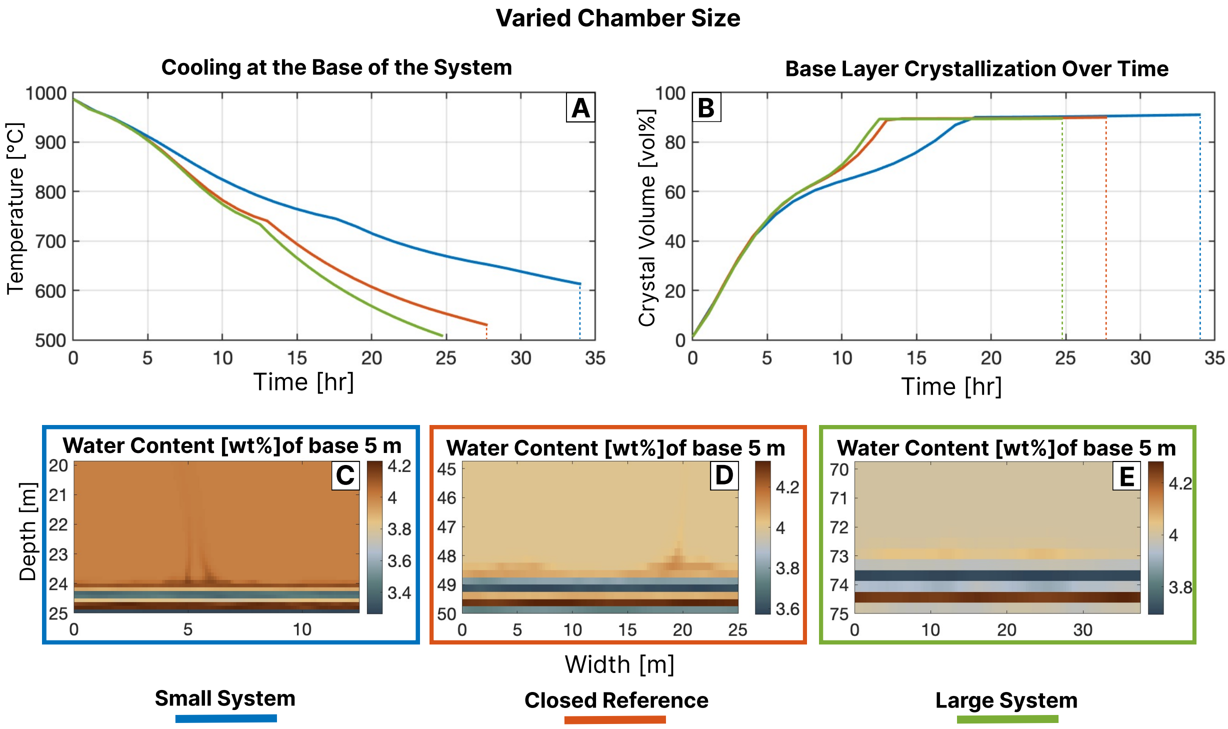

Figure 4.5: Varied chamber size simulations compared to the reference simulation. The figure compares the largest and smallest chamber size simulations among several variations. (A) Plot showing the temperature values at the bottom of the system over time for each simulation. This illustrates the varied cooling rates across the parameter test, with the smaller chamber cooling more slowly than the larger one. (B) Plot of crystal volume percentage (vol%) over time for the bottom layers of each model. Variations in chamber size affect the crystallisation rates, particularly after the base layer reaches 50 vol%. (C, D, E) Water content parameter fields for the bottom 5 m of the varied chamber size simulations and the reference simulation. These panels represent the last time step within each model. The colour scale represents H_2O content in weight percentage (wt%). The panels highlight how different chamber sizes lead to varied dynamics at the system base, affecting the formation of water-rich plumes or water-depleted zones.

the crystal layering (Figure 4.5 E). As the chamber increases in size, plume formation occurs progressively later: at 10 hr in the simulation with chamber dimensions [40.0 m × 20.0 m] and 20 hr in the simulation with dimensions [60.0 m × 30.0 m].

4.2.5 Water Content Variation

The final parameter test within the closed system group involves one simulation with half the H_2O content of the reference simulation (2 wt% water). This reduction in H_2O content leads to an initial increase in crystal vol% from 1 vol% to 3 vol%, and a rise in initial density values by approximately 154 kg/m^3 from the reference model. Moreover, the decrease in H_2O content results in an increase in initial viscosity value, from 2.3 Pa s in the reference model to 3.5 Pa s in the varied H_2O content simulation.

Similar to the reference simulation, the varied H_2O simulation exhibits drip formation at

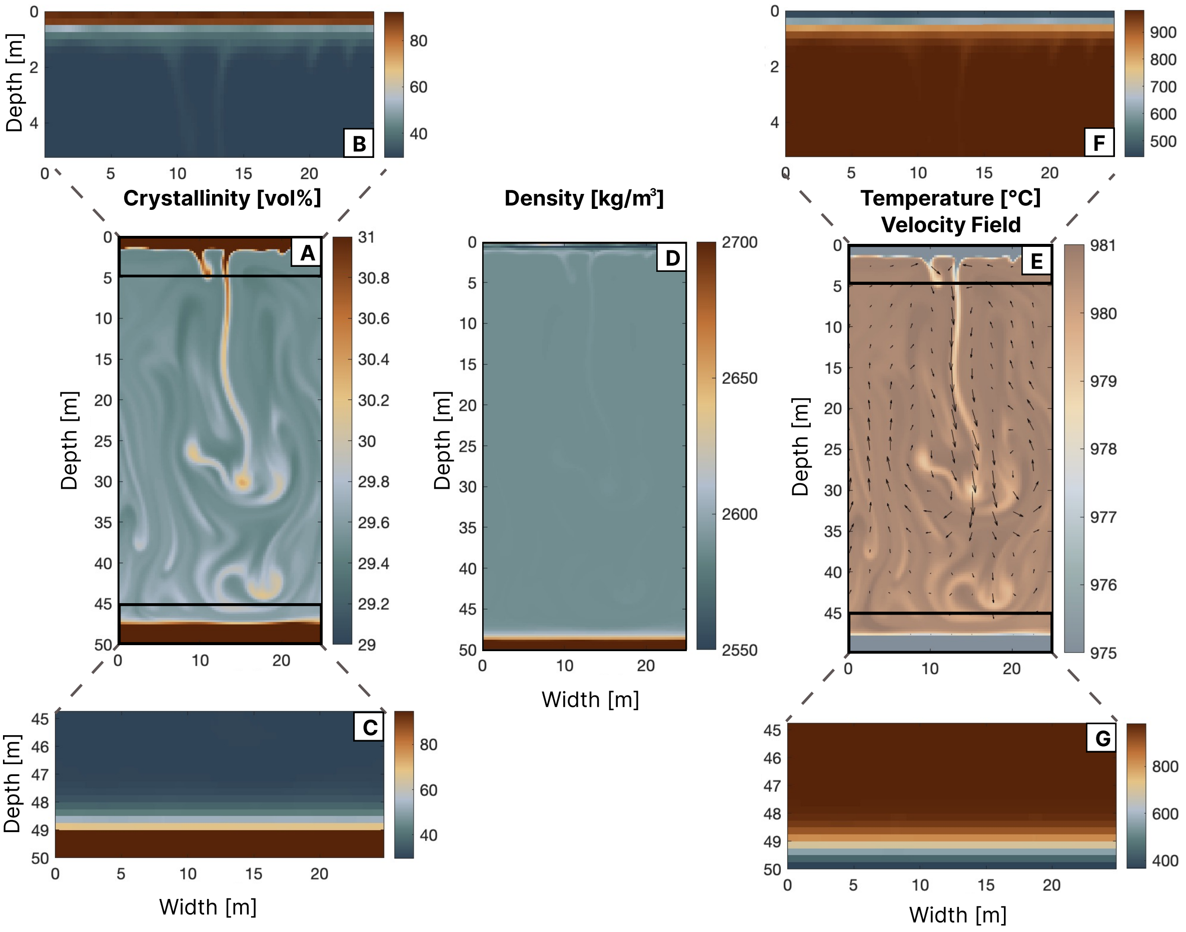

Figure 4.6: Parameter fields from the reduced H_2O simulations (2 wt% water) at 83.5 hr, which is the final frame reached during the one-month run period. The parameter fields show crystallinity, density, and temperature values. (A) Crystallinity parameter field, where the colour scale represents crystal volume percentage, ranging between 29 vol% and 30 vol%. This highlights the crystal drips and layering at the top and bottom of the system. (B) Crystallinity field without the clipped range of values, focusing on the top 5 m of the system. (C) Crystallinity field without the clipped range of values, focusing on the bottom 5 m of the system, highlighting the crystal-dense layering. (D) Density parameter field, where the colour scale represents density values between 2550 kg/m^3 and 2700 kg/m^3 . This highlights the contrasting density between the top and bottom crystal layers. (E) Temperature parameter field, where the colour scale represents temperature values between 975°C and 981°C. A velocity field is overlaid as a quiver plot, indicating the direction and magnitude of flow. The flow aligns with the crystal drips, illustrating that these drips control the convective currents. (F) The temperature field without the clipped range of values focuses on the top 5 m of the system. (G) Temperature field without the clipped range of values, focusing on the bottom 5 m of the system.

the top of the system, which sinks into the system (see Figure 4.6 A), However, unlike the reference simulation, crystal layering also forms at the top boundary in addition to the layering at the bottom, as shown in Figures 4.6 B and C.

The bottom of the chamber receives little contributions of crystals from the top boundary resulting in the formation of a homogeneous layer which had a similar SiO_2 and H_2O content to the bulk composition outlined in Table 4.1. This layer is roughly 1 m thick by the end of the simulation and has a bubble content of 5 vol% and a density of 2800 kg/m^3 (Figure 4.6 C and D). The crystal layering at the top reaches approximately 1/2 m width and had a higher bubble content of 12 vol%, this layer had a lower density of 2725 kg/m^3 which can be attributed to its higher SiO_2 and H_2O fraction 67 wt% and 5 wt% respectively, as well as the higher bubble content.

The higher viscosity and density of the system result in significantly slower whole system convective speeds, which were on average 11 m/hr compared to 52 m/hr in the baseline Figure 4.6 E. The slower convective and crystal settling speed (5.06×10^{-6} m/hr) facilitates the accumulation of crystals and bubbles at the top boundary. Both layers at the top and bottom cool down considerably due to their contact with the cooler wall rock (See Figure 4.6 F and G).

4.3 Closed System Geochemistry

One of the primary aims of this research is to understand how the internal dynamics of shallow systems influence geochemical trends. To achieve this, a suite of geochemical data was included in the simulations to analyse the resulting signatures. This suite includes major oxides (SiO_2, TiO_2, Al_2O_3, FeO, MgO, CaO, Na_2O, and K_2O) and four trace elements ranging from incompatible to compatible. Post-processing of the geochemical data produced Harker plots and trace element spider diagrams, providing further insights into the geochemical behaviours.

Harker plots were constructed by plotting the major oxide concentrations against SiO_2 for each grid cell within the system, including the solid crystal and liquid melt phases. All Harker plots are normalised to the anhydrous sum. Since water cannot partition into the solid phase, no hydrous minerals form within the model; therefore, normalising by the anhydrous sum excludes any consideration of water in the whole rock analysis. The initial input magma anhydrous compositions are outlined in Table 4.3. These plots were colour-mapped to the temperature field, allowing for an interpretation of the data's spatial location within the system. The Harker plots are displayed in figures with accompanying temperature fields and are presented as videos within the Supplemental Material.

Mineral proportions including feldspar, pyroxene, olivine, and quartz—are derived from the model's pseudo-components and are reported consistently as weight percentages (see Appendix 7.1 for the complete list of mineral systems and end members considered within the model).

Magma	**SiO_2**	**TiO_2**	**Al_2O_3**	**FeO**	**MgO**	**CaO**	**Na_2O**	**K_2O**	**Units**
Resident	57.66	1.06	15.35	9.34	5.08	6.24	4.02	1.25	wt%
Recharge	52.07	1.16	18.35	9.66	5.78	9.31	3.04	0.63	wt%

Table 4.3: The initial compositions of the two input magmas: resident and recharge, normalised to the anhydrous sum.

The four trace elements are not real-world but serve as tracers for fractional crystallisation processes in the closed system. Their partition coefficients were chosen to represent strongly incompatible, slightly incompatible, compatible, and strongly compatible behaviours, capturing the range of partitioning dynamics during crystallisation. The trace elements were assigned Initial concentrations of dimensionless values between 0.3 and 3 to show clear contrasts between compatible and incompatible behaviour.

As mentioned previously, the closed system simulations contain a single magma composition like that of an andesite, as outlined in Table 4.3. Throughout the simulation, the geochemical composition evolves without external inputs from recharge or crustal assimilation. The model time elapsed within the one-month real-world simulation period ranges from 11 to 83 hr across the 10 closed system simulations, reflecting diverse internal dynamic complexities. None of the simulations achieves more than a tenth crystallisation of the system, resulting in limited compositional variation. Nonetheless, they provide insights into the early stages of fractional crystallisation trends.

4.3.1 Geochemical Behaviour: Closed Reference Simulation

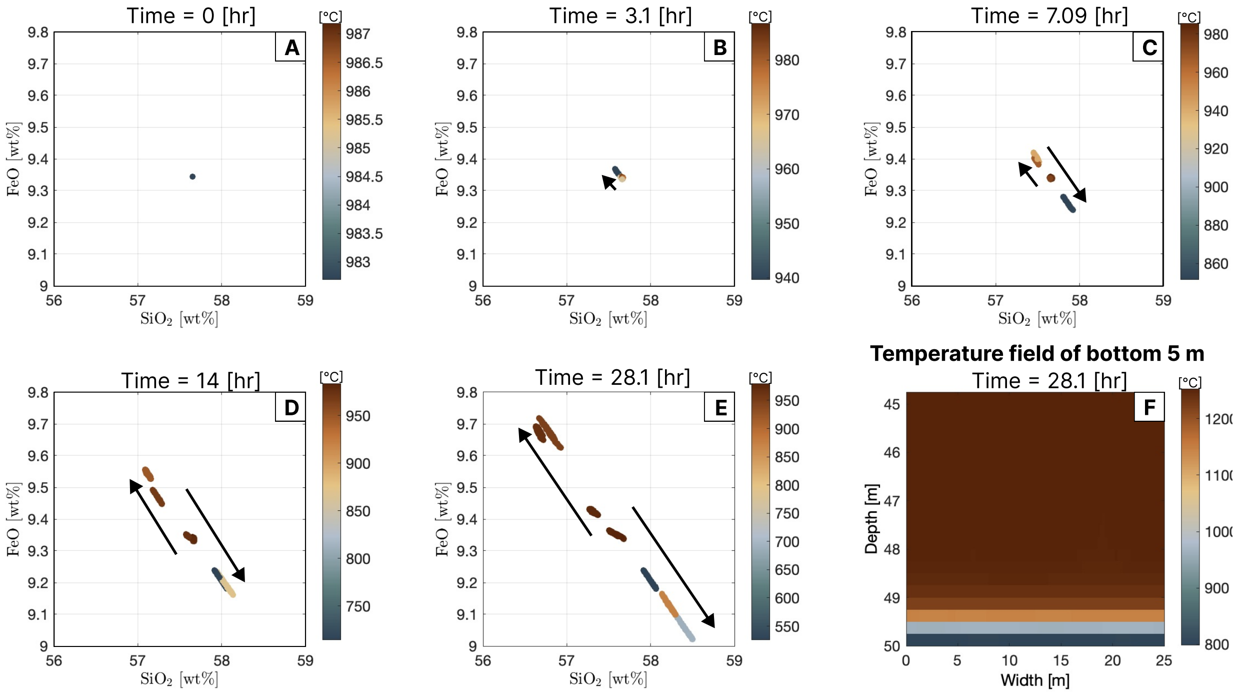

Figure 4.7: Iron Oxide (FeO) Harker plots from the closed reference simulation (Normalised to the anhydrous sum). (A–E) depict the Harker plots at different time frames through the simulation from 0 hr within (A) to the end of the simulation at 28.1 hr (E). Each point on the Harker plots represents a data point within the system. The colour of the points are mapped to the temperature field of the system. (F) Depicts the temperature parameter field for the bottom 5 m of the system's domain. This field represents the temperature values corresponding to the colours of the points on the Harker plots, providing insights into the temperature and location of each cluster on the Harker plots. The Harker plots outline the evolution of the system though time, with clusters first depleting in SiO_2 before evolving again and moving over to the right.

In the reference simulation, the initial chemical perturbations set during the model setup are fully mixed within the first hour. As the simulation progresses, the geochemical signature

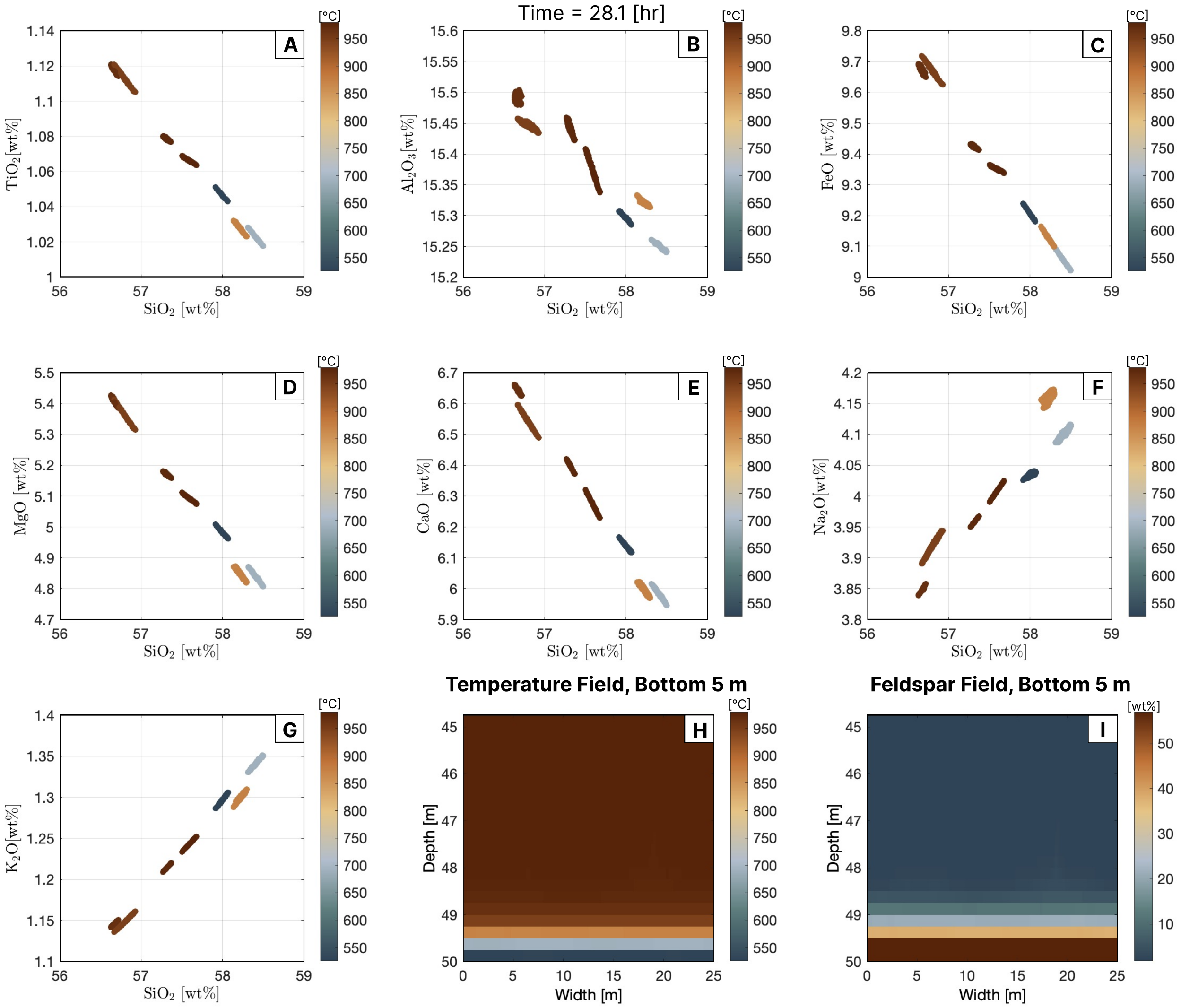

Figure 4.8: Major oxide data from the closed system reference simulation (Normalised to the anhydrous sum), taken at the final time frame (28.1 hr). Each point on the Harker plots represents a data point within the system, with colours indicating the temperature of that point, as mapped to the temperature parameter field. The Harker plots all show straight line trends with: (A) TiO_2, (B) Al_2O_3, (C) FeO, (D) MgO, and (E) CaO, all showing compatible trends and (F) Na_2O and (G) K_2O Harker plots showing incompatible trends. (H) Depicts the temperature parameter field for the bottom 5 m of the system's domain. This field shows the temperature values corresponding to the colours of the points on the Harker plots, providing insights into the temperature distribution and the location of each cluster. (I) Shows the feldspar mineral content for the bottom 5 m of the system. The colour scale represents feldspar content in weight percentage (wt%) within the cumulate layer and above the melt.

gradually evolves through fractional crystallisation. At the bottom of the system, the crystal cumulate layer contains a slightly higher SiO_2 value of 57.8 wt% compared to the bulk composition. The evolution of the cumulate layer is visible in the iron oxide Harker plots (Figure 4.7).

The Harker plots are colour-mapped to the temperature fields to better indicate the geographical locations of the different clusters within the system. From the start of the simulation, the base layer forms a distinct cluster that initially shifts slightly to the left, showing a decrease

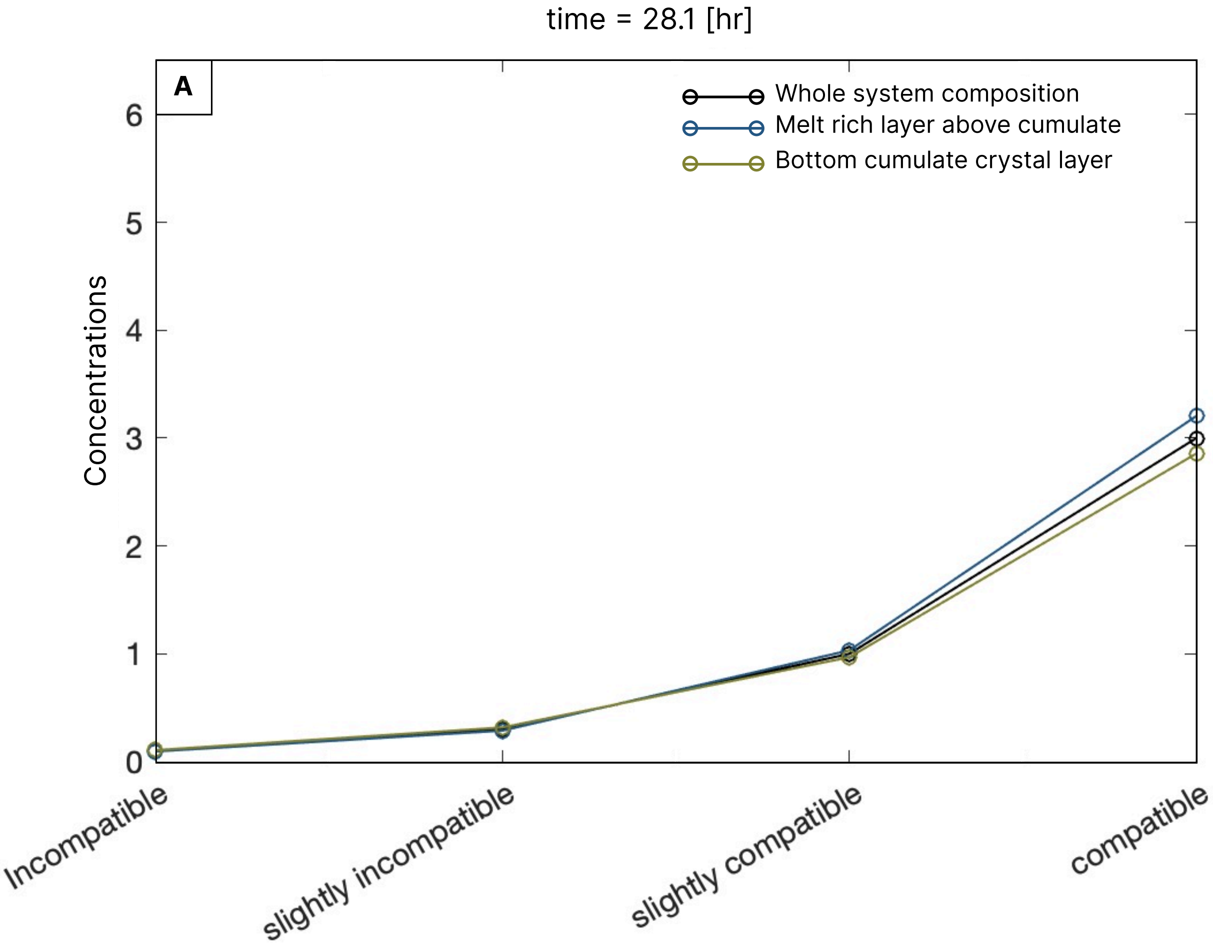

Figure 4.9: Trace element spider diagram showing the four model trace elements at the final frame (28.1 hr) of the closed system reference simulation. Trace elements are ordered from least to most compatible, based on fixed partition coefficients ($K_{tr} = 0.01, 0.10, 3.0, 10.0$). These elements are dimensionless tracers and do not affect the bulk composition. The average trace element composition of the entire system is plotted in black, the melt-rich layer above the cumulate is shown in blue, and the cumulate layer is shown in green. The cumulate is slightly depleted in the most compatible trace elements relative to the system average, while the melt-rich layer is slightly enriched.

in SiO_2 (Figure 4.7 B). Subsequently, it slows and begins to evolve to the right. This is illustrated in Harker plot videos within the Supplemental Material. The layer also shows a decrease in iron oxide content (see Figure 4.7 C). The crystal layers that accumulate above the base layer follow a similar trend: they first move to lower SiO_2 values, then increase in SiO_2 and decrease in iron oxide (Figure 4.6 C-E). The cumulate layer continues to evolve, slowly increasing in SiO_2 content from 57 wt% to 58.4 wt% by the end of the simulation.

Figure 4.8 presents the Harker plots for other major oxides at the end point of the model simulation, illustrating the evolutionary trajectory of the system. Throughout the simulation, the Harker plots display straight-line trends as the system differentiates. Titanium dioxide (Ti_2O), aluminium oxide (Al_2O_3), iron oxide (FeO), magnesium oxide (MgO), and calcium oxide (CaO) all show decreasing oxide values with increasing SiO_2, indicating a relatively small proportion of these oxides being incorporated into the crystals Figuer 4.8 A-E). Conversely, sodium oxide (Na_2O) and potassium oxide (K_2O) show positive trends, suggesting higher incorporation of sodium and potassium into the crystals compared to the surrounding magma Figure 4.8 F-G. This aligns with the mineral composition of the base layer, which is composed of approximately 56.88 wt% feldspar (Figure 4.8 I), 9.35 wt% quartz, 9.97 wt% orthopyroxene, 10.49 wt% clinopyroxene, 3.68 wt% spinel, and 5.87 wt% olivine. The subsequent layers display slightly lower values of Ti_2O, FeO, MgO, CaO, and K_2O, and higher values of Al_2O_3 and Na_2O, indicating a shift towards more pyroxene and spinel and less quartz. By the end of the simulation, the SiO_2 values vary by only 4 wt%, indicating that the system has only slightly evolved within its run time. The trace elements also exhibit minimal variation across the simulation, with the base layer containing bulk concentrations of incompatible, slightly incompatible, and slightly compatible trace elements, as illustrated in Figure 4.9. There is a slight variation in the behaviour of the most compatible trace elements, with the base crystal-dense layer showing a slight depletion of the compatible trace elements relative to the bulk composition. The water/melt-rich layer above the crystal layer shows a slight enrichment of the compatible trace elements relative to the bulk composition, see Figure 4.9.

4.3.2 Geochemistry of the Closed System Parameter Variations

The remaining nine models within the closed system group follow the same geochemical trends as the reference simulation, with only slight variations in major oxide values and the most compatible trace elements. The cumulate layers slowly increase in SiO_2, Na_2O, and K_2O as predominantly feldspar crystallises. Three models that experience plumes within the first ten hours of their runs are outlined and compared to the baseline in Figure 4.10. The simulation with slow wall rock cooling evolves more slowly than the reference simulation; however, due to its longer run time, greater geochemical variation is displayed at the end of the simulation (see Figure 4.10). In this slow wall rock cooling simulation, as time progresses, the layer at the base becomes increasingly enriched in silica, Na_2O, and K_2O. Unlike the other models, the cumulate layer has considerably less quartz. The two simulations with different wall rock cooling rates show variations in the timescales of geochemical evolution, matching the varied crystallisation rates. However, they ultimately display the same geochemical trends.

Figure 4.10 also highlights the major oxide values for the simulation with increased crystal size. Although this simulation follows the same geochemical trend as the reference model, the initial depletion of the base crystal layers before evolving to higher SiO_2 levels is more pronounced, with later crystal layers reducing to 55 wt% SiO_2. Plumes begin to rise from the base of the cumulate layers, which become enriched with H_2O and bubbles. This simulation exhibits the fastest plume onset among all ten models.

The largest variation in geochemical signature is exhibited in the simulation with varied H_2O content, which has half the H_2O content of the base model. This simulation experiences faster cooling, crystal accumulation, and layering at the system's top and bottom. The faster cooling and long in model time of 83.5 hr result in the most evolved geochemical signature of all ten closed system models Figure 4.10.

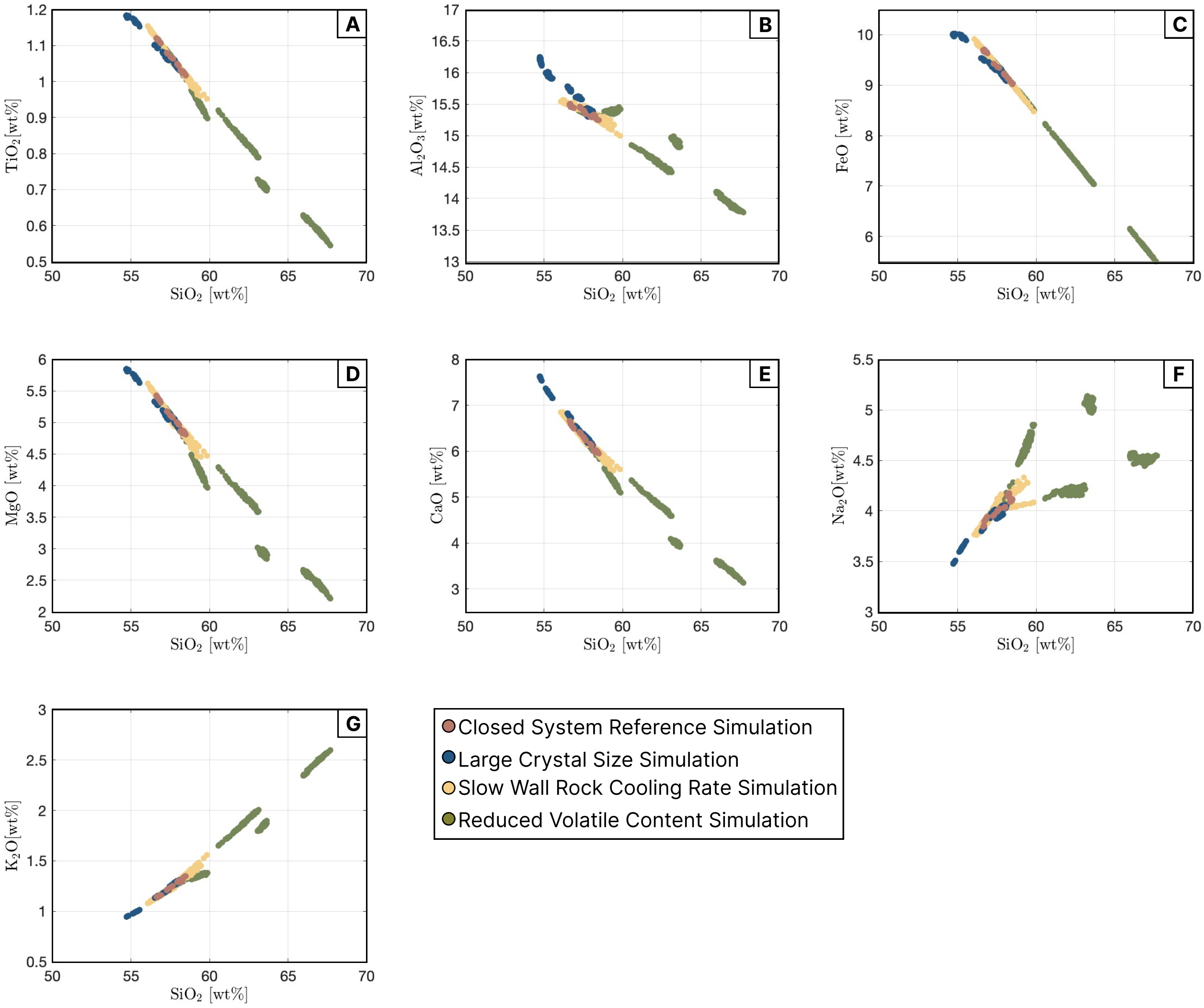

Figure 4.10: Harker plots of major oxide data from four simulations, taken from the final time frame of each model run. The reference simulation is plotted in pink. The larger crystal size simulation (3×10^{-3}) is shown in blue. The slow wall rock cooling rate simulation (48 hr) is plotted in yellow. These simulations exhibit the greatest variation in geochemical trends relative to the reference model within the closed system simulations, with the reduced H_2O content simulation showing the most significant geochemical variations. (A) TiO_2, (B) Al_2O_3, (C) FeO, (D) MgO, (E) CaO, (F) Na_2O, and (G) K_2O.

Figure 4.11 shows that within the varied H_2O content simulation, the crystal layer at the top of the chamber evolves along the same trend as the bottom cumulate layer in the previous simulations. The first crystal layers to form at the top of the chamber become depleted in most of the major oxides (Figure 4.11 A-E) and increase in SiO_2 content, Na_2O, and K_2O (Figure 4.11 F).

As subsequent layers form at the top of the model, each new layer becomes progressively enriched in both Na_2O and SiO_2 (Figure 4.11 F). By the end of the simulation, the uppermost layer contains the most evolved composition within the system, ranging from 67-63 wt% SiO_2 and 5 wt% H_2O. This upper layer is 90 vol% crystalline and is predominantly composed of 57.87 wt% feldspar, 14.63 wt% quartz, 8.12 wt% orthopyroxene, 8.58 wt% clinopyroxene, 2.97 wt%

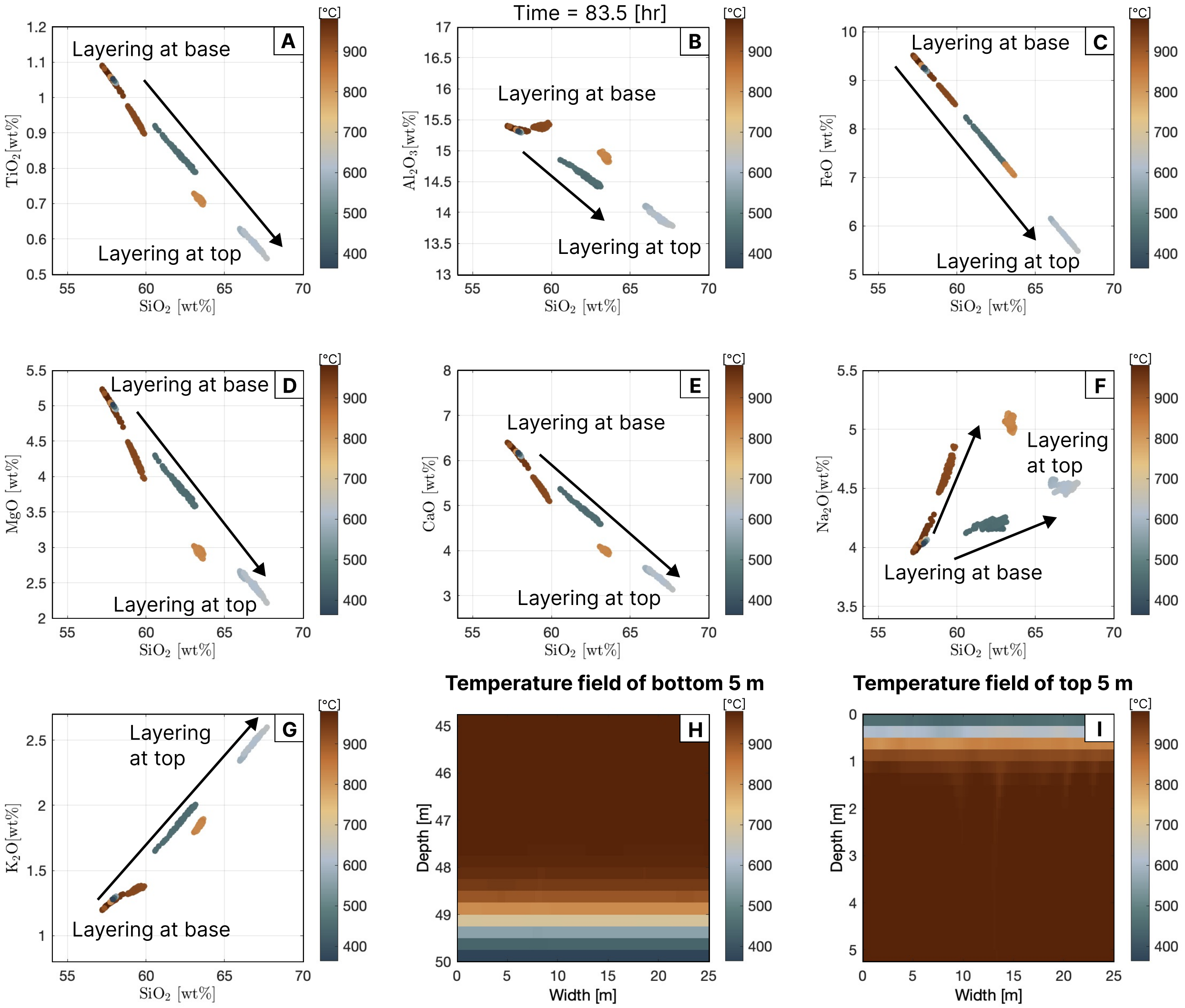

Figure 4.11: Major oxide data from the reduced H_2O content simulation (2 wt%), taken at the final time frame (83.5 hr). Each point on the Harker plots represents a data point within the system, with colours indicating the temperature of that point, as mapped to the temperature parameter field. (A) TiO_2, (B) Al_2O_3, (C) FeO, (D) MgO, and (E) CaO, all showing straight line compatible trends. (F) Na_2O shows two deviating straight line trends and (G) K_2O Harker plot shows an incompatible trend. (H) Depicts the temperature parameter field for the bottom 5 m of the system's domain. (I) Depicts the temperature parameter field for the top 5 m of the system's domain. These fields show the temperature values corresponding to the colours of the points on the Harker plots, providing insights into the temperature distribution and the location of each cluster. These Harker plots show that the top and bottom crystal layers form contrasting geochemical signatures.

spinel, and 4.6 wt% olivine. Some olivine and pyroxene crystals become trapped within the rapidly cooling and crystallising layer, while the majority sink into deeper regions of the system. The co-existence of olivine and quartz within the cumulate is an artefact of the simplified pseudo-phase diagram used in the model; in natural systems, these phases typically do not crystallise together. However, across the simulations, one of the two phases usually occurs only in minor proportions—for example, the 4.6 wt% olivine within the top layer.

Conversely, at the bottom of the model, the crystal layering composition closely resembles that of the bulk composition, with approximately 57 wt% SiO_2 and 2 wt% H_2O. This is evident in the Harker plots (Figure 4.11 A-G), where the base layer forms within the bulk chamber cluster, exhibiting minimal variation throughout the simulation. By the end of the run, the base layer consists of 57.87 wt% feldspar, 9.31 wt% quartz, 10.23 wt% orthopyroxene, 10.75 wt% clinopyroxene, 3.78 wt% spinel, and 6.02 wt% olivine. This is similar to the cumulate compositions across the other closed system simulation see Appendix 7.3. The cumulate at the base contains 6 vol% trapped bubbles. The base of the cumulate is more than 90 vol% crystalline, and the upper portions of the cumulate are approximately 70 vol% crystals, where crystals are still forming and accumulating from the top.

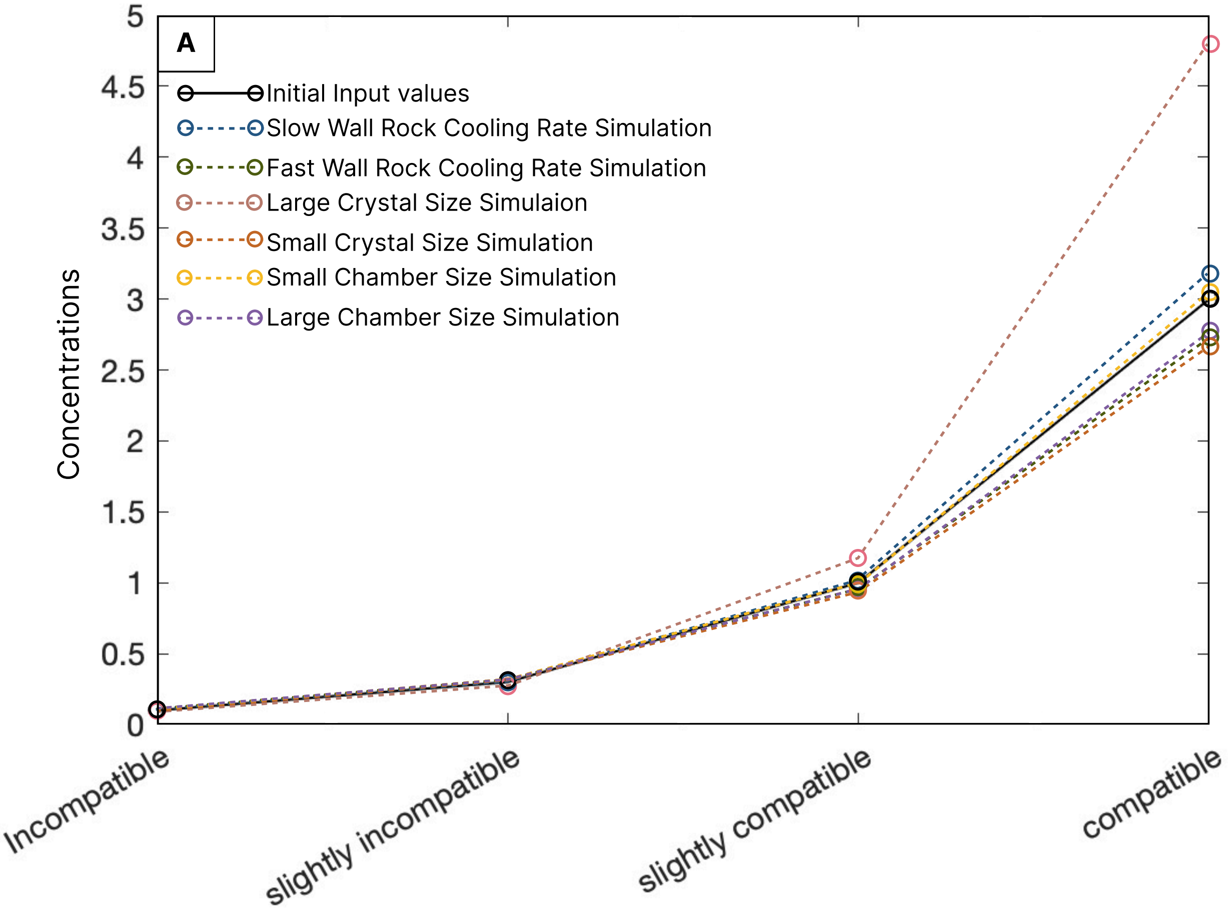

Figure 4.12: Trace element spider diagrams displaying the four trace element values from the final time frame of each end-member simulation across the different parameter variations. Trace elements are ordered from least to most compatible, based on fixed partition coefficients (K_{tr} $= 0.01, 0.10, 3.0, 10.0$). The results show that within the simulations with the fast plume onset, the plume is enriched in the most compatible trace elements. The incompatible trace elements have little to no variation across all the simulations.

The trace elements show minor variations across the ten closed system simulations (Figure 4.12). The three models that experience plume formation within the first 10 hr of simulation (slow wall rock cooling, large crystal size, and smallest chamber size simulations) show slight enrichment in the most compatible trace elements, illustrated in Figure 4.12. The simulations that experience later or no plume formation show a slight depletion of compatible trace elements within the base crystal layer relative to the bulk composition, as illustrated in Figure 4.12. One outlier is the large crystal size simulation, which exhibits considerably higher concentrations of compatible trace elements in its base layer (Figure 4.12).

Finally, the trace element signatures for the varied H_2O simulation reveal interesting trends between the top and bottom layers. At the bottom layer, there is a slight depletion of compatible trace elements, contrary to the expected trend. This discrepancy suggests there may be an inconsistency in the model version used. Later models show a more typical increase in compatible elements within the cumulate stack. The top layer, however, displays a slightly enriched compatible trace element signature (Figure 4.12). There is little to no variation in the incompatible trace element concentrations across all ten closed system runs.

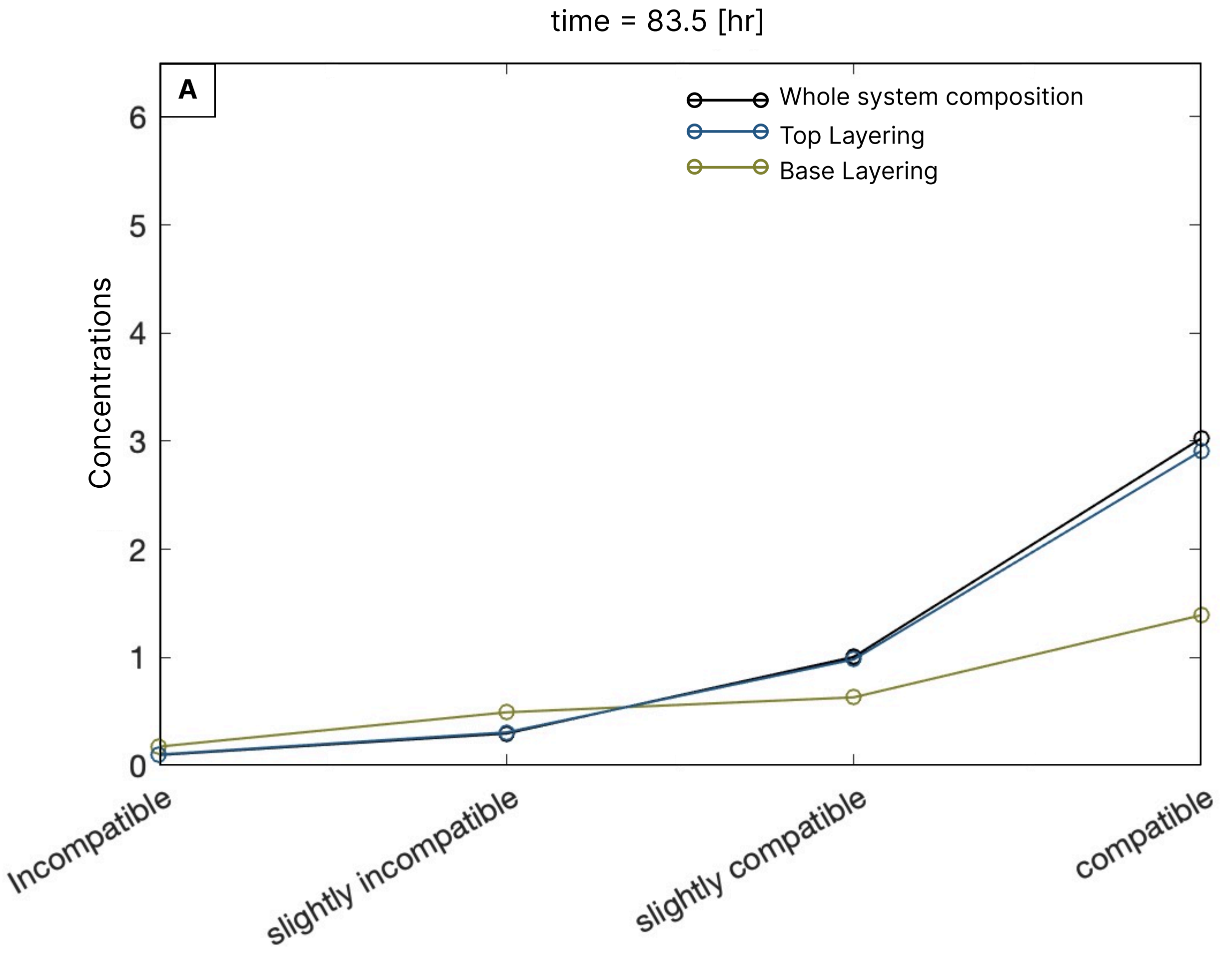

Figure 4.13: Trace element spider diagram displaying the four trace element values from the last time frame (83.5 hr) of the varied H_2O content simulation (2 wt% water). The whole system composition is plotted in black. The top crystal layer is shown in blue, and the bottom crystal layer is plotted in green. This highlights the differing composition between the top and bottom crystal layers.

4.4 Open System Dynamics

The second group of simulations introduces a second basaltic magma composition outlined in Table 4.3; this magma is hotter and more primitive than the resident magma to simulate recharge from the deeper, hotter crustal magmatic system. The primary aim of the open system models is to assess the effects of introducing a second magma on the internal dynamics and geochemistry. Additionally, they assess the post-recharge convective influences on the extent of mixing and preservation of the geochemical signatures of the primitive magma. The first model within this group serves as the open system reference simulation from which all other models vary. Table 4.4 outlines all the models within this group and their parameter values. Three parameter tests are conducted: varying the volume of recharging magma, the initial temperature of both magmas and the H_2O content of both the resident and recharge magma.

Model ID	Recharge Volume [%]	Resident water [wt%]	Recharge water [wt%]	Resident temperature [°C]	Recharge temperature [°C]
Open_Reference	20	4	2	985	1235
Smallest_Rech_volume_5	**5**	4	2	985	1235
Small_Rech_volume_10	**10**	4	2	985	1235
Small_Rech_volume_15	**15**	4	2	985	1235
Large_Rech_volume_30	**30**	4	2	985	1235
Large_Rech_volume_40	**40**	4	2	985	1235
Largest_Rech_volume_50	**50**	4	2	985	1235
Equal_Water	20	4	**4**	985	1235
High_Water_Rech_1	20	4	**5**	985	1235
Higher_Water_Rech_2	20	**2**	**4**	985	1235
Lower_Res_temp_973	20	4	2	**973**	1235
Lower_Res_temp_968	20	4	2	**968**	1235
Lower_Res_temp_959	20	4	2	**959**	1235
Lower_Rech_temp_1200	20	4	2	985	**1200**
Higher_Rech_temp_1270	20	4	2	985	**1270**

Table 4.4: Table of open system models with their ID values, and parameter values for the recharge volume, H_2O content, and temperature of both magma compositions. Varied values are in bold. (Where "Rech" = Recharge magma and "Res" = Resident magma)

4.4.1 Open System Reference Simulation

When the reference model is initiated, a layer forms at the interface between the two magma compositions. This layer persists throughout the model run, acting as a hybridisation zone where the two compositions interact and mix, creating a hybrid composition (see Figure 4.14 A-B). The hybridisation zone dynamics regime is a system where two stratified magma bodies interact only at their interface. Plumes and drips form at this boundary, driving convection cells in both layers and allowing localised mixing and production of a third, hybrid magma composition.

These plumes and drips continue through the simulation, generating two distinct convection cells and forming a layered convection system, see Figure 4.14 B–F see also Supplemental Material for videos of the reference simulation.

Both layers undergo convection for the duration of the model run. Initially, the top layer convects more slowly at 15 m/hr, while the base layer convects more vigorously at 57.6 m/hr due to its higher temperature.

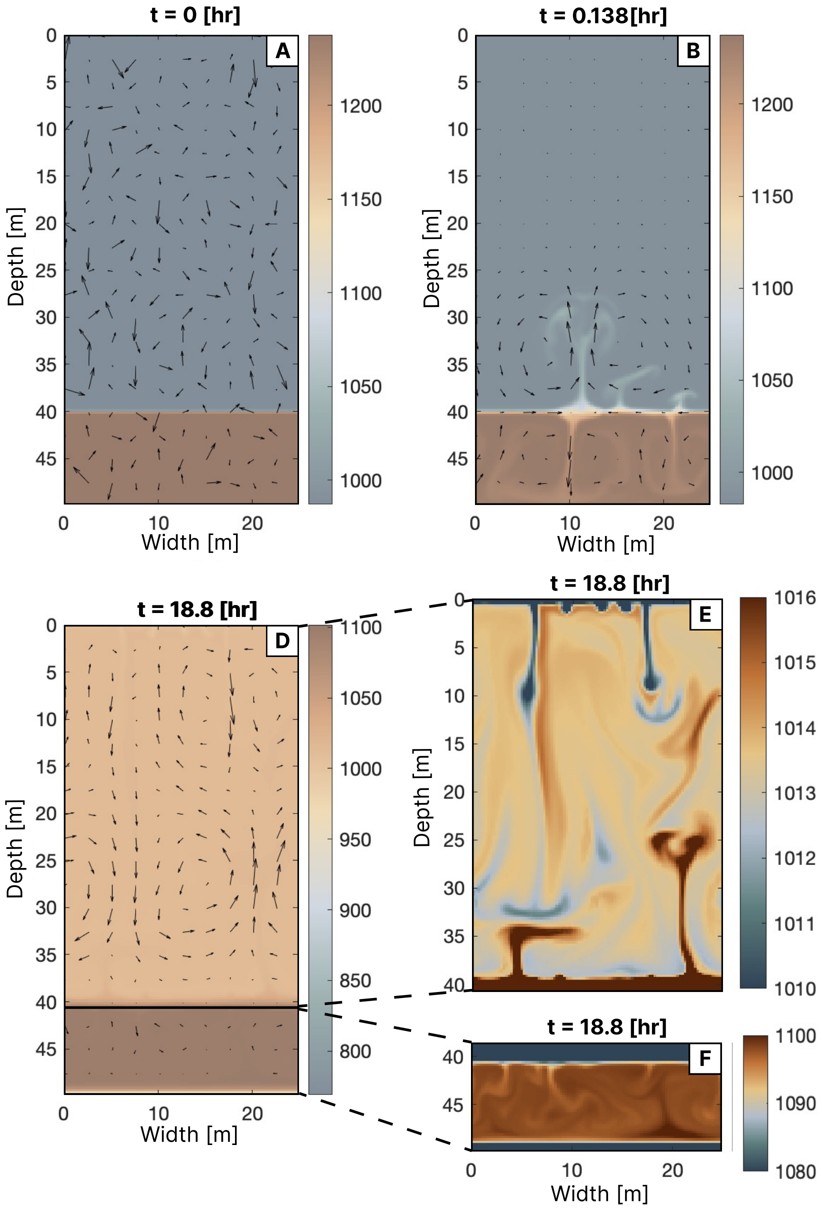

Figure 4.14: Parameter field from the open system reference model at multiple time steps. (A–D) Show temperature values, with the velocity field overlain as a quiver plot indicating the flow's direction and magnitude. They show the evolution of the hybridisation zone regime through time. (E) Depicts the temperature parameter field of the top convecting layer, with a clipped range of temperatures between 1016°C and 1010°C. Highlighting the internal dynamics, plumes, drips and layer convection. (F) Depicts the temperature field of the bottom convecting layers, showing temperature values between 1100°C to 1080°C, again highlighting the internal dynamics of the layer.

The convection speeds fluctuate throughout the first three hours as the two layers gradually equilibrate in temperature (see Figure 4.14 D). As the base layer cools, its convection slows, while the upper layer becomes more vigorous, driven by the heat from rising plumes originating in the hybridisation zone. After three hours, both layers begin to settle, and their convective speeds decrease as the simulation progresses. By 17 hr, the top layer is convecting at 63 m/hr, while the base layer has slowed to just 13 m/hr. This difference in convection rates is reflected in their mean Rayleigh numbers, with the top layer at 2,700 and the base layer at 827.2. During the first hour of the simulation, drips form at the domain's roof and sink into the system, similar to the behaviour observed in the closed system simulations, illustrated in Figure 4.14 E. As the model progresses, a crystal-rich layer begins forming at the bottom of the simulated chamber, gradually accumulating over time. By the end of the simulation, this base cumulate layer reaches approximately 90 vol% crystals. Very little bubble phase is present throughout the simulation, with bubbles only beginning to exsolve around 9.33 hr into the run. The bubbles exsolve within the cumulate layering as it reaches 50 vol% crystals and become trapped.

4.4.2 Recharge Volume Variation

The first open system parameter test varies the recharge volume added to the system, ranging from 5-50 % of the total system volume, across six simulations (outlined in Table 4.4). The variation in recharge volume is depicted in Figure 4.15 A-C.

Across all six simulations, a consistent dynamic behaviour emerges, characterised by the formation of a thin hybridisation zone where the two magmas mix. This behaviour is similar to the dynamics observed in the reference simulations. In each case, two distinct convection cells develop within the magma layers. However, the convective speeds vary between them.

In the simulation with the smaller recharge volume (5 % of the system), the thin recharging layer convects significantly slower than in the reference simulation, at approximately 20 m/hr Figure 4.15 A and B). As observed in the closed system parameter tests with different chamber sizes, the convection speed is related to the layer's size (See Equation 3.8). As the simulation progresses, both convection cells slow down, and by the end, the top resident magma layer is convecting at 32 m/hr, while convection in the base layer almost ceases, slowing to 0.17 m/hr.

In contrast, in the simulation with a large recharge volume (50 % of the system), the bottom convection cell convects much faster, at around 200 m/hr. This simulation follows a similar trend with both convection cells slowing over time. By the end of the simulation, the top layer is convecting at 120 m/hr, and the base layer at 106 m/hr (Figure 4.15 C).

The variation in recharge volume not only affects convective speeds but also influences the system's temperature profile. As the two magmas interact, the cooler resident magma warms while the recharging magma cools as they equilibrate. As recharge volume increases, the resident magma heats more quickly. In the small recharge volume simulation (5% recharge), the resident magma's temperature increases by 0.92°C/hr. In contrast, in the large recharge simulation (50% recharge), the resident magma heats much faster at 9.61°C/hr. The cooling rate of the recharge magma also depends on the recharge volume. In the small recharge simulation, the recharge

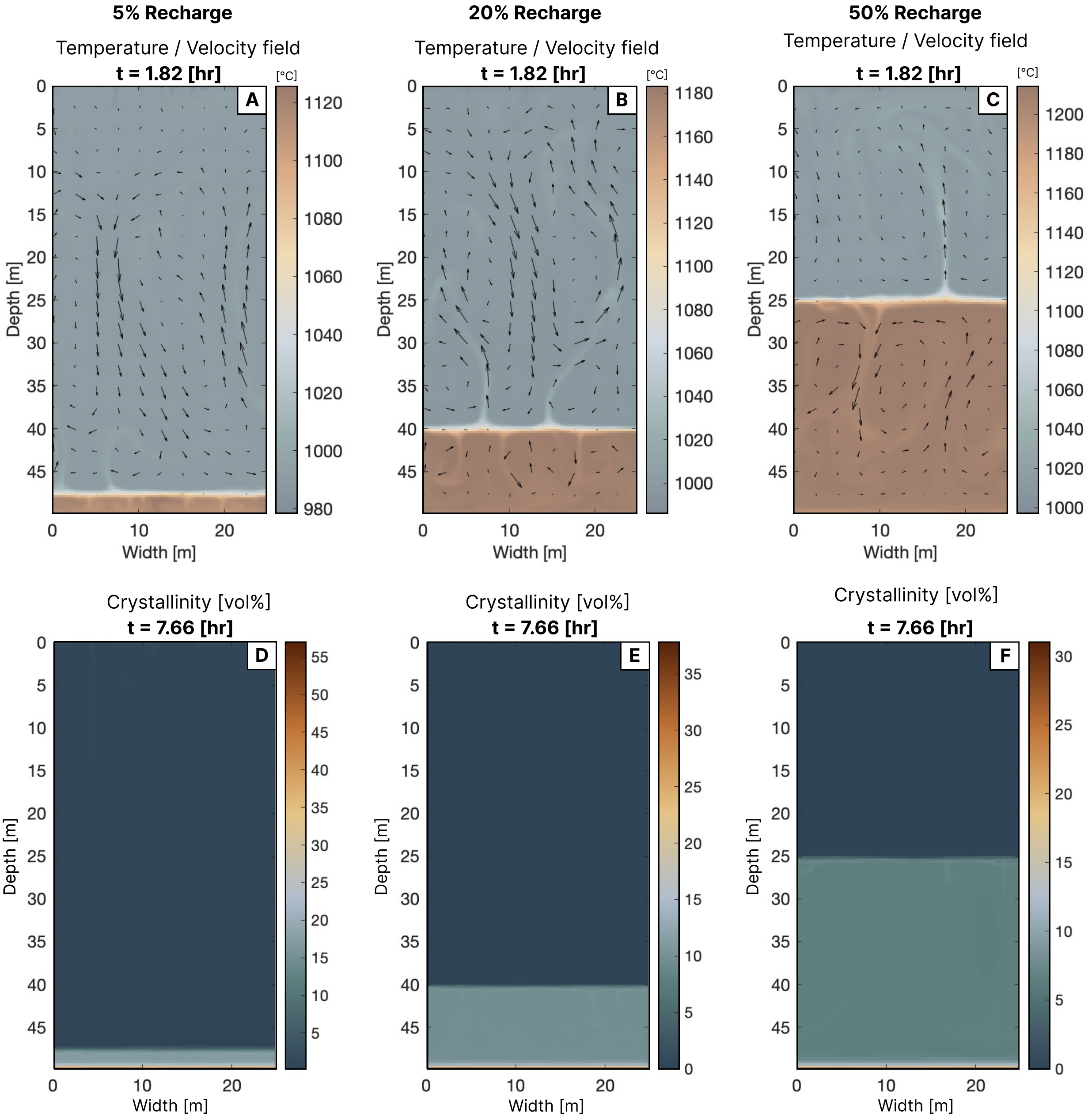

Figure 4.15: Parameter fields from the smallest (5 vol% recharge) and the largest (50 vol% recharge) varied recharge volume simulations compared against the open system reference simulation (20 vol% recharge). (A–C) Depict temperature parameter fields with the velocity field overlaid as a quiver plot, indicating the direction and magnitude of flow. Both varied recharge volume simulations display the same internal dynamics regime as the reference simulation. All panels show the dynamics at 1.82 hr for consistency. (D–F) Show the crystal volume percent (vol%) for the three simulations at the same time frame of 7.66 hr, highlighting the varied crystal volumes. In the small recharge simulation, the base layer contains 55 vol% crystals, while in the large recharge simulation, it contains 30 vol% crystals.

magma cools rapidly at 22°C/hr, while in the large system, it cools more slowly at 8.29°C/hr.

Another notable difference among the models is the presence of bubbles. Bubbles are observed in models with smaller recharge volumes, where they exsolve and accumulate in the base crystal layers. Bubbles are absent within the large recharge volume simulations. A smaller, cooler, and less convective layer within the low recharge simulation leads to increased crystal formation, faster accumulation, and crystallisation. By 7.66 hr, the base layering within the small recharge system reaches 55 vol% crystals, comparatively the 20 vol% recharge system reaches 35 vol% crystals, and the 50 vol% recharge system reaches 30 vol% crystals by 7.66 hr (Figure 4.15 D-F).

The second parameter test varies the initial temperature values of both magmas across five simulations. In each case, the same hybridisation dynamic regime is observed, featuring the formation of two convection cells. Cooling and crystallisation occur, with crystals settling at the base. This dynamic regime is similar to that seen in the varied recharge simulations. Each simulation also displays consistent patterns in cooling, crystallisation, and bubble behaviour. For further details, see Appendix 7.2.

4.4.3 Water Content Variation

The final parameter test within the open system simulations includes three simulations, each exploring different H_2O contents in the recharge and resident magmas. Unlike the reference and previously discussed simulations, which feature a recharge magma composition depleted in water relative to the resident magma, this test examines scenarios with equal H_2O contents and a volatile-enriched recharge. These scenarios reflect the volatile-rich magmas from deeper subduction zones and the volatile-depleted resident magmas in the continental crust. Table 4.4 details the three simulations in this test. These variations significantly impact the internal dynamics, with each simulation exhibiting a distinct dynamic regime, outlined below.

Equal Water Contents

Initially, the dynamics of this model closely resemble those of the reference simulation, with upwellings and downwelling's forming at the contact between the two magma compositions. This interaction creates a hybridisation zone and two convecting cells (Figure 4.16 A–B). From this hybridisation zone, hot plumes rise into the resident magma, while cooler drips sink into the recharge magma. Both magmas contain 4 wt% H_2O, but their saturation points are different due to temperature dependence. At the start of the model run, the resident magma is just below H_2O saturation, while the hotter recharge magma exceeds it, leading to bubble exsolution. These bubbles rise towards the hybridisation zone (the boundary between the two magmas) and accumulate there. This process depletes the lower part of the system (recharge magma) of H_2O and bubbles and forms a three-layered convective system (Figure 4.16 C). The top layer convects at approximately 101 m/hr, the central bubble-rich layer at 89 m/hr, and the bottom layer at 32 m/hr.

In the central layer, crystals remain entrained due to their lower density compared to the base magma. This increases the crystallinity of the layer from 0 vol% to around 5 vol% by 1.77 hr (see Figure 4.16 D). At 1.5 hr, the crystals begin to settle across the boundary and accumulate at the bottom of the system, see Figure 4.16 E. At around 8.56 hr, bubbles within the bottom recharge layer rise towards the central bubble-rich layer; however, they do not cross the boundary due to density contrasts, which creates a transient fourth convecting layer. This

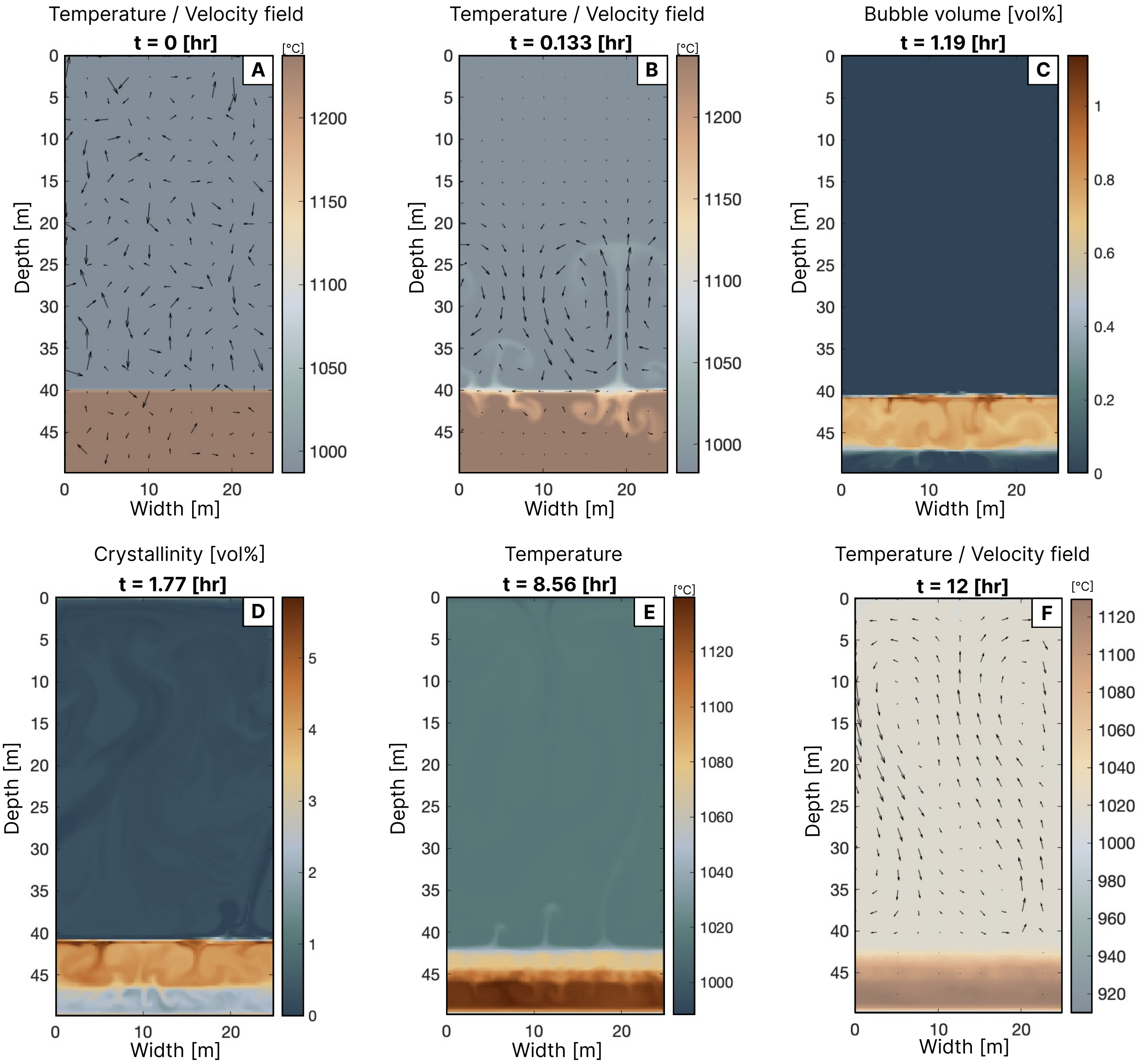

Figure 4.16: Parameter fields from the equal H_2O content simulation taken at various points in time. (A) The temperature field with the velocity field is overlaid as a quiver plot, indicating the direction and magnitude of flow and depicting the internal setup before the run begins. (B) The temperature field at 0.13 hr after initiation, highlighting the rapid interaction between the two magmas. (C) The bubble volume percentage (vol%) parameter field at 1.19 hr shows the bubble-rich layer sandwiched between two depleted layers. (D) Crystallinity (vol%) parameter field at 1.77 hr, highlighting the high crystal content of the middle layer. (E) The temperature parameter field at 8.56 hr, showing the development of four convecting layers. (F) Temperature and velocity field quiver plots at the end frame of the simulation, showing the system has settled into a three-layer convective regime, with minimal movement in the lower layers.

fourth layer does not last long as it equilibrates with the bubble-rich layer above and they merge (4.16 E). As the simulation progresses, the middle bubble-rich layer shrinks from 15 m to less than a metre as the bubbles slowly migrate upwards across the boundary into the upper resident magma layer, where they redissolve back into the melt Figure 4.16 F.

High Water Recharge (1 vol% difference)

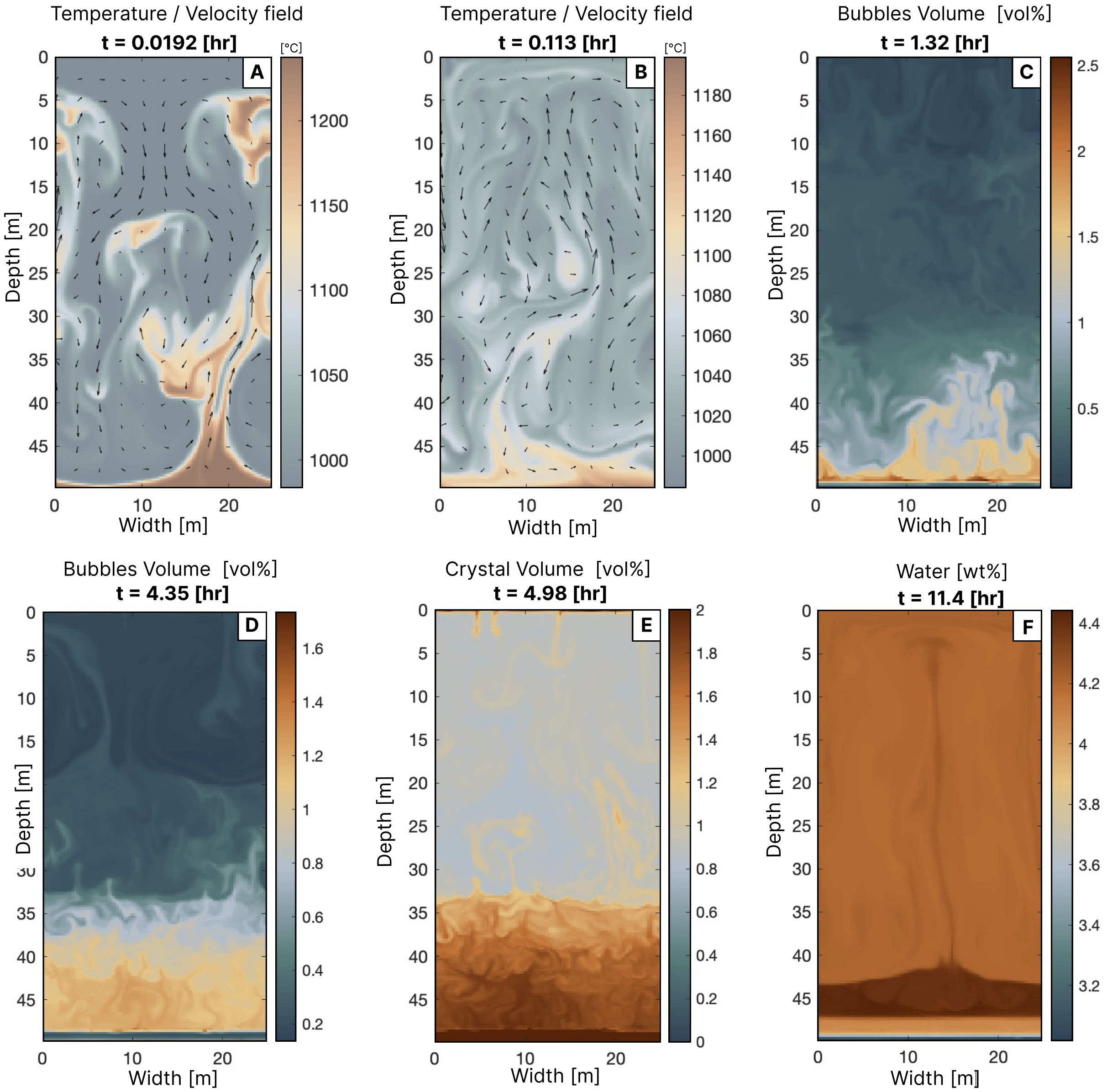

Figure 4.17: Depicts several parameter fields through time from the high H_2O recharge (1 vol% difference) simulation. (A) The temperature and velocity fields within the first minute of the simulation highlight the system overturn event. (B) The temperature field a few minutes later illustrates the rapid nature of the overturn and the extent of mixing within a short period. (C) Bubble volume percentage (vol %) parameter field, showing the bubbles' location at the system's base. (D) Bubble volume percentage (vol %) field at 4.35 hr, depicting the evolution of layering and heterogeneity as the bubbles rise. (E) Crystallinity parameter field (vol %), showing values between 0 vol %) and 2 vol % to highlight the crystal volume at the system's base versus the top. This helps to counteract the bubble buoyancy, preventing a second overturn. (F) Water parameter field (wt%) at 11.4 hr, highlighting the location of the water-rich layer and the dynamic interactions between layers, including the draining of H_2O from this layer to the depleted layer above via plumes.

Within this simulation, the resident magma contains 4 wt% water, while the recharging magma contains 5 wt%. This setup creates a density contrast between the layers, with the bottom layer having a density of 2422 kg/m^3 and the top layer having a density of 2424 kg/m^3. At the start of the simulation, the density contrast causes the system to overturn, with the recharging magma rising to the top of the chamber and mixing with the resident magma, as shown in Figure 4.17 A. The recharge magma then sinks back down to the base of the system (see Figure 4.17 B). Following the initial overturn event, the system experiences significant homogenisation, and the sharp density contrast that initially triggered the overturn almost completely disappears.

As the system settles, it stratifies into layers with a diffuse boundary between them. These layers show differences in temperature, viscosity, chemical compositions, and bubble content; however, these contrasts are less extreme than the initial model setup (Figure 4.17 C). The system further stratifies, forming two layers. At the top of the system is a cooler, bubble-poor layer, and at the bottom, there is a hotter, bubble-rich layer (Figure 4.17 D). Despite conditions appearing to favour another overturn, it does not occur. The base layer, while still hotter and more bubble-rich, becomes slightly denser than the top layer due to cooling, bubble loss, and increased crystallinity. This increased density in the bottom layer stabilises the system.

Several factors contribute to this stability. The increased crystallinity in the base layer enhances its density and viscosity (Figure 4.17 E), counteracting the bubble buoyancy. Initially, the base layer is less viscous (0.6 Pa s) than the top layer (2.2 Pa s), but as the bubbles exsolve and the base cools, its viscosity increases to 1.4 Pa s. While a viscosity difference persists, it diminishes over time. The compositional contrast between the felsic, buoyant top layer and the more mafic, dense base layer also contributes to stability, particularly as the loss of bubbles and heat in the lower layer reduces its buoyancy.

Crystal-rich drips form at the top of the chamber and sink, while a thin crystal cumulate layer accumulates at the bottom of the system. Water and bubble-rich plumes begin to rise from the bottom layer and migrate into the upper layer (Figure 4.17 D-E).

Between 4-11 hr, transient interstitial layers of varied H_2O volumes form between the bubble-rich and bubble-poor sections of the system (Figure 4.17 D-F). The system continues to stratify, forming a three-layered convective regime with a water-enriched layer between the two more depleted layers see Figure 4.17 F.

As the model progresses, bubbles continue to rise and redissolve within the top layer. The central water-rich layer reduces in width from 15 m to less than 1 m by the end of the simulation, as water escapes via plumes. Simultaneously, the depleted layer beneath steadily grows in thickness, as illustrated in Figure 4.17 F. The model output reflects the dynamics seen in the previous simulation, with less stable boundary stratification. By the end of the 17 hr run, the system is stably stratified into two homogeneous melt layers, with a thin layer of crystal accumulation at the base.

High Water Recharge (2 vol% difference)

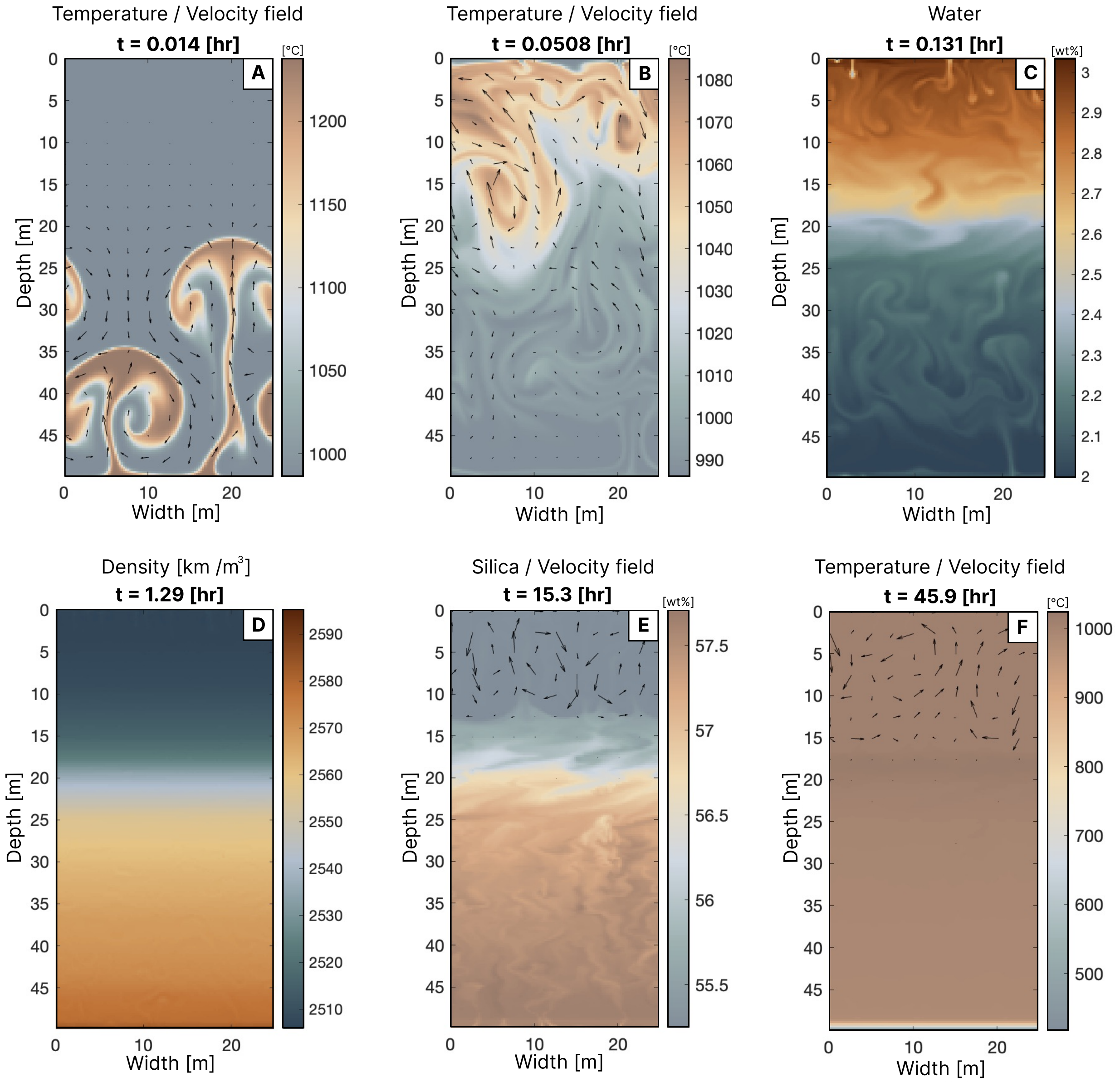

Figure 4.18: Depicts several parameter fields through time from the High Water Recharge (2 vol% difference) simulation. (A) Temperature parameter field with the velocity field overlain as a quiver plot, indicating direction and magnitude of flow. This highlights the initial overturn of the system, showing plumes of recharge magma rising from the base into the system. (B) Temperature and quiver plot a few moments later, showing the recharge magma settling as a layer at the top of the system. (C) The water content (wt %) field highlights plumes and drips extending into the system from the boundaries. (D) Density field showing the stable density stratification of the system within 1.29 hr. (E) SiO_2 parameter field (wt%) with the velocity field overlain as a quiver plot, indicating homogenisation within the top convecting cell. This plot also highlights the chemical diversity within the lower layer despite its stable density stratification. (F) Temperature and velocity field of the last frame of the model, indicating the equilibration of temperature and the convecting cell at the roof of the system.

The final simulation in this parameter test examines a scenario where the resident magma contains 2 wt% H_2O, half the H_2O content of the reference case. While the recharging magma contains double that amount at 4 wt%, outlined in Table 4.4. This simulation is designed to simulate H_2O rich magma recharge that originated deep within the subduction zone.

Upon initiation of the simulation, the system undergoes rapid overturn within the first few minutes, similar to the previous model. The less dense recharging magma rises to the top of the system, see Figure 4.18 A. However, unlike the previous simulation, the recharge magma does not sink again. Instead, it accumulates at the top, resulting in a two-layer stratified system. This can be seen in Figure 4.18 B. The top layer is composed of H_2O rich, less dense magma, while the denser, cooler and more viscous magma remains at the bottom. The initial bubbles from the recharge magma that lowered the density, triggering the overturn event, quickly redissolve into the melt, and the bubble content drops to zero.

A diffuse boundary layer forms between the two magma compositions, creating a thin interface. Plumes begin to form at the bottom wall rock boundary and rise into the system. Simultaneously, crystal drips descend from the top wall rock contact as depicted in Figure 4.18 C.

As the simulation progresses, convection diminishes, and by 1.5 hr, two-thirds of the chamber have stabilised into a stratified density. With no driving force, all movement slows to almost zero (Figure 4.18 D). The plumes at the bottom appear to become static. Crystallisation persists at the top and bottom wall rock contacts, with a crystal cumulate layer forming at the base and crystal drips forming at the top.

Over time, the crystal drips from the top form a small, localised convection cell, which expands slowly as it erodes the stable layers below (see Figure 4.18 E). Small plumes rise from the eroded boundary as this convection cell grows. By the end of the simulation, the convection cell grows to roughly 25 m in width.

Throughout the 45.9 hr simulation, physical properties such as temperature, density, viscosity and crystal content become evenly distributed throughout the system. Meanwhile, the geochemical properties including SiO_2 H_2O and major oxide values, maintained distinct layers. This contrast can be seen across Figure 4.18 D-F.

4.5 Open System Geochemistry

The open system simulations see the introduction of a second recharge magma composition similar to that of a basalt emplaced at the base of the chamber. Both compositions are outlined in Table 4.3.

4.5.1 Geochemical Behaviour: Open Reference Simulation

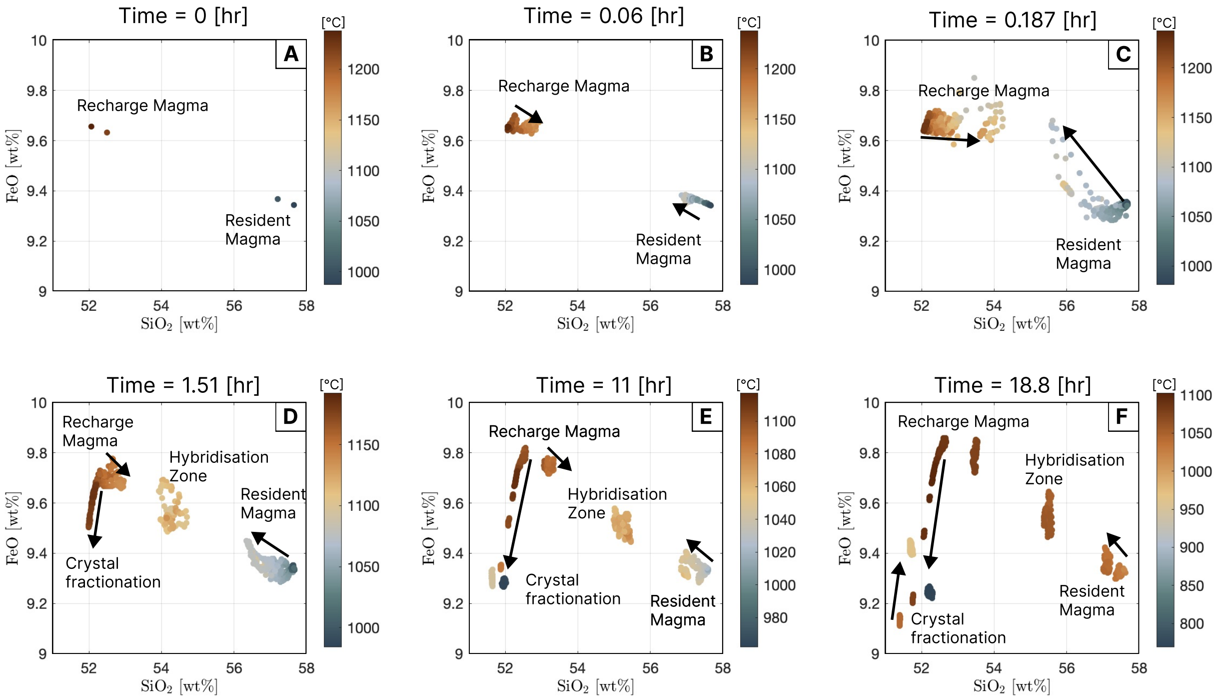

Figure 4.19: Iron Oxide (FeO) Harker plots from the open reference simulation. (A–E) depict the Harker plots at different time frames through the simulation from 0 hr within (A) to the end of the simulation at 18.8 hr (F). Each point on the Harker plots represents a data point within the system. The colour of the points are mapped to the temperature field of the system. The initial geochemical signature of the system shows the two magmas plotting as distinct compositions. (B–E) show the system's evolution over time with the formation of a hybridisation zone. (F) depicts the geochemical signature at the end of the simulation, showing the two end members, the hybridisation zone between them, and the fractional crystallisation trends within the base crystal layers.

The open system reference simulation's major oxide evolution is outlined in Figure 4.19, depicted as Harker plots. Initially, the two magmas plot as distinct clusters with the resident magma containing 57.66 wt% SiO_2 and the recharge magma containing 52.07 wt% SiO_2 (Figure 4.19 A). As mixing occurs across the hybridisation zone, the geochemical signatures of the magmas converge, forming a third composition at the interface (Figure 4.19 B-C). Although the two magmas mix in the hybridisation zone to create a third composition, large parts of the system remain unmixed (Figure 4.19 D). The crystals that form and accumulate at the bottom of the system initially deplete in FeO and SiO_2. They then increase again as crystallisation progresses, Figure 4.19 D-F. This behaviour mirrors the SiO_2 patterns observed within the closed system simulations. As the simulation continues, crystallisation continues creating a fractionation trend Figure 4.19 F. The Harker plots provide insights into the competing influences of the recharge/mixing and fractionation.

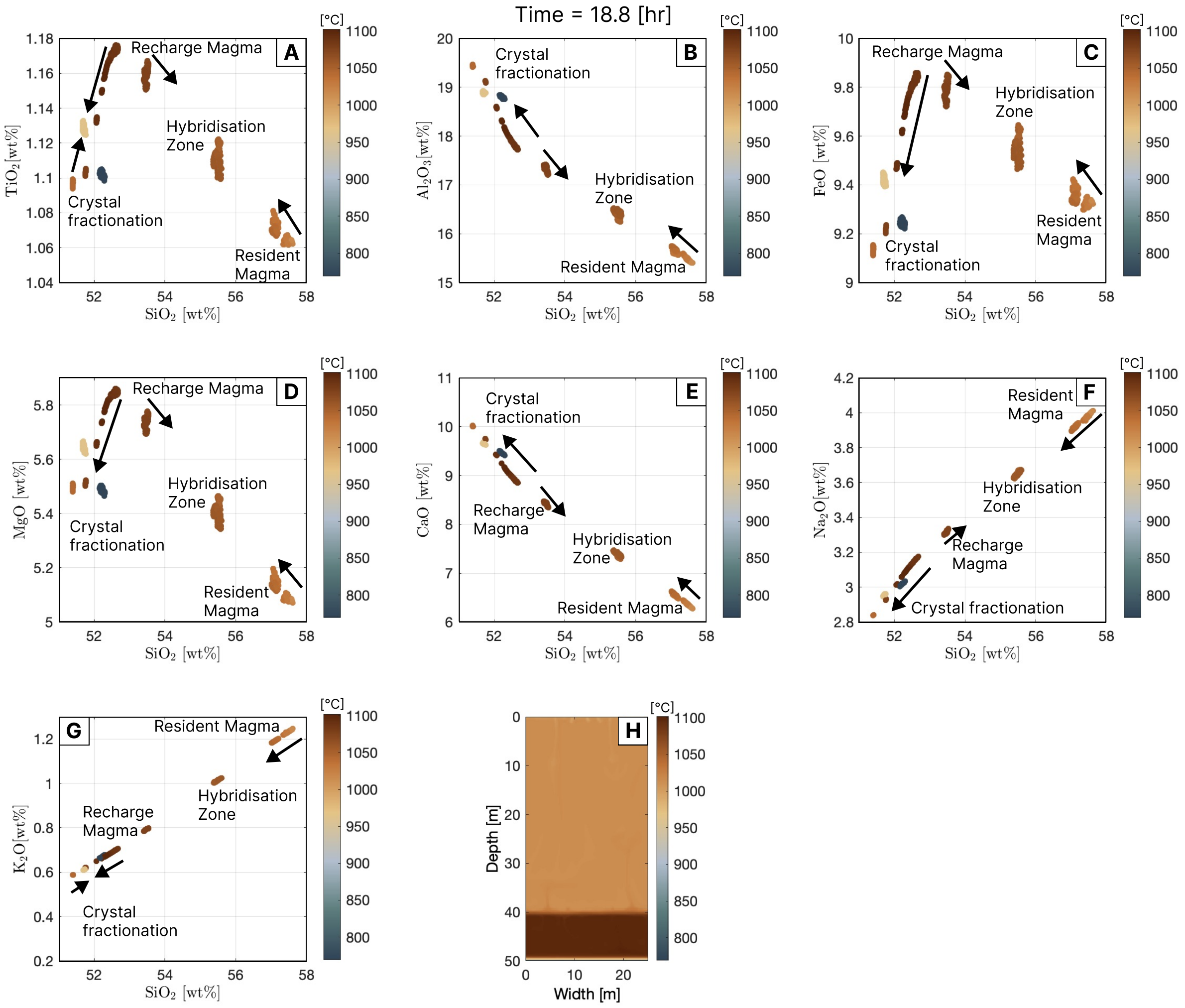

Figure 4.20: Major oxide data from the open system reference simulation, taken at the final time frame (18.8 hr). Each point on the Harker plots represents a data point within the system, with colours indicating the temperature of that point, as mapped to the temperature parameter field. (A) TiO_2, (B) Al_2O_3, (C) FeO, (D) MgO, and (E) CaO, (F) Na_2O, (G) K_2O (H) Depicts the temperature parameter field of the system's domain. This field shows the temperature values corresponding to the colours of the points on the Harker plots, providing insights into the temperature distribution and the location of each cluster. These Harker plots display mixing trends between the two magma compositions as well as a crystal fractionation trend, where crystals accumulate at the bottom of the system.

By the end of the simulation, the initial magma compositions remain distinct, though both have slightly shifted towards each other, see Figure 4.20. Fractionation, driven by crystal accumulation in the cumulate layer, changes major oxide trends.

The fractionation trend is evident in all major oxide plots. TiO_2, FeO, and MgO exhibit arced trends, with early fractionation depleting in these oxides relative to the recharge magma, followed by later crystal layers showing higher concentrations (Figure 4.20 A, C, D). In contrast, the remaining oxides (Al_2O_3, CaO, Na_2O, and K_2O) display linear trends. Figure 4.20 B, E, F and G. Al_2O_3 and CaO are enriched, while Na_2O and K_2O become depleted relative to the recharge magma Figure 4.20 B, E, F and G.

The mineral composition of the cumulate layer consists of 66.77 wt% feldspar, 11.13 wt% clinopyroxene, 10.35 wt% orthopyroxene, 3.78 wt% quartz, 6.42 wt% olivine, and 3.91 wt% spinel (see Appendix 7.3). Compared to the closed-system simulations, the cumulate layer in the open system contains higher concentrations of feldspar and lower quantities of quartz and SiO_2.

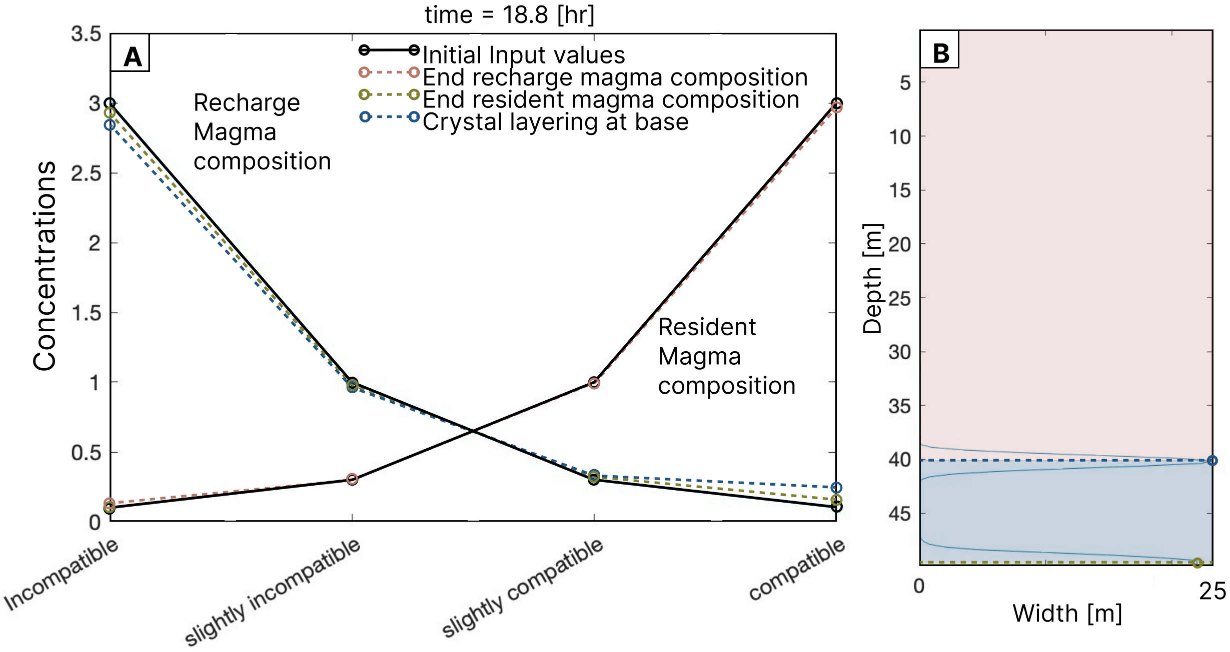

Figure 4.21: (A) Trace element spider diagram for the baseline open system reference simulation at the final time frame (18.8 hr). The x-axis shows trace elements arranged from incompatible to compatible, with respective partition coefficients of approximately 0.01, 0.1, 3, and 10. The y-axis shows dimensionless trace element concentrations. The black line represents the initial bulk system composition, which was set to contrasting trends between the resident and recharge magmas to highlight mixing behaviour. The pink, blue, and green lines represent different layers identified by density contrasts, corresponding to the regions shown in (B). (B) Model domain showing the spatial distribution of the compositional layers identified in (A). The axes represent depth and width within the model. Coloured circles and lines mark boundaries determined from density contrasts. Pink indicates the melt-rich resident magma layer at the top, blue represents the recharge magma layer that has not fully mixed, and green is the crystalline cumulate layer at the base.

The trace element signatures were initially designed with contrasting trends. The resident magma is enriched in compatible trace elements and depleted in incompatible trace elements (see Figure 4.21 A). In contrast, the recharge magma shows the opposite pattern, being enriched in incompatible elements and depleted in compatible ones. These contrasting compositions were assigned to the magmas to identify mixing trends between the two.

Throughout the simulation, the recharge signature experiences a slight depletion in the incompatible trace elements and a corresponding increase in the compatible trace elements.

The resident magma experiences the opposite trend. By the end of the simulation, both trace element signatures remain largely unaltered (see Figure 4.21).

The crystal layering at the system's base (Figure 4.21 B) displays a trace element composition closely resembling the initial recharge magma with some depletion in incompatible trace elements. There is also a slight increase in the compatible trace elements.

4.5.2 Geochemistry of the Open System Parameter Variations

Across the parameter tests, the models exhibit varying levels of deviation from the open reference simulation in terms of both internal dynamics and geochemistry. In the varied temperature parameter test, all models demonstrated consistent internal dynamic behaviour, including the formation of a hybridisation zone, crystal drips, multi-layered convection and cumulate layer formation. The geochemical signatures within this simulation mirror the trends outlined in the reference simulation.

There is minimal variation in geochemical trends across the varied recharge volume simulations. Figure 4.22 illustrates the major oxide values for the smallest (5 vol%) and largest (50 vol%) recharge volume simulations compared to the reference simulation. As seen from the Figure 4.22, both simulations exhibit the same major oxide trends as the reference simulation. The main variability is within the Ti_2O FeO and MgO concentrations, see Figure 4.22 A, C and D. The small recharge volume simulation (5 vol%) shows slightly higher concentrations of Ti_2O, FeO and MgO. Conversely, the larger recharge volume simulation (50 vol%) shows slightly lower Ti_2O, FeO and MgO concentrations. These differences correlate with slightly higher spinel and pyroxene values within the bottom layering. Overall, there is only minimal variation from the reference model, indicating that the recharge volume does not significantly influence the major oxide geochemical signatures within the first stages of chamber evolution.

The trace element data of the varied recharge simulations show similar outputs to the reference run. Figure 4.23 outlines the trace element signatures of the base melt layers within the smallest and highest recharge volume runs. These base layer signatures are similar to the input recharge compositions, indicating no extensive mixing between the two magmas. There are, however, slight variations of the most and least compatible trace elements which can be seen within Figure 4.23. In the 5 vol% recharge simulation, the least compatible trace element in the recharging magma decreases by 13.3% from its original concentration. In contrast, in the 50 vol% recharge simulation, it depletes by only 3.3%. (Figure 4.23 outlines the range of variations seen within the base crystal layering across the six simulations. This indicates that the recharge volume only slightly varies the initial chemical composition of the base layering.

The final parameter test, varying the H_2O contents, led to the biggest variations in the internal dynamics and the resulting geochemical signatures. The simulation with equal H_2O contents within both magmas sees the system enter a multi-layered convective regime; there is more vigorous mixing between the two end-member geochemical signatures. This mixing is reflected within the Harker diagrams depicted in Figure 4.24, which show straight line trends between the two initial compositions with minimal gaps between the two magmas.

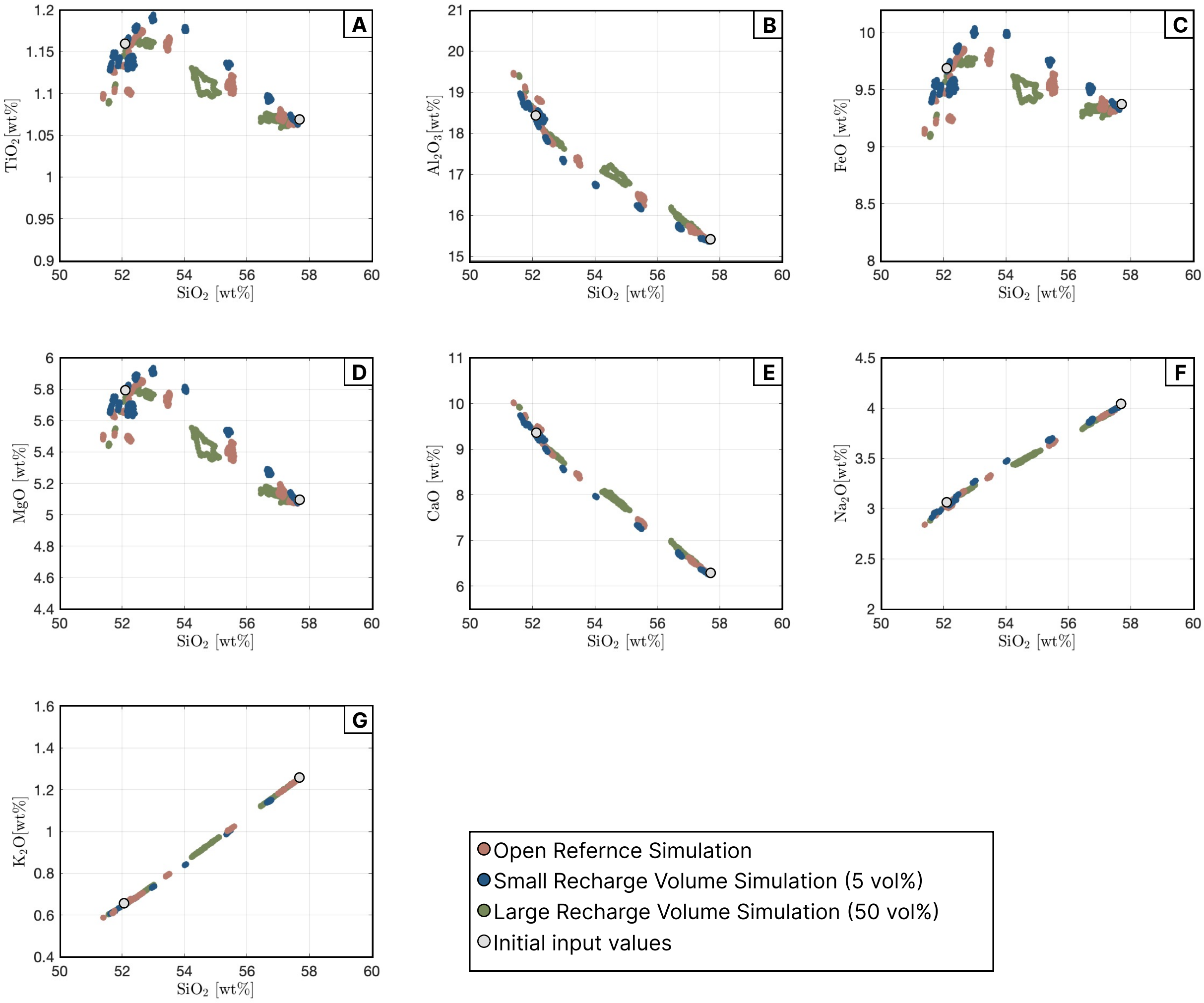

Figure 4.22: Harker plots of major oxide data from the largest (50 vol%) and smallest (5 vol%) volume recharge simulations compared to the baseline simulation. Data is taken from the final time frame of each model run. The reference simulation is plotted in pink, the small recharge volume simulation data is shown in blue, and the large recharge volume simulation is depicted in green. The initial input values of both magmas are plotted in grey circles to highlight the variation from the initial inputs. (A) TiO_2, (B) Al_2O_3, (C) FeO, (D) MgO, (E) CaO, (F) Na_2O, and (G) K_2O. Most Harker plots show straight-line trends, except for (A), (C), and (D), which exhibit arc trends. These oxides also display the greatest variation between the large and small recharge volume simulations. This indicates that changes in recharge volume lead to slight variations in TiO_2, FeO, and MgO.

The equal H_2O content simulation exhibits a fractionation trend similar to the reference simulation. The composition of the base cumulate layer at the end of the simulation contains lower Ti_2O, FeO, MgO, Na_2O and K_2O relative to the reference (Figure 4.24 A, C, D, F, G) and higher values of Al_2O_3 and CaO (Figure 4.24 B and E). This translates to more felspar formation and accumulation at the bottom of the model. This simulation displays a larger range of SiO_2 and major oxide values (See Figure 4.24).

The trace element composition of the equal H_2O simulation exhibits large variations from the reference model, illustrated in Figure 4.25 A). The cumulate layer displays a trace element

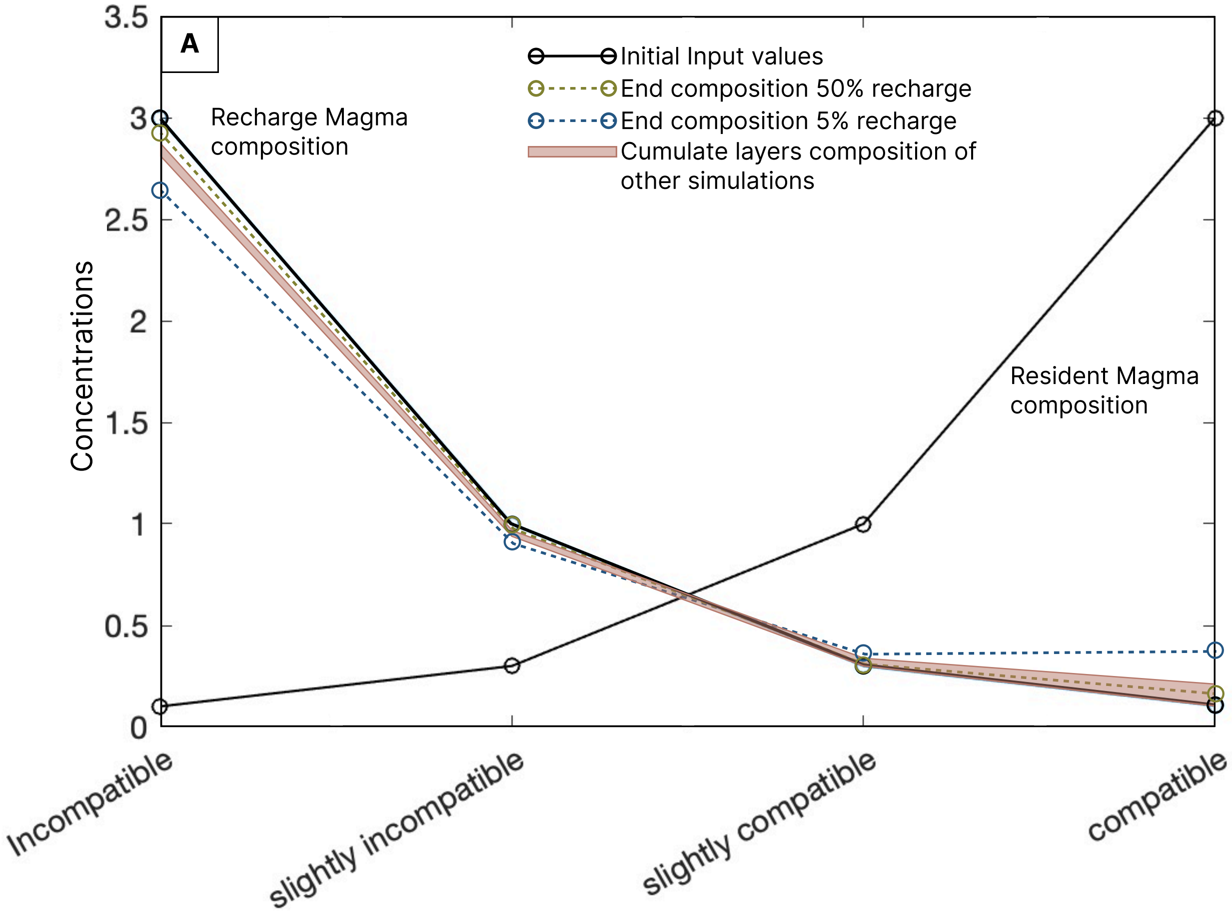

Figure 4.23: Plot of trace element compositions of the recharging magma for all varied recharge volume simulations. The black line represents the initial bulk system composition, which was set to contrasting trends between the resident and recharge magmas. The small recharge simulation composition is plotted in blue, and the large recharge simulation composition is plotted in green. The pink shaded area represents the range of compositions within the cumulate layers across all varied recharge simulations. The results indicate that the small recharge simulation exhibited slightly greater composition changes than the large recharge simulation. However, all simulations produced similar cumulate layer compositions, suggesting that recharge volume had little effect on composition during the early stages of mixing and fractional crystallisation.

composition that is more depleted in incompatible trace elements and enriched in the compatible trace elements compared to the reference simulation. Indicating greater interaction between the two end-member magma compositions, which is outlined in Figure 4.25 A.

The next simulation experiences H_2O rich recharge with 1 vol% more H_2O than the resident magma. This simulation experiences an overturn event within the first few minutes, which is captured within the major geochemical data as a straight-line mixing trend on the Harker plots. As the simulation progresses and crystals begin to form, a fractional crystallisation trend also forms, representing the base cumulate layer. The cumulate layer has similar SiO_2 values as the recharge magma, 52 wt%. It is more enriched in Al_2O_3, and CaO and depleted in Ti_2O, FeO, MgO, Na_2O and K_2O, as outlined in Figure 4.24. By the end of the simulation, the Ti_2O, FeO and MgO plots all show arced trends like the reference simulation, however, on a much

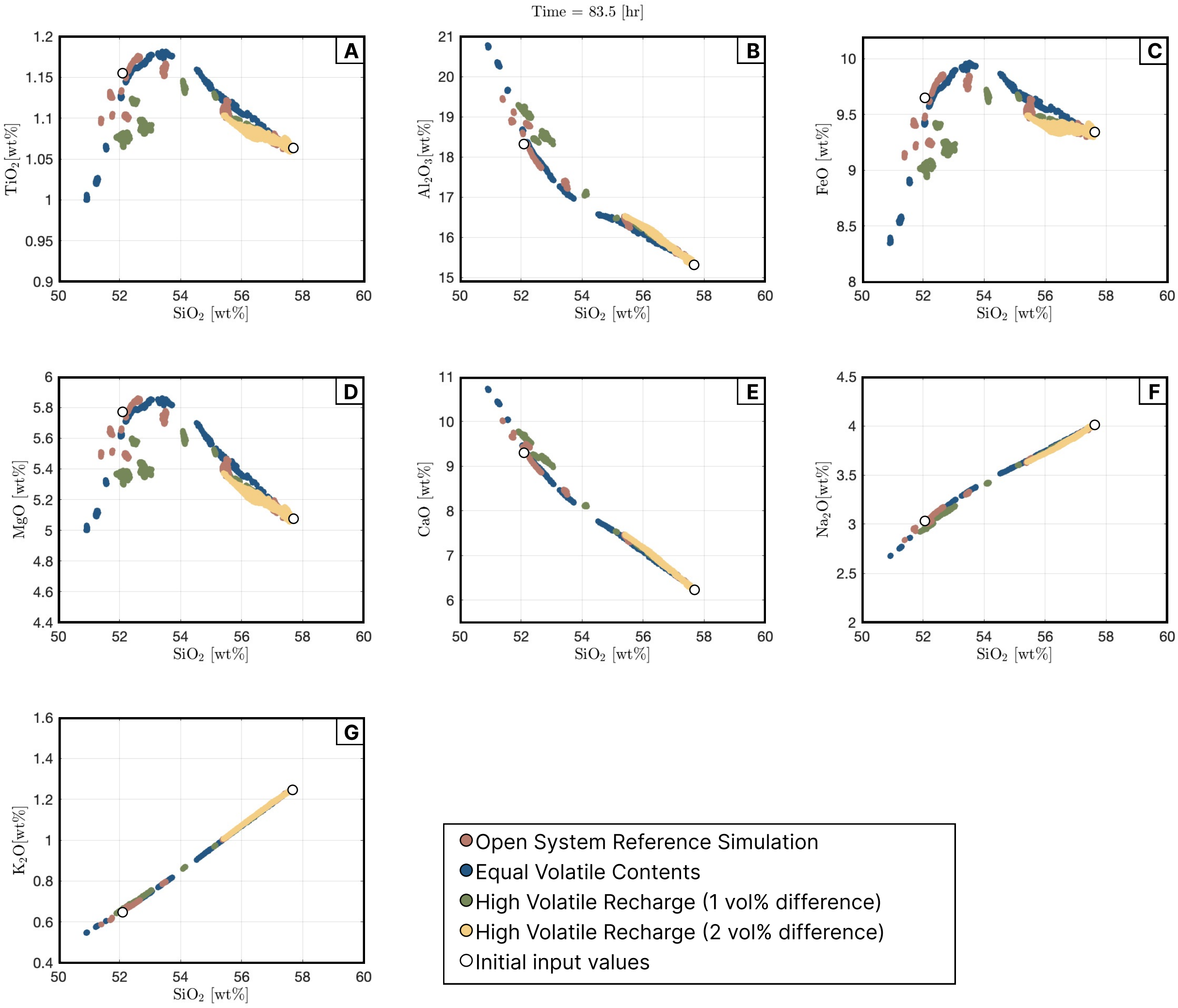

Figure 4.24: Major oxide data from the three varied H_2O content simulations compared to the open system reference simulation, taken at the final time frame of each model. The reference simulation data is plotted in pink. The equal H_2O content simulation data is shown in blue. The high H_2O recharge simulation with a 1 vol% difference is depicted in green, and the simulation with a 2 vol% difference is plotted in orange. Initial magma values are marked with white circles. (A) TiO_2, (B) Al_2O_3, (C) FeO, (D) MgO, (E) CaO, (F) Na_2O, and (G) K_2O. The results show that the varied H_2O content simulations all experienced greater levels of mixing between the two magma compositions than the other open simulations. In both the equal H_2O content model and the 1 vol% enriched recharge model, end-member compositions are still somewhat represented. However, in the 2 vol% difference recharge model, the compositions mix more thoroughly, evolving towards the composition of the larger-volume resident magma.

narrower SiO_2 range (see Figure 4.24 A, C and D).

The trace element values also show significant variations outlined in Figure 4.26. At the end of the simulation, the top layer of the system, which contains most of the melt-rich sections, has a trace element composition similar to the resident magma (see Figure 4.26 B). It shows a slight depletion of the compatible trace elements and a slight enrichment of the incompatible trace elements (Figure 4.26 A). The bottom layer of melt, which is less than 4 m thick, contains a composition almost completely between the two end members, indicating extensive mixing

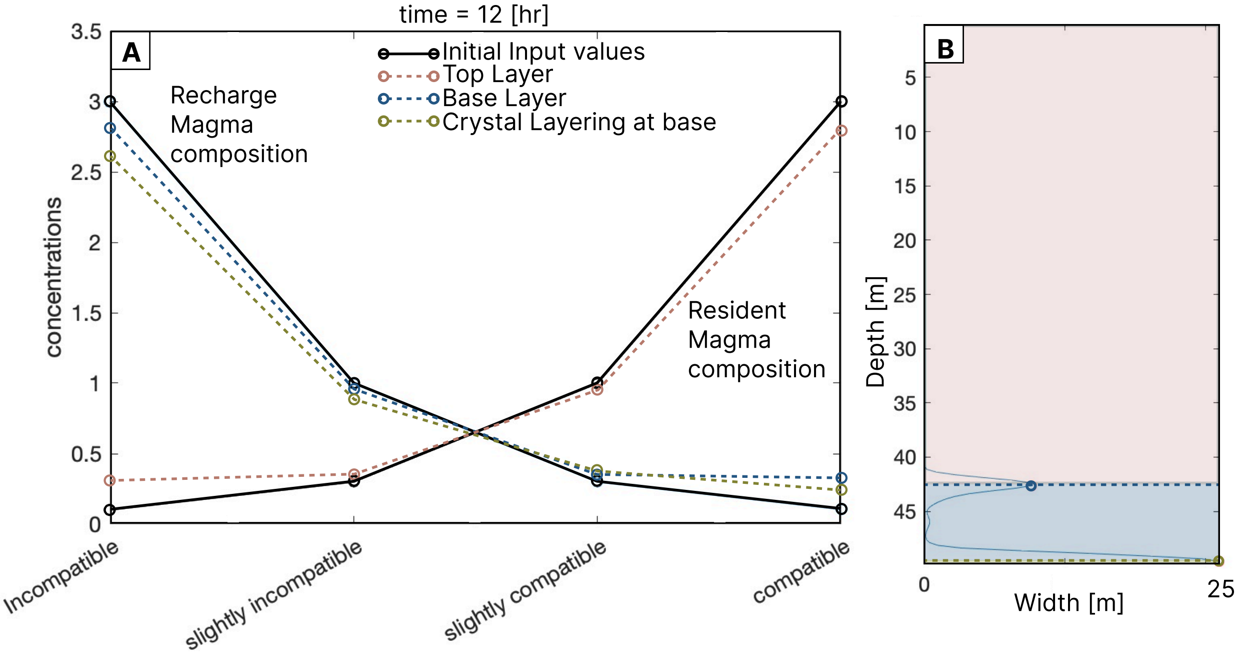

Figure 4.25: (A) Trace element spider diagram for the equal H_2O content simulation at the final time frame (12 hr). The x-axis shows trace elements arranged from incompatible to compatible (with partition coefficients of approximately 0.01, 0.1, 3, and 10, respectively), and the y-axis shows the dimensionless trace element concentrations. The initial input compositions are plotted in black and were set to contrasting trends between the resident and recharge magmas to highlight mixing behaviour. The pink, blue, and green lines represent the resident magma, recharge magma, and cumulate layer, respectively. The trace element plot indicates that increased mixing in this simulation leads to greater homogenisation of the two magmas. While the two melt-rich layers retain similarities to the initial resident and recharge magmas, the cumulate layer shows a composition similar to the recharging magma. (B) Shows the model domain with the spatial distribution of the different layers. The axes represent depth and width within the model. The coloured circles and lines mark the boundaries identified from the density fields, corresponding to the compositional layers plotted in (A). Pink indicates the resident, melt-rich top layer; blue represents the recharge magma layer; and green denotes the crystalline cumulate layer at the base.

between them. Finally the crystal-rich layer at the base which is less than a meter thick (Figure 4.26 B) contains a composition similar to that of the recharge magma, slightly depleted in incompatible trace elements and enriched in the compatible ones Figure 4.26 A.

The final simulation also sees a system recharged with H_2O rich magma, which has 2 wt% more H_2O than the resident magma. This simulation undergoes an overturn event, followed by density stratification, which results in little mixing or flow. The initial overturn event is visible within the major oxide data, see Figure 4.24. As the overturn event progresses, the overall system composition shifts towards the bulk resident magma composition, increasing in SiO_2. As it evolves it decreases in Ti_2O, FeO, MgO, Al_2O_3, and CaO and increases in Na_2O and K_2O (Figure 4.24). At 4.16 hr, the composition appears to pause and become static. From this point to the end of the simulation (45 hr), the composition does not change significantly. The cumulate at the base of the chamber contains a composition that matches the resident magma.

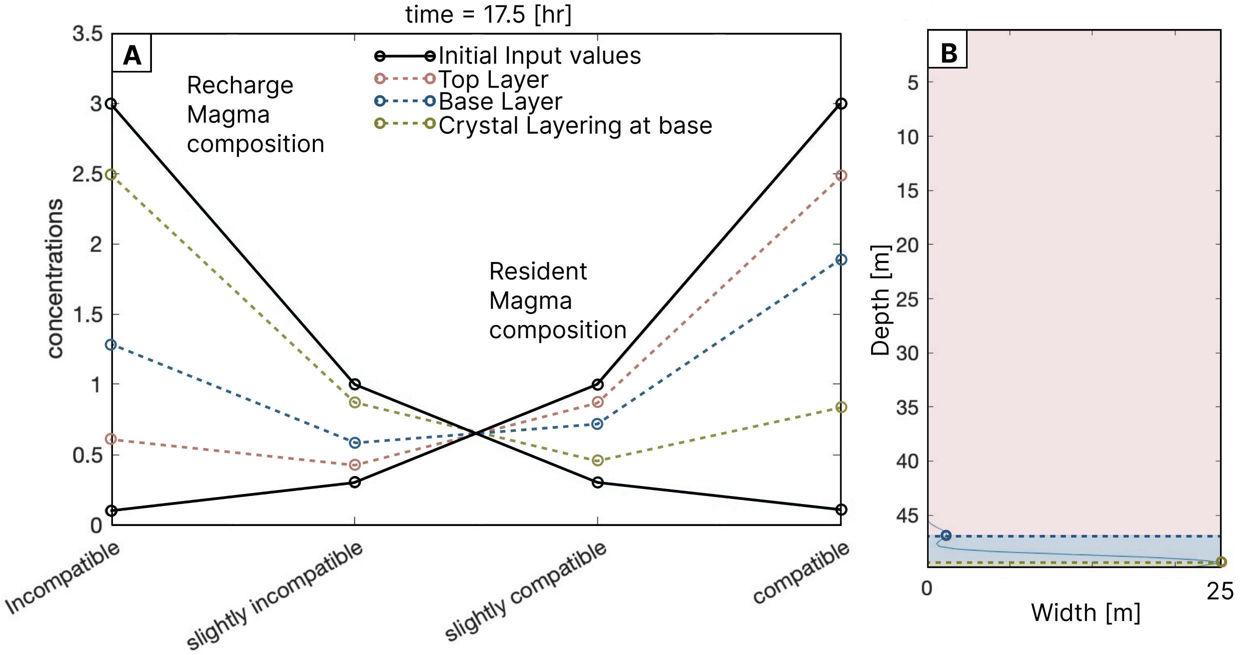

Figure 4.26: (A) Trace element spider diagram for the higher H_2O recharge simulation (1 vol % difference), taken at the final time frame (17.5 hr). The x-axis shows trace elements arranged from incompatible to compatible, and the y-axis shows the dimensionless trace element concentrations. The initial input compositions are plotted in black. Three distinct layers are identified within the system: the top layer (resident magma) in pink, the bottom layer (recharge magma) in blue, and the base cumulate layer in green. The trace element plot shows that increased mixing in this simulation leads to greater homogenisation of the two magmas. Both melt-rich layers exhibit significant variation across all four trace element values relative to the initial input compositions. The cumulate layer composition closely resembles that of the recharging magma. (B) Shows the locations and depths of these layers within the model domain. The axes represent depth and width within the model. The coloured circles and lines mark the boundaries identified from the density field, corresponding to the compositional layers plotted in (A).

At the top of the model is a convection cell containing the most well-mixed composition between the two end members. This can be seen within the trace element signatures in Figure 4.27 A-B. The interface layer that separates the convecting cell and the stably stratified base layer shows a trace element composition closer to the resident end member composition (Figure 4.27 A-B). Below the interface layer the bottom 25–28 m of the chamber are composed of the stably stratified layer which has a composition close to that of the resident magma (see Figure 4.27 A-B). Finaly at the base of this layer there is a crystal-rich layer that again has a composition that closely matches the initial resident magma composition, with only slight variations in concentration Figure 4.27 A.

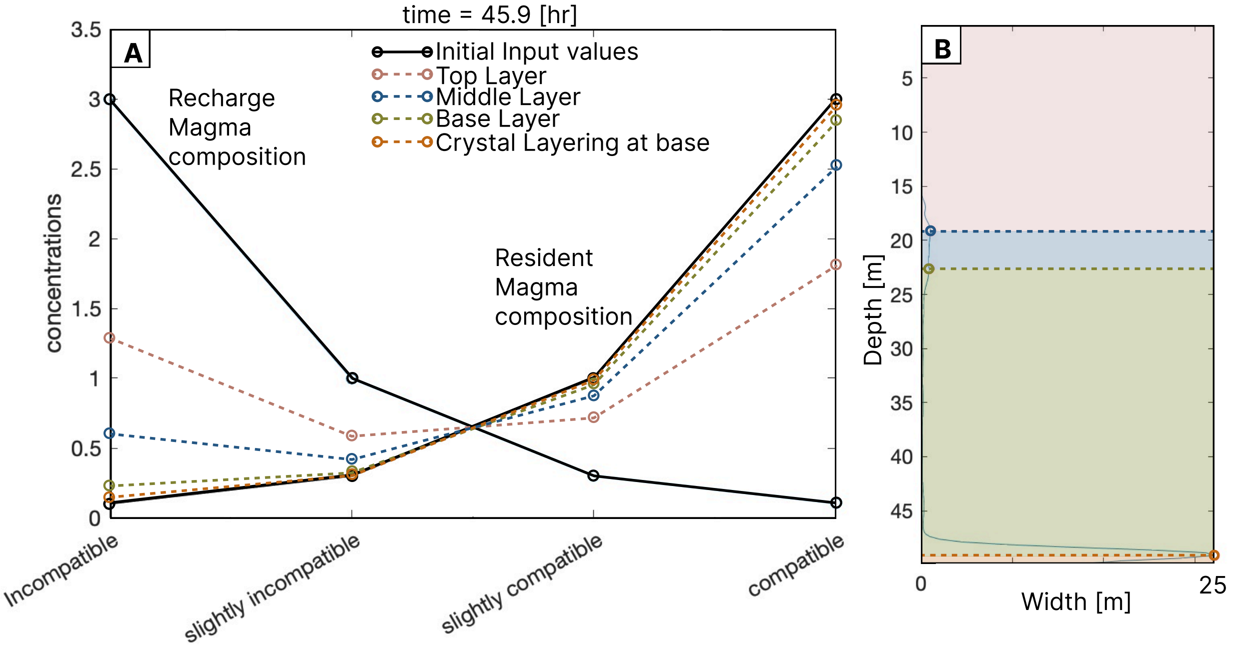

Figure 4.27: (A) Trace element spider diagram for the higher H_2O recharge simulation (2 vol% difference), taken at the final time frame (45.9 hr). The x-axis shows trace elements arranged from incompatible to compatible, and the y-axis shows the dimensionless trace element concentrations. The initial input compositions are plotted in black. Four distinct layers are identified within the system: the top layer containing the convection cell (pink), the interface layer directly below (blue), the large base layer (green), and the bottom crystal cumulate layer (orange). The trace element plot indicates that the overturn event in this simulation resulted in extensive mixing between the two magmas. All four layers exhibit variations across all trace elements, with compositions skewed closer to the resident magma. This suggests that the recharge magma's composition was lost during the overturn event. Unlike previous simulations, the base crystal layer closely matches the resident magma composition, implying that crystallisation occurred in situ from the resident magma after the overturn event, as it settled at the base. The most mixed composition is observed in the top layer. (B) Shows the locations and depths of these layers within the model domain. The axes represent depth and width within the model. The coloured circles and lines mark the boundaries identified from the density fields, corresponding to the compositional layers plotted in (A).

4.5.3 Isotope Ratios Within the Open System Simulations

To investigate mixing interactions between the resident and recharge magma, an isotope ratio was defined. The isotope ratio is designed to emulate delta (δ) notation and does not partition between phases making it a passive tracer of mixing. The two magmas were defined to have a contrasting isotope ratio. The resident magma had an isotope ratio of (-1), and the recharge magma was assigned a ratio of (+1).

The isotope ratio acts as a variable that allows for the tracking of hybridisation between the two magmas independent of crystal fractionation, it therefore allows for useful comparisons between different dynamic regimes. Figure 4.28 depicts the isotope field within the reference simulation, which experiences a hybridisation zone dynamic (Figure 4.28 A-D) and the high-water content recharge simulation, which experiences overturn (Figure 4.28 E-H). The Figure highlights that within the overturn simulation, there is greater homogenisation within the isotope field than in the reference simulation (Figure 4.28). The plots also indicate that within the hybridisation zone dynamic regime, there is only little mixing between the magmas (4.28 A-D). The lack of extensive mixing dynamics within the isotope fields suggests that the layering at the base of the system is a result of fractional crystallisation, rather than mixing. Within the high-water content recharge simulation (2 wt%) the overturn of the system is captured within the isotope fields see Figure 4.28 E-F, followed by mixing and hybridisation between the two magma compositions (Figure 4.28 G-H).

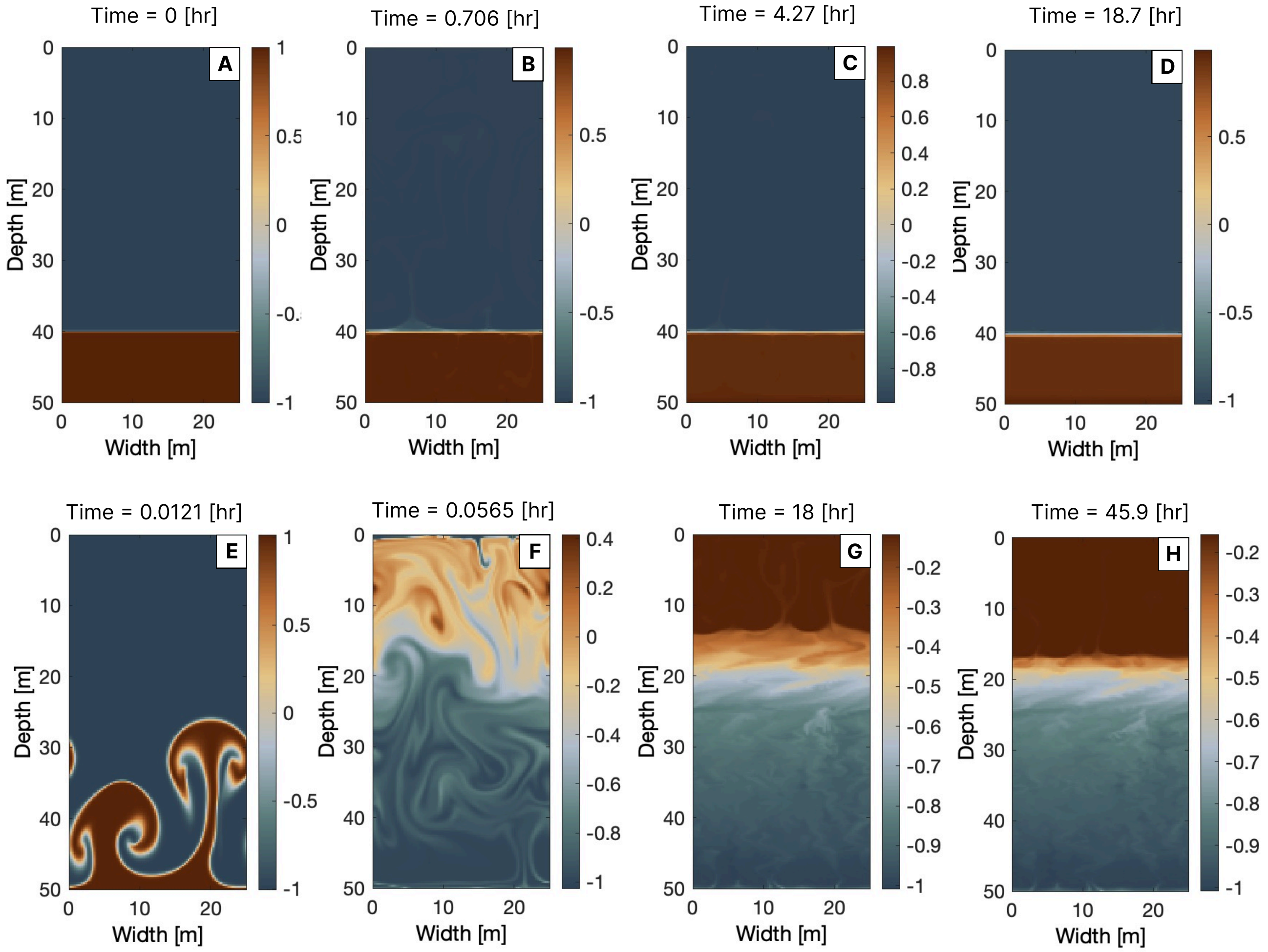

Figure 4.28: Stable Isotope fields of Isotope 1 at various time steps within two open systems simulations. Plots A-D show the isotope distributions from the reference simulation, progressing from the initial composition to the final time step at 18.7 hr. These plots highlight the two-layer set up of the system and show minor isotope variations where the two magmas meet. Plots E-H show evolving dynamics within the simulation that experiences high water content recharge into the system. With 2 wt% water difference between the two magmas. These plots also span four time steps, from the initial frame to the final time step at 45.9 hr. In contrast to the reference case these plots highlight the overturn and mixing of the isotope ratios.

Figure 4.29, shows the isotope values from the open system reference simulation plotted against SiO_2 to show how the isotope ratios evolve throughout the simulation (Figure 4.29 A-F). The plots show broken linear mixing trends with three identifiable clusters representing the resident magma, recharge magma, and the hybridization zone (Figure 4.29 C-F). The plots highlight that there is limited chemical interaction between the two magma compositions. Over time, the isotope values in the hybridisation zone evolve from values similar to the recharge magma toward those of the resident magma, which dominates the system volume this can be seen within Figure 4.29 C-F. The layering at the base of the system shows slight evolution in silica values however they retain an isotope ratio of -1 similar to the recharge magma composition. This indicates this portion of the initial geochemical signature is being preserved (Figure 4.29 A-F). A video of the isotope parameter field evolving throughout the run can also be seen within the supplemental data.

Throughout the varied recharge volume and temperature parameter tests, the simulations experience the same hybridisation zone dynamic regime and show the same isotope ratio behaviours to the open system reference case. However, within the varied water content parameter tests, slight changes in the recharge water content lead to varied internal dynamics, which in turn affect the extent of homogenisation between the two magmas. The isotope evolution throughout the varied water content simulations are presented as videos in the supplemental data.

The isotope ratio in the equal water content simulation shows a linear mixing trend that is less fragmented than the reference simulation (Figure 4.30 A-F). This less fragmented signature indicates greater mixing between the two magmas within this dynamic regime than in the previous homogenisation regime (Figure 4.29). Over time, slight gaps appear in the isotope compositions. These breaks are due to different convective layers forming throughout the simulation; the gaps are visible within Figure 4.30 D-F and can be seen clearly within the video in the supplemental data. Similar to the reference simulation, the crystal layering that forms at the system's base retains an isotope ratio of -1, like the initial recharge magma (Figure 4.30 A-F), again highlighting that this portion of the system is preserved and not involved in the mixing. By the end of the simulation there are three seperate convecting layers within the system outlined in Figure 4.30 G-H.

Within the simulation with a slightly higher water content in the recharge magma (1 wt%), the magmas mix more vigorously, and the system overturns within the first few minutes of the simulation run (Figure 4.17). This increased mixing is reflected in the isotope ratios, where consistent linear mixing trends form (Figure 4.31 A-F). The majority of the melt-rich section of the system reflects an isotope value similar to the resident magma, which has a higher volume of the system than the recharge magma Figure 4.31 G-H). However, the early forming crystal layers at the base have isotope values that reflect the recharge magma, as these layers formed quickly before the two magmas had extensively mixed (Figure 4.31 A-D). As the model progresses, the layers at the base form separate clusters within the isotope plots, and over time, these clusters become more isolated as the rest of the system continues to homogenise towards the resident magma composition (Figure 4.31 D-F). As subsequent layers form, they become progressively similar to the resident magma isotope ratio, highlighting different mixing stages (Figure 4.31 D-F). By the end of the simulation there is a narrow melt layer at the base of the

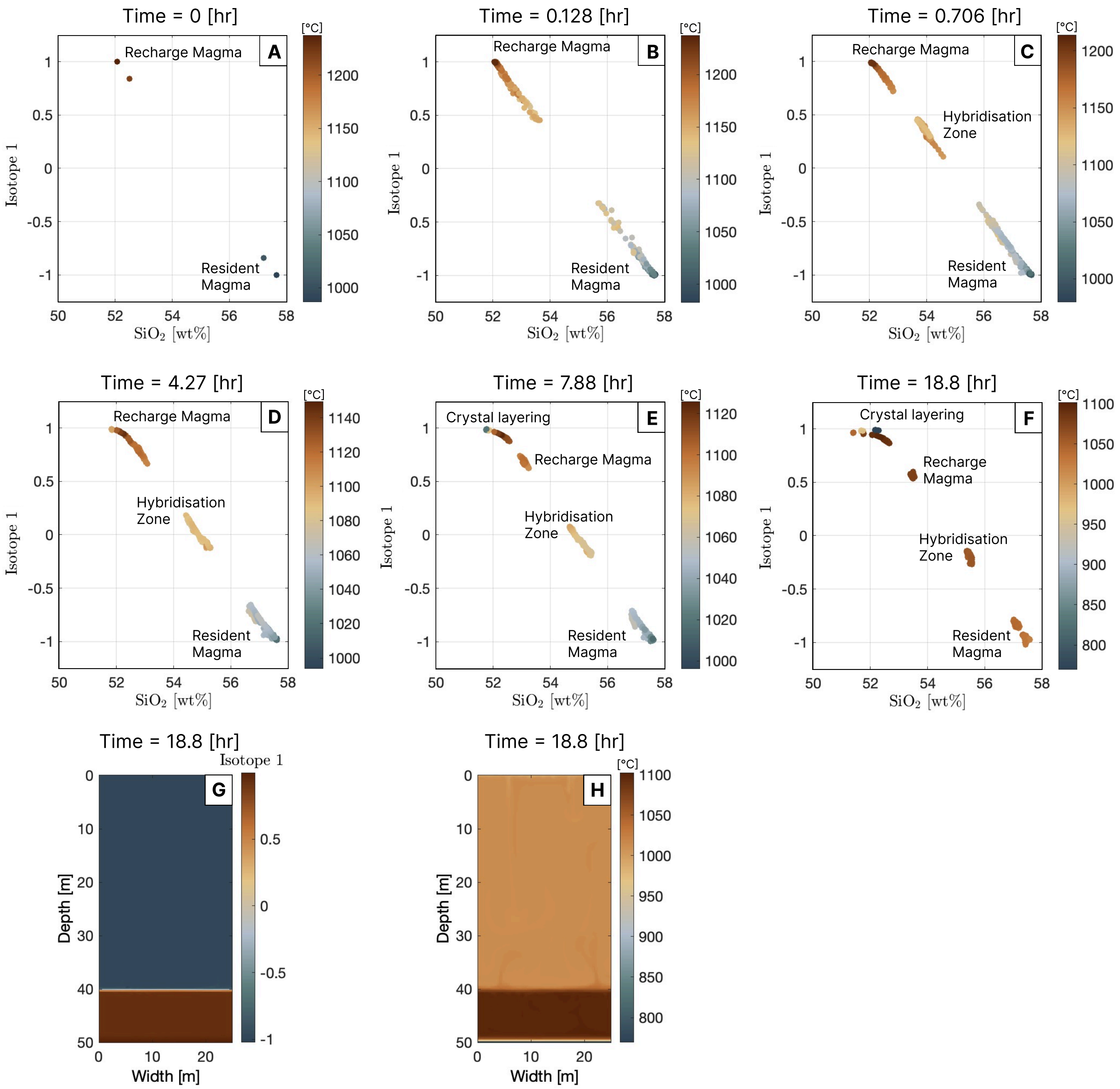

Figure 4.29: Isotope data from the open system reference simulation. Plots A–F show the isotope ratios plotted against SiO_2 at various time steps throughout the simulation, spanning from the initial to the final timestep. The data points are colour-mapped to the temperature field, highlighting their spatial distribution within the system. These plots illustrate the isotope ratio values of the initial magmas and the development of a hybridisation zone at their interface. G displays the isotope parameter field at the final time step, emphasising the presence of two distinct compositional layers. Plot H shows the corresponding temperature field used for the colour mapping in the isotope-SiO_2 plots.

system which can be seen in the isotope and temperature field Figure 4.31 G-H.

The final simulation that shows variations in the isotope ratio behaviour is the simulation with high water content in the recharge magma (2 wt%). Within this simulation, the system overturns due to density contrasts, and the two magmas almost completely homogenise (Figure 4.18). The extensive mixing of the magmas is visible in the isotope values (Figure 4.32 A-F). The isotope ratios show clear linear mixing trends that slowly move towards the initial resident

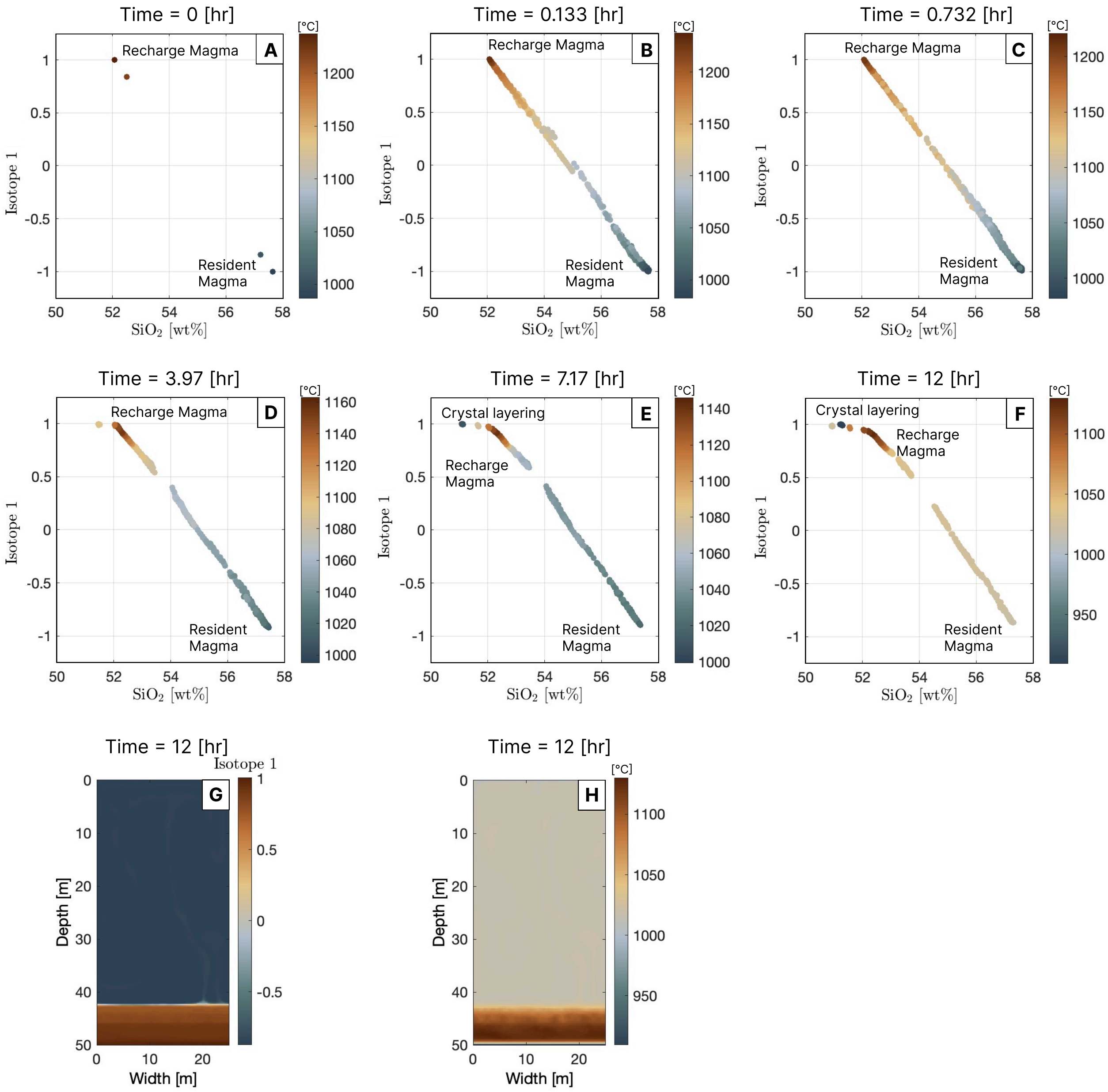

Figure 4.30: Isotope data from the equal water content simulation. Plots A–F show the isotope ratios plotted against SiO_2 at various timesteps throughout the simulation, spanning from the initial to the final timestep. The data points are colour-mapped to the temperature field, highlighting their spatial distribution within the system. The plots show linear mixing trends between the two magmas, with slight breaks appearing related to transient convective layers forming. Plot G displays the isotope parameter field at the final time step, which shows three convective layers. plot H shows the corresponding temperature field used for the colour mapping in the isotope-SiO_2 plots.

magma value as the magmas mix, as seen in Figure 4.32 B-F. The system overturn results in the layering at the base reflecting isotope ratios close to the initial resident magma value (Figure 4.32 A-F). The isotope ratio fields show that the recharge magma is thoroughly mixed and lost within the system (Figure 4.32 A-F). By the end of the simulation there is only slight variation within the isotope ratio field, (Figure 4.32 G).

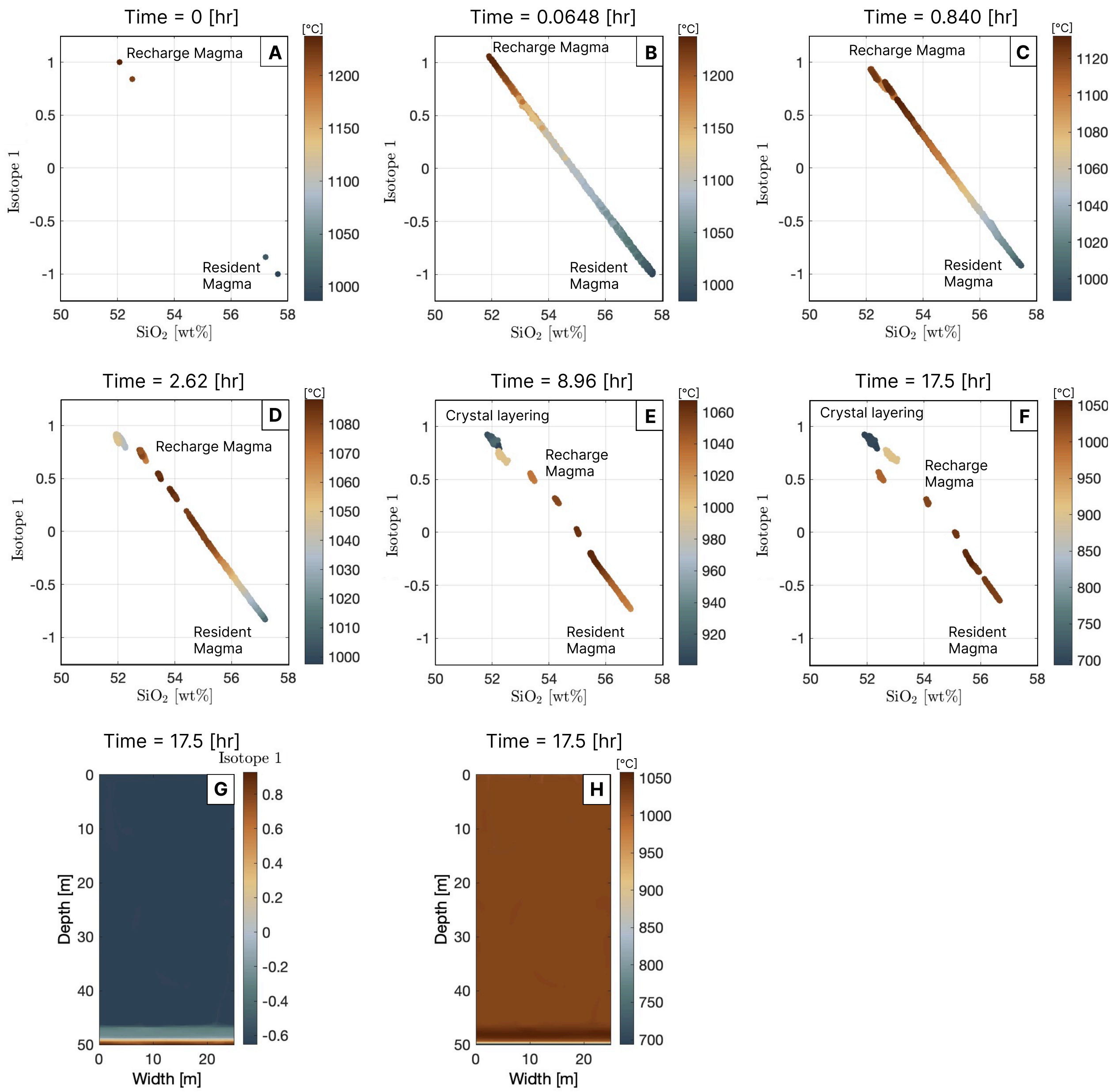

Figure 4.31: Isotope data from the simulation with 1 wt% water difference between the two magmas. Plots A–F show the isotope ratios plotted against SiO_2 at various timesteps throughout the simulation, from the initial to the final timestep. The data points are colour-mapped to the temperature field, highlighting their spatial distribution within the system. The plots show linear mixing trends between the two magmas. Additionally the base layers have isotope ratios reflecting different degrees of mixing. Panel G displays the isotope parameter field at the final time step, which shows a narrow layer remaining at the base of the system. Panel H shows the corresponding temperature field used for the colour mapping in the isotope-SiO_2 plots.

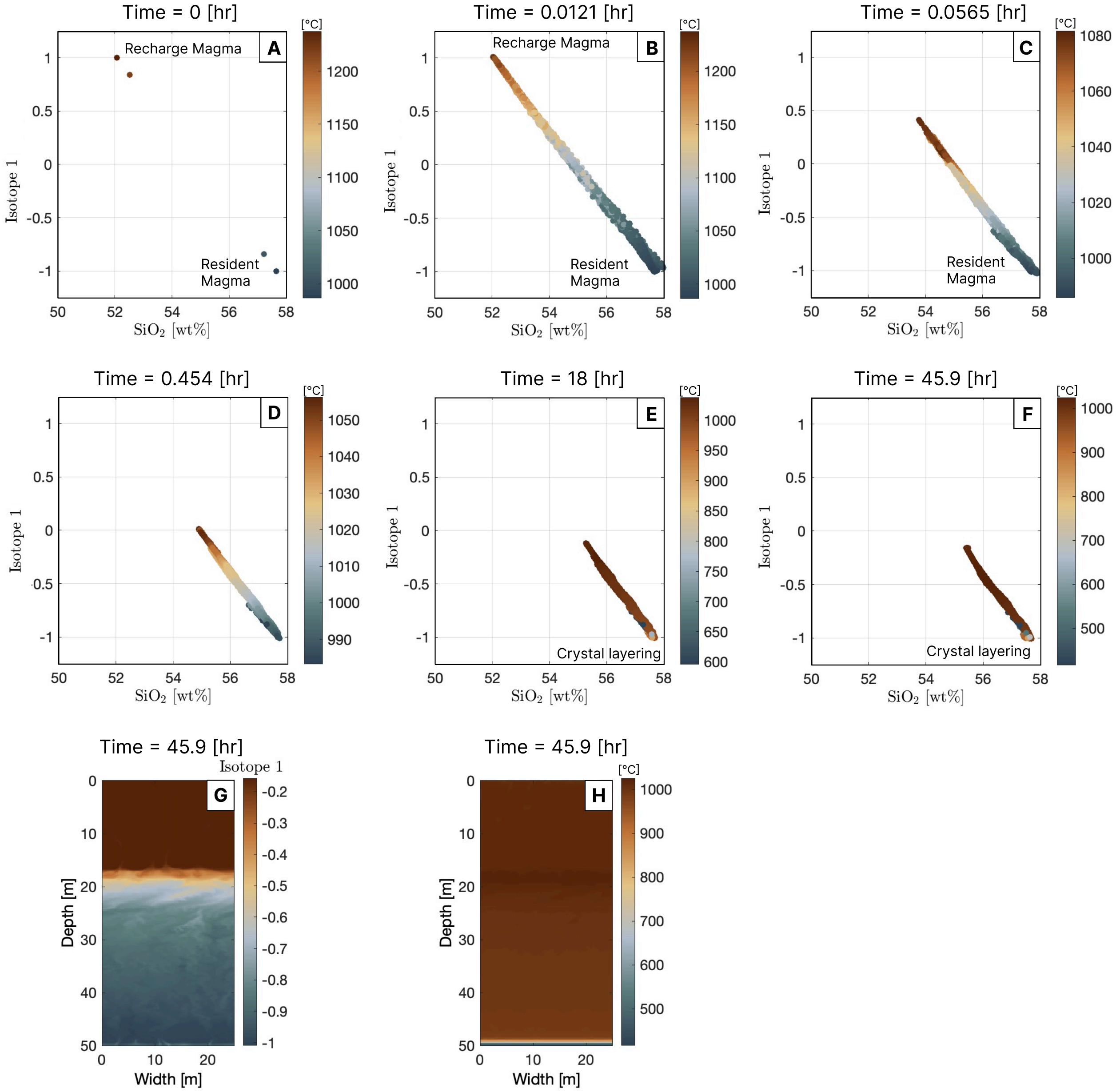

Figure 4.32: Isotope data from the simulation with 2 wt% water difference between the two magmas. Plots A–F show the isotope ratios plotted against SiO_2 at various timesteps throughout the simulation, from the initial to the final timestep. The data points are colour-mapped to the temperature field, highlighting their spatial distribution within the system. The plots show linear mixing trends between the two magmas. As the system homogenises the recharge magma composition is lost, and the linear trends move towards the resident magma. G displays the isotope parameter field at the final time step, which shows a slight variation between two layers. Plot H shows the corresponding temperature field used for the colour mapping in the isotope-SiO_2 plots.

4.6 Machine Learning

One of the primary objectives of this research is to explore the feasibility of reconstructing the original compositions of magma end members from the end model geochemical data. To test this, a machine learning script employing principal component analysis (PCA) and factor analysis was utilised on ten of the open system simulations. The five varied temperature simulations were excluded because they showed no significantly different dynamics. All the varied recharge models and varied H_2O models were included to capture the varied dynamic regimes identified.

The machine learning analysis was performed multiple times, varying both the types of data included (major oxides, trace elements, and stable isotopes) and the number of data points sampled. Within the framework of the model two isotope systems were defined. To track mixing, only one isotope ratio was required; therefore, the two isotopes were defined as having opposite values to each other, and both show identical patterns but in reverse. Both isotope systems were included within the machine learning analysis; however, as they are correlated, the principle component analysis, which reduces the data dimensions, simplified them down to one data direction. Therefore, the second isotope ratio does not affect the results. The isotope ratios were included in the machine learning dataset in an effort to improve model performance and better backtrack to the original endmember compositions. Sampling strategies ranged from using all data points within the system to selecting 25 random samples across the domain. Random sampling was intended to mimic the process of collecting real-world samples from a rock exposure, where the number of samples typically depends on the exposure's size, time and cost constraints.

4.6.1 All Data Points

The initial run of the machine learning includes major oxides, trace elements, and stable isotope data from each point within the 2D model domain. After running the simulations for one month, the final output frame from each run is used to analyse the results. However, the time represented by this final output frame varies across simulations due to differences in the complexity of the dynamics each simulation experiences. These model times range from 7.6 hr to 45.9 hr.

Once the machine learning script produces the end member predictions, error norms are calculated to evaluate how well the predictions match the initial end member compositions. This assessment is crucial for determining the accuracy of the machine learning model. The error norms measure the difference between the predicted compositions and the actual initial end member inputs.

Figure 4.33 presents the predicted end member values for the open system reference simulation. The data is displayed on Harker plots, and is compared against the initial end member compositions and the end frame geochemistry. The predicted end members are compared to the final geochemistry spread of the model to examine how well the reduced data captures the full

Model ID	Recharge End Member Error	Resident End Member Error	Overall Error	# No of End Member predictions
Open_Reference	0.0054	0.0014	0.0038	2
Smallest_Rech_volume_5	0.0036	0.0012	0.0026	2
Small_Rech_volume_15	0.006	0.0009	0.0042	2
Small_Rech_volume_10	0.006	0.0009	0.0042	2
Large_Rech_volume_30	0.0046	0.0022	0.0035	2
Large_Rech_volume_40	0.0036	0.0026	0.0031	2
Largest_Rech_volume_50	0.0029	0.0029	0.0029	2
Equal_Water	0.0361	0.0030	0.0248	3
High_Water_Rech_1	0.0326	0.0221	0.0275	3
Higher_Water_Rech_2	0.0881	0.014	0.0611	3

Table 4.5: Whole system analysis error norm values predicted end members and overall model output.

range of geochemical trends, such as mixing and fractionation trends. The initial geochemical signatures are plotted to evaluate the accuracy of the machine learning predictions by assessing how well they match the initial compositions.

The predicted end members are a good match for the initial values; however, the reduced data points do not capture the full geochemical trends of the simulation end signature. This is particularly prominent within the Ti_2O, FeO and MgO Harker plots (See Figure 4.33). This indicates that the reduced data isolates the mixing trend by losing the additional variability introduced by fractional crystallisation.

When prompted for three end member predictions, the reduced data is able to capture the end geochemical data and provides two end members which match the input values. The predicted end members have significantly higher errors than when asked for two end member compositions, 0.0209 for the resident end member, and 0.0205 for the recharge end member. The trend that the third end member captures is the fractional crystallisation trend (Figure 4.34)

The six varied recharge volume simulations were run through the machine learning model. The machine learning successfully predicts two matching end members for all six simulations, all of which experience hybridisation zone dynamics. All six display error norms less than 0.004, indicating that they match the initial inputs well (see Table 4.5). As the recharge volume increases, the error norm for the resident magma end member increases from 0.0012 to 0.0029.

The remaining three varied H_2O content models all experience significant degrees of mixing between the two initial magmas, which proves more difficult to predict the initial end members. Two end member predictions are insufficient to identify the initial inputs and three end members produce high errors.

Within the equal H_2O content simulation, the resident magma composition remains traceable with a low error of 0.003, but the machine learning script is less successful in identifying the recharge magma composition.

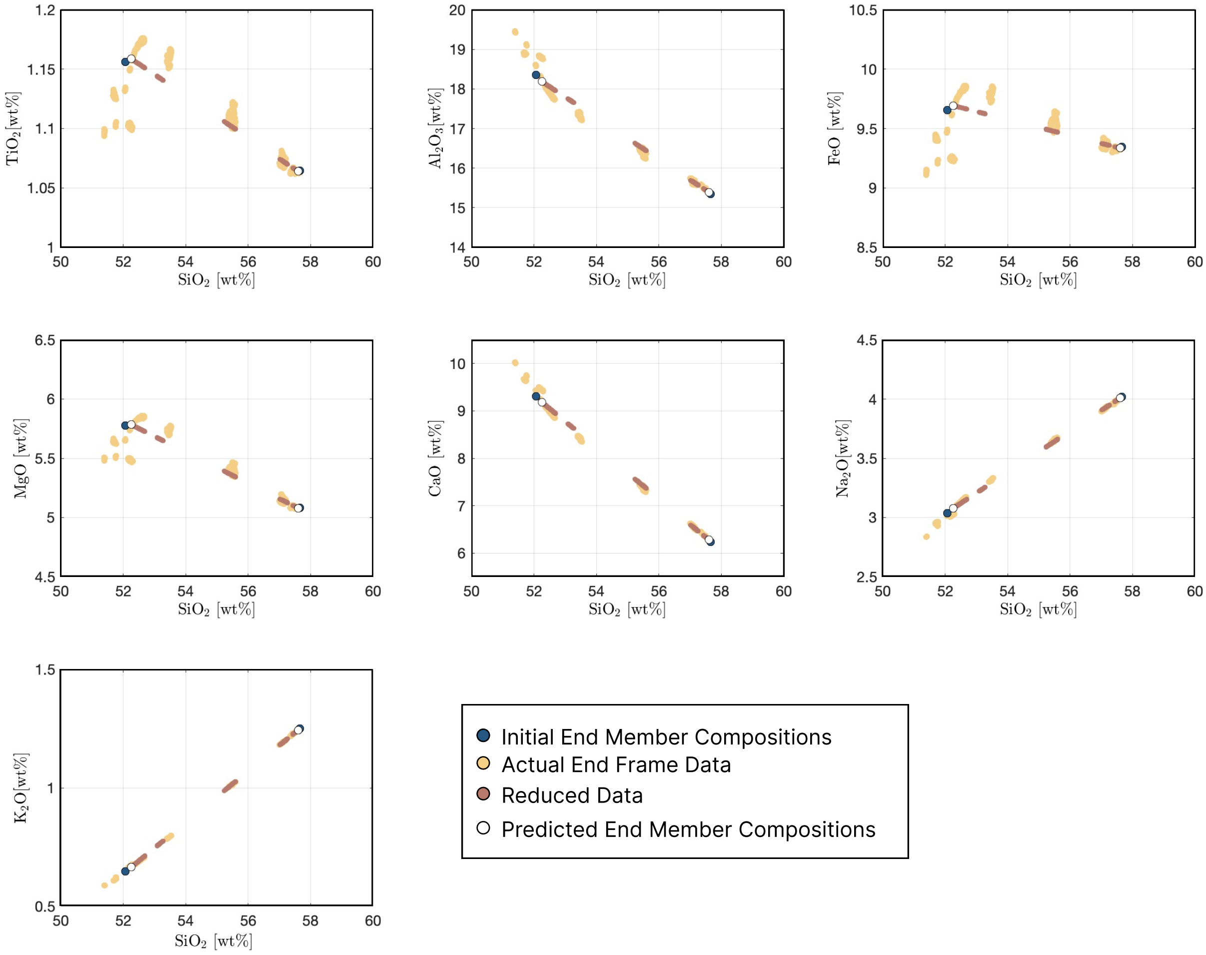

Figure 4.33: This figure depicts Harker plots of the predicted major oxide endmembers from the machine learning analysis of the open system reference simulation. The data was generated when the machine learning script was prompted to identify two endmember compositions. The analysis incorporated all available data points from the system. Blue points represent the initial input compositions, while white points indicate the predicted endmembers identified by the script. Yellow clusters display the original simulation output, and pink clusters represent the reduced dataset processed by the machine learning model. The results show that the script successfully predicted two matching endmember compositions and effectively filtered out the fractional crystallisation trend.

In the first H_2O rich recharge simulation (1 vol% difference), end member prediction is again impossible. The overall composition of the system evolves away from the initial values. Similar to the previous simulation, the machine learning produces one matching end member composition close to the initial resident magma. When prompted for three end members, the remaining two are closer to the recharge magma composition; however, neither fits the initial value well.

In the final simulation, which undergoes whole-system convection and stable stratification, the resident magma can still be identified, but the recharge magma's geochemical signature is not detected. This is shown in the figure of the three-endmember reconstruction, where increased mixing creates a bias towards the resident magma (See Figure 4.35). The endmem-

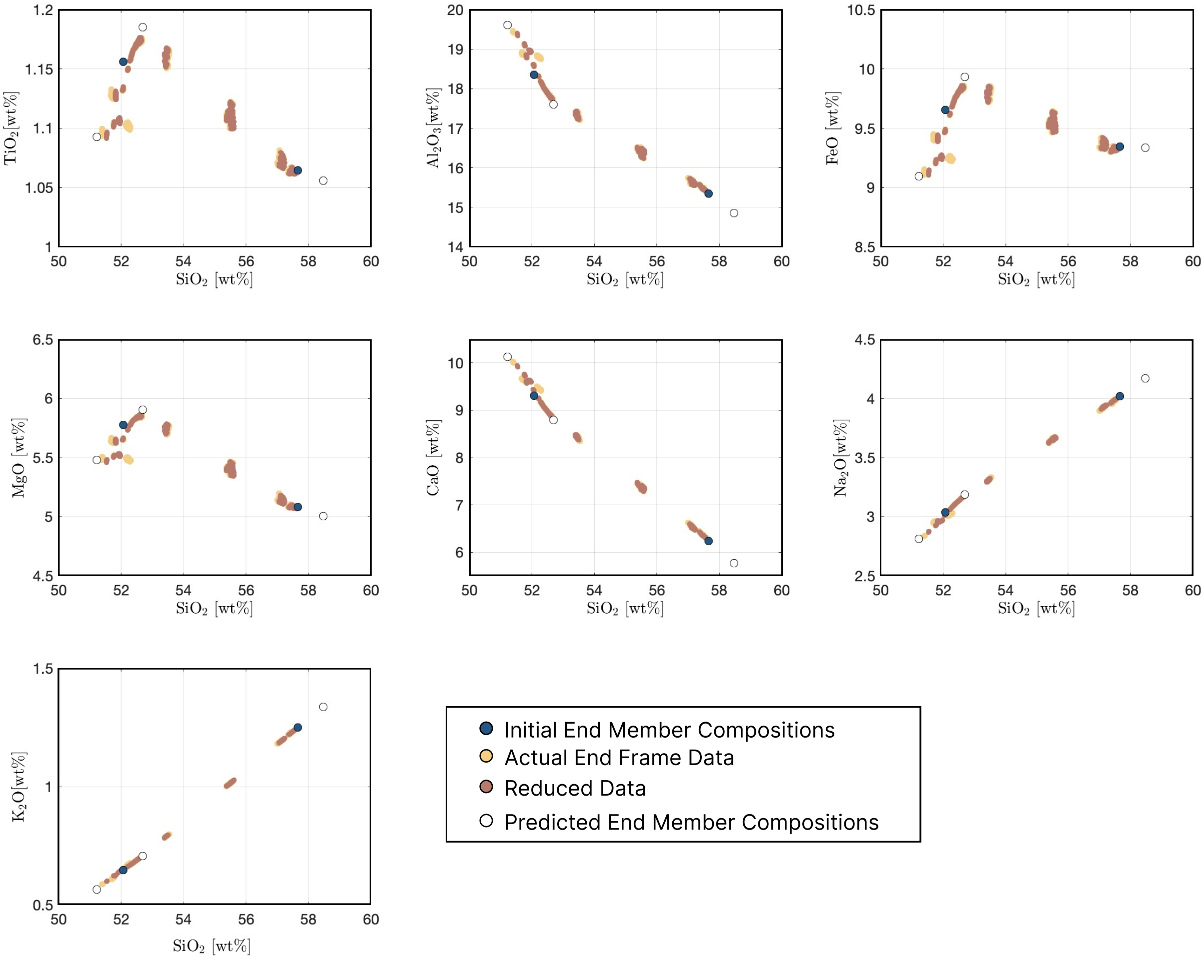

Figure 4.34: This figure depicts Harker plots of the predicted major oxide endmembers from the machine learning analysis of the open system reference simulation. The data was generated when the machine learning script was tasked with identifying three endmember compositions. The analysis used all available data points from the system. Blue points represent the initial input compositions, while white points indicate the predicted endmembers identified by the script. Yellow clusters show the original simulation output, and pink clusters represent the reduced dataset processed by the machine learning model. The results demonstrate that the script successfully predicted two matching endmember compositions, although with higher errors than the two endmember analyses. The third endmember captures the fractional crystallisation trend.

ber reconstruction struggles to identify the recharge magma composition because it makes up a smaller portion of the system. As mixing intensifies, the recharge signature becomes less distinct, making it increasingly difficult to resolve in the geochemical analysis.

4.6.2 Varied Geochemical Data

This analysis considers which data types (major and trace elements and stable isotopes) should be included to best predict end members. In the field, a full scope of data collection is not always possible due to time and funding constraints. All ten models are run through the machine learning script, first excluding both trace elements and stable isotopes and then excluding only

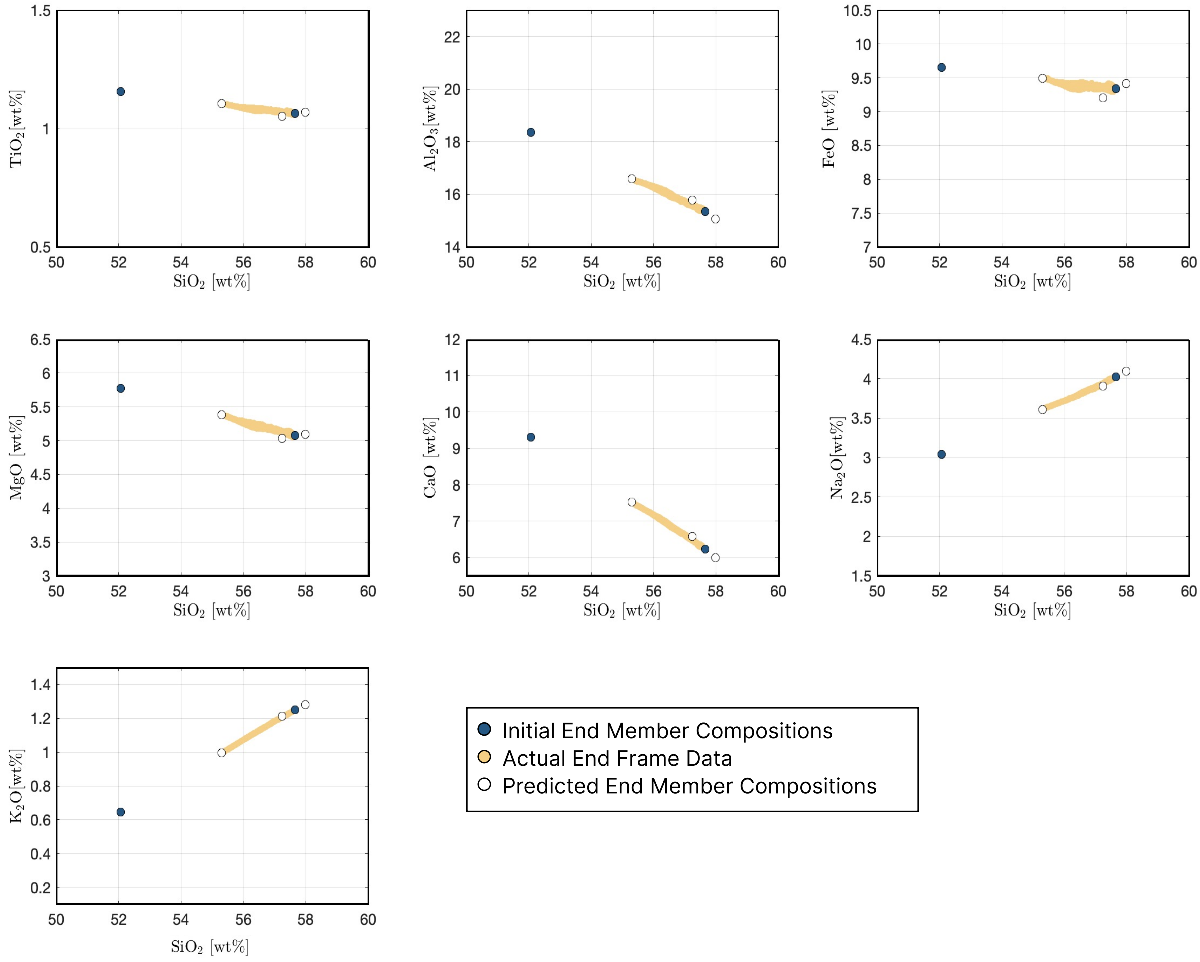

Figure 4.35: This figure depicts Harker plots of the predicted major oxide endmembers from the machine learning analysis of the H_2O rich recharge simulation (2%) simulation. The data was generated when the machine learning script was tasked with identifying three endmember compositions. The analysis used all available data points from the system. Blue points represent the initial input compositions, while white points indicate the predicted endmembers identified by the script. Yellow clusters show the original simulation output. The results demonstrate that the script unsuccessfully predicted two matching endmember compositions. It can identify two end members close to the resident magma composition within all of the oxide Harker plots; however, it fails to identify the recharging magma composition, with the predicted end member (white) being far away from the initial values (blue)

the stable isotopes. The calculated error norms for these variations are outlined in Appendix 7.4. The results show trends similar to those in the previous example, which includes all the data. Two predicted end members are sufficient to identify the initial geochemical signatures for all seven hybridisation zone simulations. The lowest error values are produced when only the major oxide data is analysed, followed by the inclusion of the trace elements and finally the analysis of all three.

Additionally, there is greater success in predicting the end members of the equal H_2O simulation when the stable isotopes are excluded. Finding end members for the overturn simulations still proves difficult, and although the errors are reduced relative to the whole data analysis, they remain relatively high (Appendix 7.4). Stable isotopes often show smaller variations than major and trace elements. Therefore, the lower variability may not provide enough discriminative power to distinguish between the different end members.

4.6.3 Varied Data Points

The final analysis involves varying the number of data points included in the machine learning model to simulate the constrains often encountered in fieldwork. Due to the extensive size of geological bodies, geologists cannot sample every point in a natural system. In real-world scenarios, the number of samples collected is often constrained by factors such as the availability of exposed rock, time limitations, and processing costs. For example, a small geological body might only be analysed a few times if there is significant petrological variation, whereas a larger pluton, covering an area of 100 km^2 or more, might be sampled more extensively. To reflect these field limitations, the machine learning analysis was conducted with 25 and 50 random samples taken from across the domain area (See Figure 4.36). Although this represents a relatively large sample size compared to typical field studies, it aims to simulate the practical challenges of sampling density, variability, and the trade-offs between data quantity and precision.

Over the past seven decades, many studies have utilised whole rock data to identify trends associated with geological processes such as fractional crystallisation, mixing, and assimilation [Thomas and Sinha, 1999, Vogel et al., 2008]. While detailed mineral-scale studies provide more precise constraints on these processes [Davidson et al., 2008, Oeser et al., 2015], they are both expensive and time-consuming. Conversely, techniques like portable XRF and remote sensing can increase the number of whole rock data points but come with a trade-off in precision [Balaram, 2017, Vonopartis et al., 2022].

By analysing these reduced datasets, we can evaluate how well the model performs under conditions similar to those encountered in actual geological studies. The reduced data sets lead to greater errors for the reference simulation and the varied recharge simulations. Despite the higher errors, matching end member compositions can still be identified from both 50 and 25 random samples. The end member predictions for the 25 random samples produce lower errors than those predicted for 50 samples. The error norm values are outlined in Appendix 7.4.

The reduced data point analysis is unsuccessful in predicting end members for the three varied H_2O content simulations. It produces error norm values similar to those of the whole system analysis.

Finally, the machine learning analysis is carried out one more time, taking samples from the top and base layers of the system. In the field, it is sometimes possible to identify cumulate layering and the roofs of the systems. The top and base sections of the model domain are identified, taking 20 rows of each, and 25 samples are randomly taken from these rows (See Figure 4.36). Two end members are successfully predicted for the hybridisation zone simulations with considerably low errors. All three varied H_2O simulations produce high errors, and only one end member can be predicted with any accuracy (See Appendix 7.4).

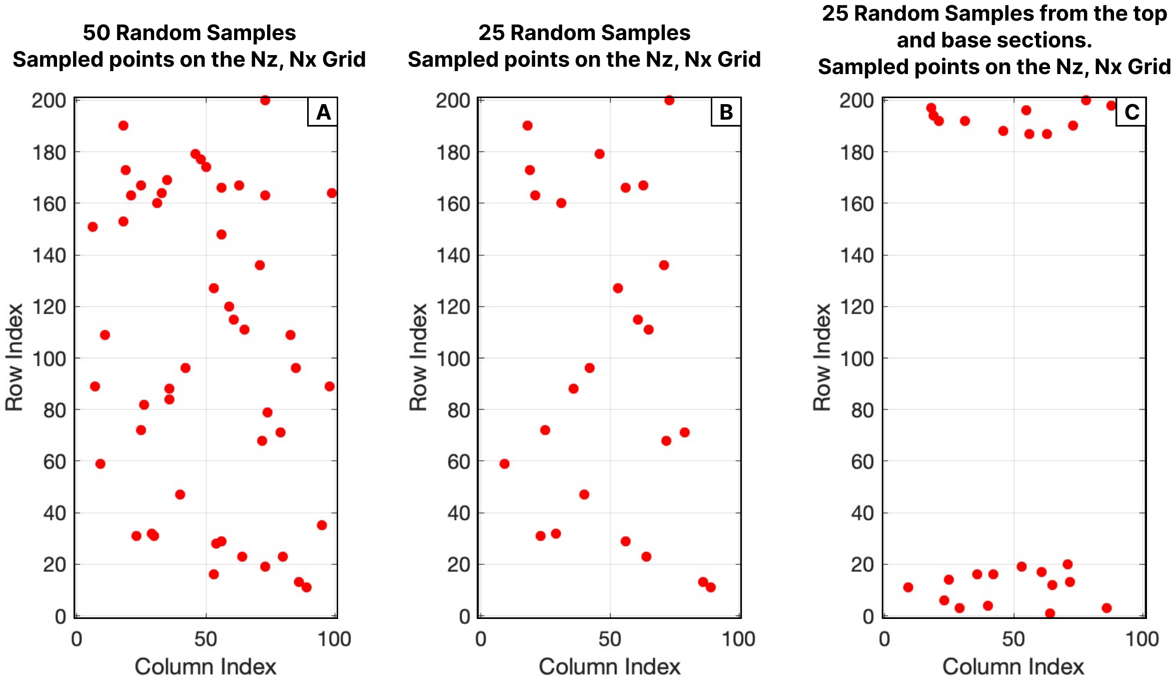

Figure 4.36: A) Depicts the locations of the random samples taken within the 50 random sample machine learning analysis. B) represents the locations of the samples taken for the 25 random sample analysis. C) represents the locations within the top and bottom margins of the systems where 25 random samples were taken from the system peripheries.

Overall, machine learning is somewhat successful at predicting end members if the system has not undergone significant mixing. However, even a short 1-2 hr overturn event is sufficient at overwriting the geochemical signatures within the system, making backtracking to both end members difficult. The major oxide data proves to be the best for predicting end member compositions. However, trace elements also prove to be good tracers when looking at the more complex overturn simulations. Finally, reduced data points result in increased errors; however, the data suggests that samples collected from the margins of systems may retain traces of the initial endmember signatures.

Chapter 5

Discussion

Across the ten closed system simulations, they all exhibit classic examples of expected dynamics for a melt-rich magma body, including whole system convection, fractional crystallisation, cumulate layer formation, and plumes and drips. The results align with established conceptual models of the dynamics within simple magma chambers [Bowen, 1928, Sparks et al., 1985, Campbell, 1996, Marsh, 2013]. They also align with the interpretation of field data and previous numerical modelling studies [Sparks and Marshall, 1986, Marsh, 1996, Gutiérrez and Parada, 2010, Dufek and Bachmann, 2010]. The observed whole-system convection across all ten simulations underscores the critical role of density contrast in driving flow dynamics [Sparks and Huppert, 1984]. Specifically, the results from the varied cooling rate simulations reveal how different cooling rates influence convective behaviour. The faster wall-rock cooling rate results in more rapid crystallisation at the wall-rock contacts (see Figure 4.2), leading to a larger density contrast between the dense crystal drips and the hotter inner magma. The denser crystal drips in the fast cooling systems drives faster convection, with average speeds of 99 m/hr compared to 22 m/hr in the slower cooling system. The variations in crystal size, however, do not significantly affect convective speeds, suggesting that a density contrast rather than crystal size is a greater driver of convection. Additionally, the convective speeds increase with chamber size, following a squared relationship between length scales and convective speeds as described by Stokes' law (See Equation 3.8). Specifically, the largest chamber size exhibits an average convective speed of 75 m/hr, approximately four times faster than the smallest chamber size, which averages 17 m/hr. This finding highlights the significant impact of chamber size on convection rates. Throughout all ten closed-system simulations, whole-system convection persists for the entire duration of the simulation, this convective regime can be see within Figure 4.1, matching the dynamics observed in similar studies such as those by [Gutiérrez and Parada, 2010].

5.1 Significance of Water Content Within Closed Systems

This study found that the water content exerted the most significant control on shallow magma body dynamics and geochemical signatures among the parameters explored (Figure 4.6).

Previous studies found that volatiles, particularly water, play an important role in controlling the crystallisation temperature of magma [Phemister, 1934, Wallace et al., 2015, Edmonds and Woods, 2018]. Lower water contents raise the crystallisation temperature, meaning that crystals form at higher temperatures [Huppert and Woods, 2002, Wallace et al., 2015, Edmonds and Woods, 2018].

In agreement with previous work outlined above, reducing the system's water content from 4 wt% in the reference simulation to 2 wt% results in crystals beginning to form at much higher temperatures. This results in the overall system having a higher viscosity. The reference simulation has an initial viscosity of 2.36 Pa s, while the reduced water content simulation (2 wt%) has an initial viscosity of 3.55 Pa s. Higher viscosity hinders both crystal settling speeds and convective speeds, which are both calculated using Stokes' law and are therefore inherently connected to the viscosity of the system (see Equations 3.8 and 3.9).

A crystal-dense layer forms at the bottom of the system due to crystallisation from the wall rock contact and crystal accumulation from the drips outlined in Figure 4.6. The layer forms rapidly as the system crystallises and has a composition that reflects the overall bulk composition of the system, outlined in Figure 4.11. This layer could be considered similar to that of a chilled margin [Huppert and Sparks, 1989]. However, it is important to note that the fine-grained textures, often observed in nature, which are typically associated with a chilled margin [Huppert and Sparks, 1989, Latypov et al., 2007] cannot be confirmed from the model outputs, as the model cannot resolve textural details.

In agreement with previous work, this study found that variations in volatile content directly influence the convective patterns, crystallisation processes, and the geochemical differentiation within the systems [Phemister, 1934, Huppert and Woods, 2002, Wallace et al., 2015, Edmonds and Wallace, 2017, Edmonds and Woods, 2018, Popa et al., 2021]. Without sufficient volatile-enriched recharge into the system, magma bodies may solidify beyond the critical crystallinity required for eruption and form intrusive igneous rocks Popa et al. [2021].

Popa et al. [2021] found that crystallinity and dissolved volatile content control eruptive styles. For example, explosive eruptions typically occur in magmas with less than 30 vol % crystals and water content below 3.5 wt%. In contrast, magmas with over 55 vol% crystals become rheologically locked, preventing eruption [Popa et al., 2021]. Other factors, such as chamber size and wall rock cooling rate, are also known to play a role in determining the lifespan of melt-rich systems in the upper crust [Spera, 1980, Karakas et al., 2017, Annen, 2009]. Results from this study are consistent with previous findings, showing that larger simulated magma reservoirs cooled more slowly (see Figure 4.5), extending their longevity [Karakas et al., 2017, Spera, 1980, Annen, 2009]. Similarly, slow wall rock cooling rates, which can be linked to the thermal preconditioning of the surrounding crust, can contribute to the slow cooling and longevity of melt-rich systems [Karakas et al., 2017]. Karakas et al. [2017] studied this in greater detail, and they found that younger igneous provinces are less likely to sustain large upper crustal magma bodies due to the insufficient thermal development of the surrounding rock.

5.2 Significance of Water Content Within Open Systems

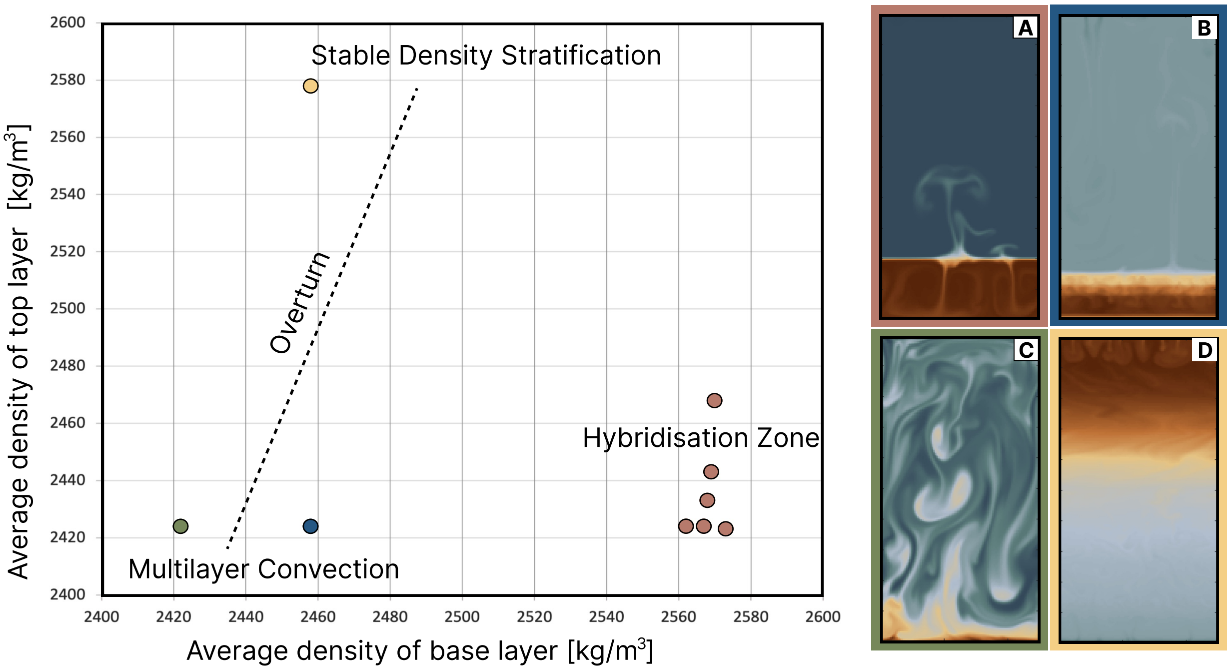

Figure 5.1: Plot of the average densities of the initial two magmas against each other. All open system simulations are plotted on the graph and colour-coded to reflect the dynamic regimes they exhibit. The graph highlights the importance of density contrast within the system and its influence on the internal dynamic regime that develops once the simulation begins. The colours correspond to subplots on the side, which show a temperature snapshot from each dynamic regime to illustrate what it looks like. In pink (A), the models exhibit hybridisation zone dynamics, where the bottom layer is denser than the top layers. The two layers remain stratified with an interface layer (the hybridisation zone) where interaction occurs, forming plumes. In blue (B), the multilayered convection regime occurs when the base layer is still denser than the top, but with less contrast, allowing bubbles to form in the base layer and rise to the interface, creating a middle, bubble-rich layer. The system therefore shifts into a multilayer convection regime with transient fourth layers forming. In green (C), the first overturn simulation shows lower density in the base layer relative to the top, triggering overturn. The system then transitions into the multilayer convection regime. In yellow (D), the second simulation also experiences an overturn event before settling into a final stable density stratification regime, where movement halts with only a small convecting layer remaining at the top.

In the open system simulations, variations in water exsolution significantly affected both the system dynamics and the resulting geochemical signatures highlighted in Figure 4.24. Each variation leads to a distinct dynamic regime, ranging from multilayered convection to complete system overturn outlines in Figure 5.1. The dynamic behaviours are primarily driven by the exsolution of volatiles forming bubbles. The presence of these bubbles alters the density of the magma and its interactions, leading to substantial changes in the system's overall behaviour (see Figure 5.1). The specifics of how each variation in water content produces unique dynamic regimes, including hybridisation zone dynamics, multilayer convection, and system overturn, are discussed in detail in the following sections.

5.2.1 Hybridisation Zone Dynamics Regime

The hybridisation zone dynamic regime is the most commonly occurring regime within this study (Figure 5.1 A). It occurs when the recharge magma is depleted in volatiles relative to the resident magma. The recharge magma settles as a denser layer at the system's base and interacts with the upper resident magma across the contact boundary, forming a hybridisation zone. The hybridisation zone dynamic regime aligns with previous theoretical and laboratory experiments investigating magma recharge beneath more evolved silica rich magma [Huppert and Turner, 1981, Huppert and Sparks, 1981, Campbell and Turner, 1989, Bergantz and Breidenthal, 2001, Perugini et al., 2015, Longo et al., 2023]. Huppert and Sparks [1981] proposed a theoretical model of hot dense magma recharging beneath a lighter fractionated basaltic magma similar to the model set up within this study. They hypothesised that the two layers would remain compositionally distinct; however, the temperatures would equilibrate as temperature diffusion is faster than chemical diffusion [Huppert and Sparks, 1981]. Later laboratory experiments demonstrated this double thermal and chemical diffusive behaviour, and it is also exhibited within the models of this study [Huppert and Turner, 1981, Campbell and Turner, 1989, Bergantz and Breidenthal, 2001, Perugini et al., 2015, Longo et al., 2023]. Within this study, the hybridisation zone is not an effective dynamic regime for mixing. The chemical flux across the zone is relatively slow compared to thermal diffusion this is highlighted within the stable isotope fields see Figure 4.28 A-D and Figure 4.29 A-F .

Within this study, the density of both layers increases over time, maintaining a strong contrast at the interface between the two compositions. This interface is visible in Figure 4.14. The strong contrast observed in the model simulations differs from tank experiments, where bubble exsolution and crystallisation reduce the density of the base recharge layer, promoting chemical mixing between the two magmas and sometimes leading to system overturn [Huppert and Turner, 1981, Huppert et al., 1984, Campbell, 1996, Bergantz and Breidenthal, 2001]. In the current model, any bubbles that exsolve within the lower layer become trapped in the cumulate layer at the base due to rapid cooling, preventing a significant reduction in density (Figure 4.14). In later simulations, bubble formation occurs more widely throughout the base layer as it approaches water saturation.

Campbell [1996] conducted a similar tank experiment in which a denser layer was introduced beneath a less dense one. However, the denser material was injected as a pulse at the base. This pulse carried excess momentum, and their results showed that under such conditions, a dense plume or fountain formed, penetrating the upper layer before falling back again [Campbell, 1996]. This fountain dynamic suggests that different recharge mechanisms could influence the dynamic regimes within magmatic systems [Campbell, 1996].

One exception within the hybridisation zone dynamic regime is exhibited within a simulation with a lower initial resident magma temperature. It is decreased from the reference simulation 985 °C to 959 °C. This simulation set up results in an initial bubble content of 1.6 vol% within the upper resident magma layer.

Due to the reduced temperature in this layer, the water saturation point is lowered, allowing bubbles to exsolve. Over time, as the resident magma is heated by plumes from the hybridisation zone, bubbles gradually redissolve, reducing the bubble volume to 0.7 vol% by the end of the simulation. This suggests that high bubble content in the upper layer stabilises the layers, whereas bubble content in the base layer can lead to instability, overturn, and increased mixing. Across all hybridisation zone simulations, the bottom recharge layer remains denser than the resident magma throughout the runs, as the recharge magmas are not enriched in volatiles. See Figure 5.1.

This hybridisation zone regime matches conceptual models of magma mingling and mixing of injected mafic magma into partially crystallised higher-silica magma [Clynne, 1999, Tepley et al., 1999, Browne et al., 2006, Jarvis et al., 2021]. Additionally, it also matches textural patterns observed in the field, where mingled magmas have crystallised rapidly, preserving evidence of mixing textures [Clynne, 1999, Tepley et al., 1999, Perugini et al., 2003, Jarvis et al., 2021].

5.2.2 Multilayer Convection Dynamic Regime

The second dynamic regime occurs when the water content of both magmas is equal, resulting in stable density stratification (see Figure 5.1). Bubbles that exsolve within the recharge magma rise and stall at the contact between the recharge magma and the resident magma. The rise of bubbles results in the formation of a third layer with a bubble saturated layer sandwiched between two water depleted layers, outlined in Figure 4.16. The bubbles stall and collect at the interface between the two initial magmas due to density and viscosity contrasts between the two compositions, creating stepped density layering [Huppert and Turner, 1981].

The multilayer convective regime mirrors the dynamics observed within laboratory experiments on saline water layering and double diffusive convection [Huppert and Turner, 1981, Sparks et al., 1985, Turner and Campbell, 1986]. In these experiments, heat diffusion across the boundaries drives convection within layers while the remaining salt creates density steps within the system [Huppert and Turner, 1981, Sparks et al., 1985, Turner and Campbell, 1986]. Similarly, in this study, heat diffusion across the boundary equilibrates through the system faster than the composition (Figure 5.1B). Unlike previous tank experiments, the density and viscosity contrasts of the layers here are controlled by phase changes, specifically the exsolution of bubbles from the melt and the formation of crystals outlined in Figure 4.16 C and D. Any bubbles that crossed the boundary layer redissolve into the resident magma as this upper layer is below its saturation point. Over time, as the base recharge layer cools and crystallises, it reaches its saturation point, leading to further bubble formation and a transition to a four-layer convective regime. Eventually, this bubble rich layer amalgamates with the initial bubble rich layer, as their temperature and density homogenise. The amalgamation of the two layers mirrors laboratory experiments, where density equilibrium between layers results in the boundary dissolving and intense mixing of the two compositions [Huppert and Turner, 1981, Bergantz and Breidenthal, 2001]. This more complex dynamic behaviour results in greater mixing of the magma compositions as each convecting layer homogenises.

As the layers that form within this regime are transient, it is not possible to trace the detailed nuances of the regime, such as the number of convecting layers, within the end layer structures. However, this regime does lead to a better-mixed end geochemical signature than the previous hybridisation zone dynamic (see Figure 4.24 and Figure 4.30 A-F), indicating that the increased volatiles play an important role in controlling not only the dynamics but also the geochemistry of the system. The diffuse boundaries between the layers at the end of the simulation (see Figure 4.16 E-F), progressing towards equilibrium, suggest that if the simulation continued longer, the potential continued mixing could homogenise the system further.

5.2.3 System Overturn Dynamic Regime

System overturn occurs when the recharging magma contains a higher water content than the resident magma and exceeds the water saturation point, allowing bubbles to form. The bubbles reduce the density of the recharging magma, creating a buoyancy contrast and causing the recharging magma to rise, see Figure 5.1. This regime is observed in two simulations involving recharge magmas enriched in water relative to the resident magma.

Within the simulation where the recharge magma is enriched by 2 wt% H_2O, there is an initial large density contrast between the two magmas. The top layer has a density of 2578 kg/m^3, while the base layer has a density of 2458 kg/m^3, giving a density contrast of 120 kg/m^3 (see Figure 5.1). In contrast, the initial density contrast is much lower in the simulation with a smaller recharge enrichment (1 wt% H_2O difference). Here, the top layer has a density of 2424 kg/m^3, and the base layer has a density of 2422 kg/m^3, resulting in a density contrast of only 2 kg/m^3 outlined in Figure 5.1.These results suggest overturn dynamics are susceptible to small-density contrasts. Both simulations experience overturn events but display slightly different dynamics during and after the overturn (Figure 5.1 C and D).

In shallow continental arcs, it is well-documented that magma systems are often replenished with hotter, more primitive, volatile-rich magma beneath cooler, more evolved, volatile-depleted magma [Moore and Carmichael, 1998, Annen and Sparks, 2002, Ruscitto et al., 2010, Longo et al., 2012, Plank et al., 2013, Zellmer et al., 2016]. Within this scenario, the resident magma has evolved due to processes such as fractional crystallisation, as outlined in the closed system models (Section 4). Additionally, they become depleted in volatiles, which separate into a gas phase through two main processes: first, boiling during decompression as the magma rises [Wallace et al., 2015, Edmonds and Woods, 2018], and second, boiling as the system cools and crystallises [Wallace et al., 2015, Edmonds and Woods, 2018]. Eventually, the volatile phase decouples from the remaining melt and escapes into the surrounding rock, leaving a volatile, depleted magma [Longo et al., 2012]. Within continental arcs, primitive magmas typically contain 3-5 wt% water [Phemister, 1934, Plank et al., 2013, Edmonds and Woods, 2018] and have not undergone significant first or second boiling upon recharging the shallow system. Therefore, recharge by a more water-enriched magma is a plausible scenario.

Within the water-enriched recharge simulations, the systems overturn within the first few minutes after initiation. The recharge magma rises quickly, destabilising the interface between the two magmas and reaching the top of the chamber, interacting with the resident magma as it does so (Figure 5.1 C and D). This behaviour is well established within laboratory experiments [Turner and Campbell, 1986, Woods and Cowan, 2009] and numerical models [Ruprecht et al., 2008, Garg et al., 2019]. Evidence of overturn dynamics has also been identified within field studies [Longo et al., 2006, Bain et al., 2013, Myers et al., 2014, Garg and Papale, 2022, Longo et al., 2023].

Within the simulation with only slightly higher water contents in the recharging magma (1 wt%) the system begins to stratify after the initial short overturn event (See Figure 5.1 C). It enters a multilayered convective regime similar to the dynamics outlined above; however, it exhibits an unstable boundary layer that appears to ripple (See Figure 4.17 D-F. Over time, the bottom recharge layer "drains," shrinking in size as the whole system homogenises with more extensive chemical mixing across the layers. This increased mixing can be seen within the stable isotope data see Figure 4.31. This indicates that a composition change of only 1 wt% water can result in significant internal dynamic changes and that these dynamic regimes are sensitive to small variations in bubble and water content.

Within the final simulation (2 wt%) difference between magmas, the system becomes stably stratified in terms of density after the initial overturn event illustrated in Figure 4.18. The density gradient between layers reaches a stable state, preventing further large-scale mixing or overturning. However, there are still variations in composition and temperature within the layers, reflecting ongoing processes such as crystallisation and water exsolution, see Figure 5.1 D). Over time, a convection cell at the top of the system begins to erode the stable diffuse layer, homogenising the system as it grows in depth. This can be seen within the stable isotope parameter fields outlined in Figure 4.28 E-H. The results of this study align with those of Garg et al. [2019] and Ruprecht et al. [2008], which also observe the interface destabilisation, plume rise and mixing of magma, followed by the gradual development of well-defined, stratified layers. Huppert and Sparks [1980] found that within tank experiments, if the density of the recharge magma became equal to or greater than the resident magma, the recharge magma would rise and mix with the upper system.

The distinction between this regime and the previous one has important implications for the geochemical signatures. Where there is only slight water enrichment of the recharging magma, some of the magma may remain at the bottom of the system during overturn. This results in trace element compositions and isotope ratios closer to those of the recharge magma within the cumulate layer outlined in Figure 4.26 and Figure 4.31. However, within the case of greater variation in H_2O content, the overturn is more successful in flipping the system, and the cumulate layers have trace element signatures that resemble the resident magma see Figure 4.27.

The overturn dynamic regimes lead to extensive mixing between the two magma compositions on relatively fast time scales (from minutes to hours), much faster than differentiation trends observed within the closed system and hybridization zone models (See Figure 4.28 A-H). The rapid mixing emphasises the critical role of water-rich recharge in controlling the geochemistry. The overturn dynamics and multilayer convection regimes are much faster at evolving the geochemistry of the system than evolution via crystal settling and differentiation.

5.3 Plume Dynamics in Closed-System Simulations

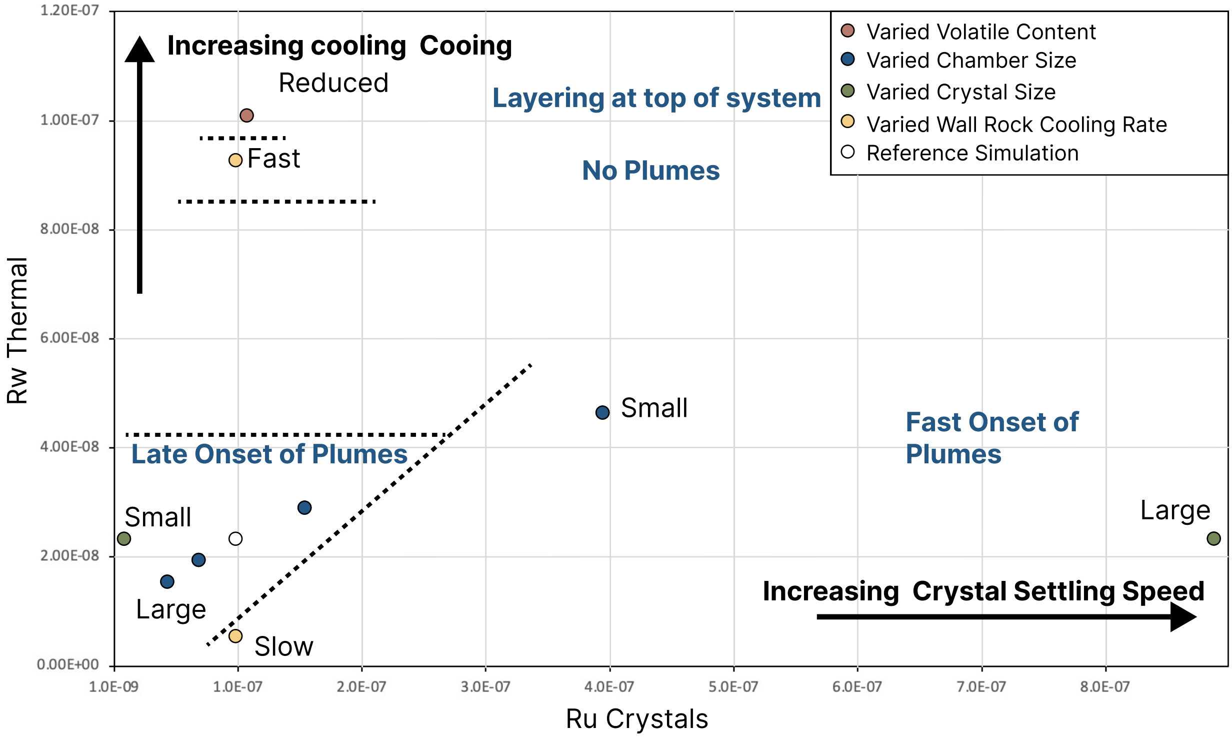

Figure 5.2: Regime diagram of the closed system models, plotting dimensionless values of Ru (Crystals) on the x-axis and Rw (Thermal) on the y-axis. This diagram highlights the influence of boundary cooling and crystal settling in determining plume formation. The simulations are colour-coded based on parameter variations, with labels indicating whether each simulation involved a higher, lower, faster, or slower variation from the reference simulation. The results show that simulations with fast cooling across the boundary (high Rw) and slow crystal settling (low Ru) do not develop plumes. In contrast, simulations with slow cooling (low Rw) exhibit plume formation, with the crystal settling rate controlling the onset of plumes. Simulations with faster crystal settling (high Ru) experience earlier plume formation, while those with slower settling rates (low Ru) have plumes form later. This highlights the interplay between cooling rates and crystal dynamics in regulating the timing and presence of plumes in the system.

Across the ten closed-system simulations, one key variation in internal dynamics is the presence or absence of plumes at the bottom of the chamber. Plume formation was not restricted to any specific set of parameter variations. Small changes in parameter values influence the timing, morphology, and frequency of plume formation. Figure 5.2 illustrates the plume dynamics and their relation to two non-dimensional parameters: Ru and Rw.

Ru (Relative Importance of Buoyancy vs Crystal Settling) measures the balance between buoyant forces driving magma convection and the settling of crystals. A higher Ru indicates that buoyancy is more dominant, while a lower Ru suggests that crystal settling plays a greater role (See Figure 5.2).

Rw (Ratio of Convective Speed to Cooling Speed) compares the convection speed within the magma to the characteristic cooling speed across the boundary layer. A higher Rw value signifies that convection dominates over cooling processes, affecting plume development. Conversely, a lower Rw means that cooling processes have a stronger influence. The interplay between Ru and Rw leads to different plume shapes, timings, and frequencies, as observed in the simulations (See Figure 5.2).

Understanding these parameters shows how variations in crystal size, chamber size, and wall rock cooling rates affect plume formation and behaviour. As mentioned in the Results (section 4), parameter tests influenced the convective speed of the systems. Plumes are most prominent in systems with slower convection, such as those with reduced wall rock cooling rates and smaller chamber sizes. They are also present in both simulations with varied crystal sizes.

The plumes form from thin, water-rich layers at the interface between the base cumulate layers and the rest of the melt-rich system above. The model setup does not allow water to partition into the solid crystal phase; it is only present in the liquid melt and volatile bubble phases. Therefore, crystallisation leads to enrichment of water within the melt phase. The melt above the cumulates becomes enriched in water. Crystal settling at the base increases crystal volume within the crystal layering and a displacement of melt upwards, further aiding in the accumulation of water-rich melt above the crystal layering. Once the water content of the melt layer reaches approximately 4.1 wt% water, thin plumes begin to rise from the boundary. At the very base of these plumes, bubbles may exsolve, adding to the buoyancy instability driving the flow; however, they quickly redissolve. This behaviour is similar to de-watering events observed in nature where melt is expelled from cumulate layering due to compaction of crystals, [Shirley, 1986, Meurer and Boudreau, 1998].

The large system simulations (75 m × 25 m) and (60 m × 30 m) experience faster cooling across the boundary layers, see Equation 3.14, this leads to faster crystallisation at the wall rock contacts. Additionally, when wall rock cooling rates are decreased from 48 hr to 3 hr at the top and bottom boundary's the model exhibits fast crystallisation rates this is highlighted in Figure 4.2 C. If a system is crystalising faster at the base, it becomes harder for the water rich melt and bubbles to escape and migrate upwards through the mushy cumulate layer, and they become trapped. The cumulate layer, therefore, becomes enriched in water, inhibiting the water from migrating through the layer and forming a water rich melt layer above the cumulate pile. As a result plumes do not form or may take longer to form (See Figure 5.2).

The crystal size affects the crystal settling speed (Equation 3.13), which in turn influences the melt segregation speed. Therefore, larger crystals equal faster crystal and melt segregation. The melt can escape quickly from the crystal layering and form plumes (See Figure 5.2).

The plumes have little impact on the overall flow. Instead, they migrate in response to stronger convection currents caused by crystal downwelling's at the top of the chamber (see Figure 4.3). The plumes are not visible within the major oxide values, trace elements or stable isotopes. Indicating that this dynamic behaviour is not traceable within the resulting geochemistry.

Across the simulations, many of the cumulate layers contain $>$ 10 vol% bubbles; however, this is not typically observed in natural systems, as bubbles that do form are generally expected to rise and escape from the system [Toramaru et al., 1996, Charlier et al., 2015]. In a study by Toramaru et al. [1996], the Ogi picrite sill on Sado Island, Japan, was investigated, where bubble-rich layering was observed forming at the top and base of the sill in regions of rapid crystallisation within volatile-rich melts [Toramaru et al., 1996]. Toramaru noted that such bubble layering is uncommon in most sills, occurring only in relatively small systems at shallow depths and without hydrous mineral formation [Toramaru et al., 1996]. The model used in this study does not currently allow for the formation of hydrous minerals such as amphibole and biotite, as the volatile water phase is not permitted to partition into the solid phase. Consequently, the elevated bubble volume in the cumulate layers is an artefact of model simplification. Therefore, the high bubble fraction in the cumulate layers should be interpreted cautiously and considered a product of model limitations rather than a representation of natural magmatic processes.

5.4 Backtracking to Initial End Member Compositions

Predicting magma end member compositions is challenging due to poorly constrained data sets [Blum-Oeste and Wörner, 2016]. Using model-simulated data where the original end member compositions are known allows for the assessment of Machine learning techniques as a method to backtrack to initial end member values. The results from this study demonstrate that when all data points from a 2D domain are present, end members can be successfully predicted for simulations that have not undergone significant mixing or interaction between the two magmas. The errors for the different models are outlined in Figure 5.3. The machine learning approach successfully identified and discounted fractionation trends within the simulations. However, the simulations were not run for an extended period, meaning the fractional crystallisation trends remain relatively minor compared to the initial geochemical variations. If the models were to run longer, allowing for the fractionation trends to become more prominent, predicting the end members could become more challenging.

Within more dynamically complex scenarios, the prediction of end members was unsuccessful (See Figure 5.3). Even slight changes in system dynamics can overwrite and destroy original geochemical signatures in systems that have not significantly evolved. The introduction of assimilation trends and real-world complexities could further complicate backtracking efforts.

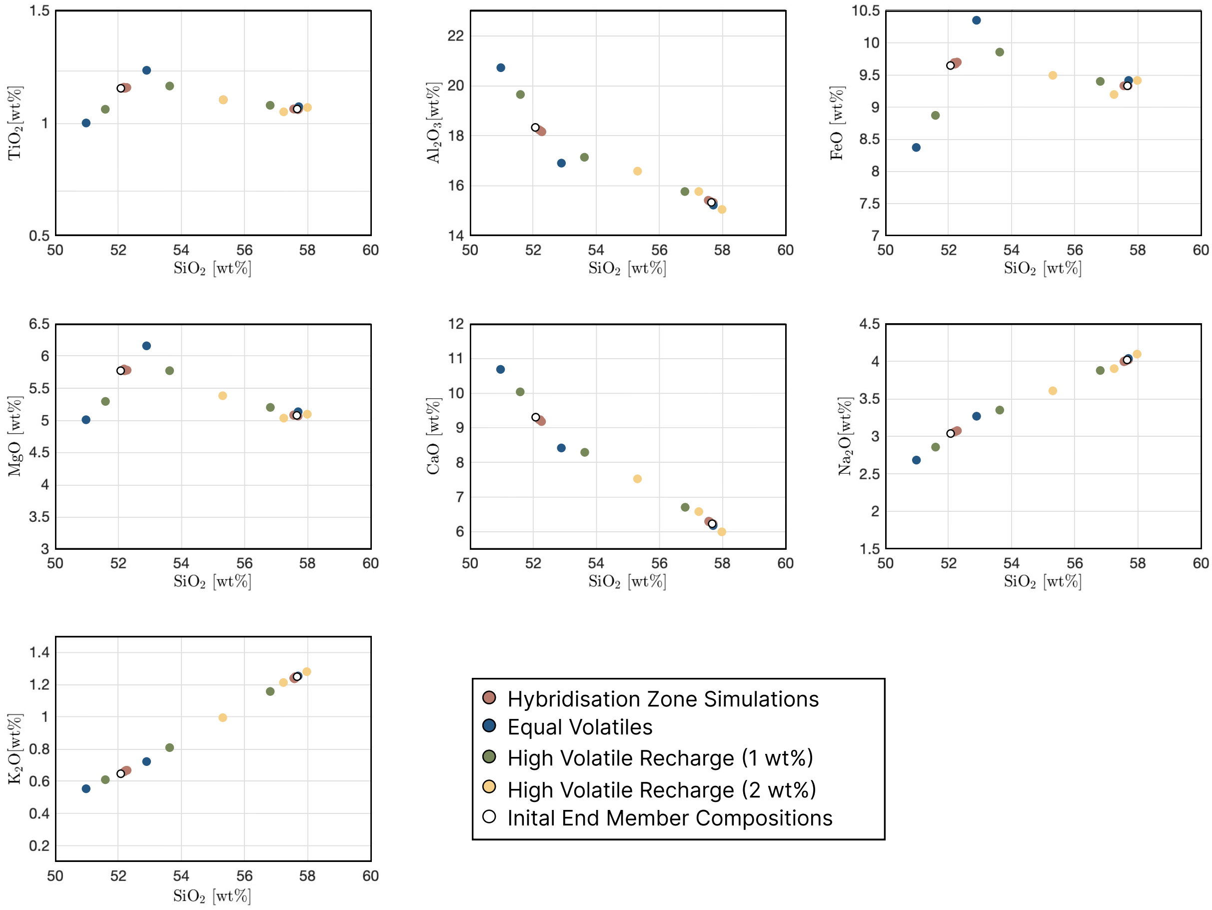

Figure 5.3: Harker plot of major oxides displaying data from the open system machine learning analysis. This data is from the run that included all data points for every point within the system. The points are colour coded to the individual simulations. With all the simulations that experience hybridisation zone dynamics grouped together. This highlights that across all the simulations, there is variable success when predicting the end member compositions.

Despite these challenges, the success within the simple examples and work from the literature suggests that continued refinement of machine learning techniques may improve their predictive accuracy [Blum-Oeste and Wörner, 2016, Ueki et al., 2018, Petrelli et al., 2020, Boschetty et al., 2022, Weber and Blundy, 2024]. For instance, previous work suggests that analysing 17 elements and stable isotopes is necessary to make confident predictions about geological settings [Ueki et al., 2018]. However, the approach to identifying different geological settings is quite different from understanding geological processes. Identifying geological settings involves excluding various magmatic processes to determine the composition of the primary magma, which can be inherently complex.

Results from this study suggest that major oxides and trace elements are good tracers for the end member compositions. The simulations with 50 and 25 random samples show that end member compositions can be identified even with reduced data for simple hybridisation zone systems. Improved results from the targeted samples at the top and base of the systems suggest that the margins of the systems may be less involved within the system dynamics, potentially preserving end-member compositions. Preservation may result from reduced mixing in these regions or from early crystallisation driven by contact with cooler wall rock, which locks in the original magma composition before significant mixing occurs [Huppert and Sparks, 1988, Marsh, 1989] Overall, further work and refinement in machine learning approaches could enhance their effectiveness as predictive tools in geochemical studies.

Chapter 6

Limitations, Future Work and Conclusions

6.1 Limitations

The model utilised within this study integrates fluid mechanics and thermochemical evolution and is one of the first to track the geochemical evolution of a magmatic system. It simulates four pseudo-components that resolve mineral systems and major oxides. It also calculates one volatile phase (water) and four hypothetical trace elements with varying partition coefficients, simulating incompatible to incompatible behaviour. Finally, it tracks two hypothetical stable isotope systems that act as passive tracers of mixing and are used to backtrack to the initial end-member compositions. Despite the advances in incorporating geochemistry, this modelling approach has several limitations. One important limitation is that it excludes the formation of hydrous mineral phases.

Due to computational complexity, the Nakhla model does not allow water to partition into the crystal phase, preventing the formation of hydrous minerals such as amphibole and biotite. This study uses the model to simulate sill-like magmatic systems (50 m thick) with an initial water content of 4 wt%, see table 4.1. The magma is above the water saturation point at shallow depths and pressures, leading to degassing that reduces the water content [Zimmer et al., 2010]. However, hydrous mineral phases such as amphibole and biotite are commonly observed in shallow arc systems, [James, 1982, McMillan et al., 1989, Samaniego et al., 2005, Annen et al., 2006, Bryant et al., 2006, Sainlot et al., 2020]. Therefore, the model's inability to simulate these hydrous minerals introduces inaccuracies in predicting the real-world mineral assemblages for these systems.

A second limitation of the model is that, for computational simplicity, the pseudo-phase diagram approximates everything by linear solution-type phase relations; therefore, all components in the model can co-exist at the same time. This allows olivine and quartz to exist within the cumulate layer, which is unlike a natural system where they would normally not occur together, as they are on either side of the eutectic [Bowen, 1928, Philpotts and Ague, 2009]. Another limitation of the geochemical data is that the model partition coefficients are set at a constant value to simplify computational complexity and to provide a simple understanding of basic scenarios. Future work could dynamically alter the partition coefficients as a function of T, P and water content to mimic real-world partitioning behaviour [Blundy and Wood, 1994, Philpotts and Ague, 2009]. Addressing the variability in partitioning behaviour based on the stable mineral phase assemblage could significantly improve the model.

Other than limitations associated with the calculation of geochemical parameters within the model, there are also several limitations associated with the data of this study. Due to time constraints, the simulations were only run for one month of real-world time. The computational complexity of these simulations meant that the internal evolution of these models was limited to approximately 83 hr for the longest run. This restriction meant only the initial dynamics were captured, including the initial stages of fractional crystallisation trends.

Additionally, there are unresolved questions about the trace element signatures in closed systems. The melt-rich layer shows unexpected compatibility trends at the top of the cumulate stack. It has a slight enrichment of compatible trace elements, while the crystal-rich layers below are slightly depleted in these elements. One hypothesis for this behaviour is that melts within the mushy, crystal-rich layers become enriched in compatible elements. This enrichment occurs because the higher volume of crystals in these layers concentrates compatible elements in the melt. As more crystals form and accumulate, these enriched melts are fluxed upwards.

The observed signatures are subtle and might be related to transient behaviours that could become more apparent if the simulations were run for a longer period. Additionally, this behaviour is occurring within a very narrow layer above the crystals, confined to a single grid square. This indicates that the dynamics are happening at a scale smaller than the model's resolution, highlighting resolution as another limitation of the model. As a result, accurately predicting fine-scale behaviours is challenging.

Further tests and investigations are required to address these limitations. Improving the model's resolution and extending the simulation duration will help resolve these issues and provide a clearer understanding of the dynamics. This is outlined in the next section on future work.

6.2 Future Work

Future work could expand on both the numerical modelling itself to address the model's limitations and the geological questions and context. Adding additional processes, such as wall rock assimilation and a third geochemical composition, may reveal more about the survival of geochemical signatures and the internal complexities of these shallow systems. Additionally, greater investigation on the role of water content within different chamber dynamics and geometries may help fill knowledge gaps. Varied recharge dynamics could be tested to include continuous recharge from a single point, with different recharge rates and compositions. As mentioned previously Campbell [1996] showed that within tank experiments recharge injected into the base of a system rose as a fountain due to excess momentum, which may change the dynamic regime.

Further expansion of the model to include pressure variations (including depressurisation) and interactions between the magma system and the surrounding country rock would enable testing more complex hypotheses related to system overpressure and volcanic eruptions. This could involve simulating effects such as wall rock fracturing and the dynamics of how the magma interacts with and influences the surrounding rock. Work within this area has already begun with [Li et al., 2023], incorporating this model within more mechanically complex crustal magma systems.

The current model does not allow for the formation of hydrous minerals such as amphibole and biotite, as the volatile water phase is not permitted to partition into the solid phase. As a result, the high bubble volume observed in the cumulate layers is an artefact of this simplification. Therefore, these bubble-rich cumulate zones should be interpreted cautiously, as they likely do not represent natural magmatic processes. Future work could incorporate hydrous mineral formation to represent a more realistic composition and reduce the artificially elevated volatile content and bubble fraction in the cumulate layers.

The current study employs hypothetical trace elements to investigate mixing and fractionation trends. While useful for exploring model behaviours, the lack of specifically defined trace elements limits direct comparison with natural systems. Future work could improve this by calibrating the model to include real-world trace elements. This would allow for ground truthing of the model by comparing it to real-world case studies, which is an essential step to enhance the models validity and applicability.

As outlined in the methods section the model framework contains two isotope ratios however, for the purposes of this study only one was required to track the extent of homogenisation between two magmas. The isotopes were therefore defined to have correlated values that show the same trends. Future work could utilise the second isotope ratio to understand additional processes such as assimilation. Additional isotope ratios could be added and defined using real world systems to aid in ground truthing the model as well as understanding more specific dynamics.

Furthermore, extending the model to include multiple magma chambers would enable the investigation of far-reaching signatures and interactions between these systems. This could potentially reveal new insights into the dynamics of magmatic systems. Additionaly incorporating realistic recharge rates and coupling the model with a dynamically self-consistent representation of a subducted slab model could further enhance its realism [Grima et al., 2020, Grima and Becker, 2024]. Integrating processes occurring in the lower crust would provide a more comprehensive view of the magmatic system, offering a deeper understanding of its evolution and behaviour. By expanding the scope of this model for future work, a more robust and accurate model can be developed, enhancing the simulation of natural geological systems and the processes that occur within them.

This work also underscores the necessity of high-resolution field sampling to capture the dynamic nature of these systems. While traditional geological sampling and whole-rock geochemistry may be limited by lower spatial sampling density, portable X-ray fluorescence (XRF) can significantly increase the number of data points collected in a short time, albeit with potentially lower geochemical quantification accuracy compared to laboratory-based methods [Hou et al., 2004]. Integrating these advanced techniques more regularly into geological studies could provide valuable insights and improve the calibration and validation of geodynamic models.

6.3 Conclusions

The main aim of this study was to utilise a numerical model to understand the magma dynamics within shallow crustal magma bodies and how these processes contribute to the generation or destruction of geochemical heterogeneity. The study's findings show that the water content of recharging magma is a major control on the internal dynamics of these systems. Even slight variations (1 wt% H_2O) can result in dramatic changes in dynamic regimes, with the caveat that the magma also crosses the water saturation point/threshold. If the magma does not reach this saturation point, the dynamics remain more stable, exhibiting hybridisation zone behaviour where there is only slight interaction between the two magmas across their contact. The hybridisation zone dynamics lead to less convective interaction between the two magmas and less geochemical homogenisation.

While other parameters, such as wall rock cooling rates, temperatures, length scales, and recharge volumes, have a lesser impact on the dynamics and geochemistry, they still affect the timescales on which these dynamics occur. These parameters may influence the subsequent geochemistry if the simulations were extended over longer periods. Ultimately, this study highlights how variations in water content of recharging magma into a shallow continental arc system can dramatically alter the internal dynamics. High water content recharge magmas can trigger convective overturn and mixing between the two magmas, altering the geochemical signatures, beyond a point where it is possible to backtrack to the initial compositions using machine learning. This study has implications for field data in that the shallowest systems could obscure or erase signatures from the deeper system if they have experienced extensive mixing and overturn. In less convective systems, the original geochemical signatures can be preserved at the top and base margins of the system.

Chapter 7

Appendix

The tables below outline the petrological model composition parameters. The composition is specified as oxides, mineral endmembers, mineral systems and pseudo components (melting model components).

7.1 Appendix 1

Mineral	SiO_2	TiO_2	Al_2O_3	FeO	MgO	CaO	Na_2O	K_2O	H_2O
Forsterite (for)	42.7	0.0	0.0	0.0	57.3	0.0	0.0	0.0	0.0
Fayalite (fay)	29.5	0.0	0.0	70.5	0.0	0.0	0.0	0.0	0.0
Ulvospinel (ulv)	0.0	32.0	2.6	46.2	19.2	0.0	0.0	0.0	0.0
Magnetite (mgt)	0.0	22.3	1.3	71.0	5.4	0.0	0.0	0.0	0.0
Ilmenite (ilm)	0.0	44.2	0.6	54.9	0.3	0.0	0.0	0.0	0.0
Enstatite (ens)	51.5	0.0	3.3	20.4	22.2	2.6	0.0	0.0	0.0
Hypersthene (hyp)	49.4	0.0	1.0	36.4	12.0	1.2	0.0	0.0	0.0
Al-augite (cp1)	52.6	0.0	2.15	9.3	15.58	19.87	0.44	0.06	0.0
Augite (aug)	52.78	0.0	0.85	15.41	11.78	18.07	1.06	0.05	0.0
Pigeonite (pig)	51.4	0.0	1.31	23.25	5.03	15.72	2.95	0.34	0.0
Anorthite (ant)	44.4	0.0	35.8	0.0	0.0	19.3	0.5	0.0	0.0
Albite (alb)	67.3	0.0	20.2	0.0	0.0	0.5	11.5	0.5	0.0
Sanidine (san)	64.8	0.0	18.3	0.0	0.0	0.0	0.5	16.4	0.0
Quartz (qtz)	100.0	0.0	0.0	0.0	0.0	0.0	0.0	0.0	0.0
Water (wat)	0.0	0.0	0.0	0.0	0.0	0.0	0.0	0.0	100.0

Table 7.1: Table from the model calibration script showing the oxide compositions of each mineral end member (in wt%).

System	for	fay	ulv	mgt	ilm	ens	hyp	cp1	aug	pig	ant	alb	san	qtz
Olivine	1	1	0	0	0	0	0	0	0	0	0	0	0	0
Oxide	0	0	1	1	1	0	0	0	0	0	0	0	0	0
Orthopyroxene	0	0	0	0	0	1	1	0	0	0	0	0	0	0
Clinopyroxene	0	0	0	0	0	0	0	1	1	1	0	0	0	0
Feldspar	0	0	0	0	0	0	0	0	0	0	1	1	1	0
Quartz	0	0	0	0	0	0	0	0	0	0	0	0	0	1

Table 7.2: Table from the model calibration script showing the mineral systems represented by combinations of mineral end members. A value of 1 indicates membership in the system. Mineral end members are indicated using there abbreviations from the previous table.

Mineral (shorthand)	Anorthosite	Basalt	Andesite	Rhyolite	Fluid
Forsterite (for)	0.0000	5.0543	0.1965	0.0000	0.0000
Fayalite (fay)	0.0000	6.9548	3.4037	0.0000	0.0000
Ulvospinel (ulv)	0.0000	3.6012	0.5051	0.0000	0.0000
Magnetite (mgt)	0.0000	3.0760	2.1748	0.0244	0.0000
Ilmenite (ilm)	0.0000	0.2390	0.1436	0.1004	0.0000
Enstatite (ens)	0.0000	15.9769	0.3661	0.0000	0.0000
Hypersthene (hyp)	0.0000	1.3431	8.8642	0.0000	0.0000
Al-augite (cp1)	0.0000	18.2853	0.0563	0.0000	0.0000
Augite (aug)	0.0000	1.5396	5.6639	0.0000	0.0000
Pigeonite (pig)	0.0000	0.4692	0.8425	1.9774	0.0000
Anorthite (ant)	100.0000	35.4479	10.8493	0.0000	0.0000
Albite (alb)	0.0000	8.0127	64.1367	24.1666	0.0000
Sanidine (san)	0.0000	0.0000	1.9340	29.0199	0.0000
Quartz (qtz)	0.0000	0.0000	0.8632	44.7114	0.0000
Water (wat)	0.0000	0.0000	0.0000	0.0000	100.0000

Table 7.3: Table from the model calibration script. Mineral end-member compositions (in wt%) of melting model pseudo-components: anorthosite, basalt, andesite, rhyolite, and hydrous fluid.

7.2 Appendix 2

Varied Temperature Values description:

The second parameter test saw the variation on the initial temperatures of the two magma's. the first three models saw variation of the resident magma temperature decreasing across the three, outlined in Table 4.4. This reduction was correlated with the initial crystal vol % of the magma. The three models therefore represent 5 vol%, 10 vol% and 20 vol% crystal volume respectively. This variation was carried out to ascertain if the state of the magma system that is recharged has a role on the internal dynamics. The last two models within this group have varied recharge magma temperatures varied by ±35°C (Table 4.4. Across all five models they all display the same dynamic behaviour as seen in the previous parameter test consisting of a hybridisation zone between two convecting magma compositions.

Within the first three models, as the temperature of the resident magma decreases, the convective speed of the top layer slightly increases and becomes more variable, with the cooler magma of the 959°C exhibiting a slower convection speed of 154 m/hr at the top and 98 m/hr at the base. This is faster than the warmer base model where the top layer convect at 91 m/hr and the base at 50 m/hr. There is a greater temperature difference between the two magmas in the 959°C simulation therefore a greater thermal density difference. In all 3 models, the crystal volume of the top convecting layer decreases as it is heated by plumes from below and as crystals settle into the base layer. The remaining two models within the parameter test have varied recharging magma temperatures. The model with 1200°C recharge mamga has a recharge magma reduced by 35°C from the base and the second model has an increased temperature of recharge magma by 35°C to 1270°C. Like the three other models varying the temperature of the interacting magmas influences the respective convective speeds. In the model with 1200°C recharging mamga the top layer is unaffected by the decrease in temperature and convects at 91 m/hr which matches the baseline simulation. However, the base layer has a slower convection rate of 40.3 m/hr. Within the model with 1270°C recharge both convective speeds increase with the top layer convecting at 99 m/hr and the base convecting at 57 m/hr. There is no change in the dynamic behaviour of these models, only variations in dynamic speeds and timescales.

7.3 Appendix 3

The following tables summarise the bulk mineralogical compositions of the cumulate layers formed in each simulation. These layers represent the final crystallised assemblages at the end of each model run. While all simulations produced a cumulate, the total volume of crystallisation varied depending on the imposed parameters (chamber size, cooling rate, recharge conditions). The tables are divided into closed and open system simulation groups.

Model ID	**Olivine wt%**	**Spinel wt%**	**Opx wt%**	**Cpx wt%**	**Feldspar wt%**	**Quartz wt%**
Closed_Reference	5.87	3.68	9.97	10.49	56.88	9.35
Slow_Wall_rock_cooling	5.65	3.52	9.57	9.81	46.53	2.43
Fast_Wall_rock_cooling	5.86	3.68	9.97	10.48	56.83	9.31
Larger_Crystals	6.03	3.77	10.17	10.76	57.43	9.31
Smaller_Crystals	5.82	3.66	9.91	10.41	56.81	9.41
Smallest_Chamber_25	5.99	3.75	10.14	10.68	57.05	9.11
Small_Chamber_40	5.91	3.71	10.03	10.03	56.95	9.27
Large_Chamber_60	5.83	3.66	9.92	10.43	56.85	9.44
Largest_Chamber_75	5.81	3.65	9.89	10.40	56.80	9.48
Lower_Water (Base)	6.02	3.78	10.23	10.75	57.87	9.31
Lower_Water (Top)	4.60	2.97	8.12	8.58	57.76	14.63

Table 7.4: Closed system model and there cumulate layer mineral composition in weight percentages.

Model ID	**Olivine wt%**	**Spinel wt%**	**Opx wt%**	**Cpx wt%**	**Feldspar wt%**	**Quartz wt%**
Open_Reference	6.42	3.91	10.35	11.13	60.77	3.78
Smallest_Rech_volume_5	6.62	4.03	10.66	11.50	60.69	4.40
Small_Rech_volume_10	6.54	3.98	10.54	11.36	61.06	4.42
Small_Rech_volume_15	6.47	3.94	10.44	11.25	61.35	4.44
Large_Rech_volume_30	4.56	2.70	6.98	7.76	39.65	0.09
Large_Rech_volume_40	3.13	1.84	4.72	5.31	32.07	0.05
Largest_Rech_volume_50	1.63	0.96	2.45	2.77	25.13	0.02
Equal_Water	5.69	3.43	9.02	9.71	56.47	0.20
High_Water_Rech_1	6.21	3.78	10.02	10.80	61.76	4.34
Higher_Water_Rech_2	6.12	3.83	10.34	10.89	57.89	8.83
Lower_Res_temp_973	5.47	3.26	8.49	9.32	44.37	0.13
Lower_Res_temp_968	4.34	2.56	6.60	7.37	36.06	0.08
Lower_Res_temp_959	3.32	1.95	5.00	5.63	29.65	0.05
Lower_Rech_temp_1200	6.47	3.95	10.44	11.26	61.31	4.45
Higher_Rech_temp_1270	6.37	3.87	10.27	10.95	57.51	1.45

Table 7.5: Open system model and there cumulate layer mineral composition in weight percentages

7.4 Appendix 4

Machine Learning Error value tables: Errors for the recharge end member, resident end member, total error and the number of end members asked for.

Model ID	Recharge End Member Error	Resident End Member Error	Overall Error	No of End Members
Open_Reference	0.0034	0.0007	0.0024	2
Smallest_Rech_volume_5	0.0022	0.0002	0.0015	2
Small_Rech_volume_10	0.0041	0.0002	0.0028	2
Small_Rech_volume_15	0.0045	0.0008	0.0031	2
Large_Rech_volume_30	0.0038	0.0018	0.0029	2
Large_Rech_volume_40	0.0029	0.0019	0.0024	2
Largest_Rech_volume_50	0.0025	0.0028	0.0027	2
Equal_Water	0.0370	0.0051	0.0256	3
High_Water_Rech_1	0.0148	0.0069	0.0113	3
Higher_Water_Rech_2	0.0694	0.0079	0.0478	3

Table 7.6: Error norm values for the predicted end members of Major Oxides.

Model ID	Recharge End Member Error	Resident End Member Error	Overall Error	No of End Members
Open_Reference	0.0054	0.0013	0.0038	2
Smallest_Rech_volume_5	0.003	0.0009	0.0022	2
Small_Rech_volume_10	0.006	0.0005	0.0041	2
Small_Rech_volume_15	0.0058	0.0009	0.004	2
Large_Rech_volume_30	0.0043	0.0021	0.0033	2
Large_Rech_volume_40	0.0026	0.0026	0.0029	2
Largest_Rech_volume_50	0.0027	0.0028	0.0028	2
Equal_Water	0.0036	0.0083	0.0065	2
High_Water_Rech_1	0.0225	0.0233	0.0229	2
Higher_Water_Rech_2	0.0836	0.0097	0.0576	3

Table 7.7: Error norm values for the predicted end members of Major Oxides and Trace Elements.

Model ID	Recharge End Member Error	Resident End Member Error	Overall Error	No of End Members
Open_Reference	0.0086	0.0021	0.0061	2
Smallest_Rech_volume_5	0.0065	0.0005	0.0045	2
Small_Rech_volume_10	0.0029	0.0011	0.0021	2
Small_Rech_volume_15	0.0075	0.0016	0.0052	2
Large_Rech_volume_30	0.0052	0.0027	0.0041	2
Large_Rech_volume_40	0.0039	0.0034	0.0037	2
Largest_Rech_volume_50	0.0028	0.0039	0.0035	2
Equal_Water	0.0162	0.0091	0.0129	3
High_Water_Rech_1	0.0232	0.0250	0.0242	3
Higher_Water_Rech_2	0.0906	0.0091	0.0623	3

Table 7.8: 50 random sample analysis, error norm values for the predicted end members and overall error.

Model ID	Recharge End Member Error	Resident End Member Error	Overall Error	No of End Members
Open_Reference	0.0069	0.0021	0.005	2
Smallest_Rech_volume_5	0.0065	0.0004	0.0045	2
Small_Rech_volume_10	0.0029	0.0011	0.0021	2
Small_Rech_volume_15	0.0062	0.0017	0.0044	2
Large_Rech_volume_30	0.0036	0.0027	0.0032	2
Large_Rech_volume_40	0.0027	0.0034	0.0031	2
Largest_Rech_volume_50	0.0018	0.0040	0.0032	2
Equal_Water	0.0162	0.0091	0.0129	3
High_Water_Rech_1	0.0232	0.0251	0.0242	3
Higher_Water_Rech_2	0.0907	0.0094	0.0624	3

Table 7.9: 25 random sample analysis, error norm values for the predicted end members and overall error.

Model ID	Recharge End Member Error	Resident End Member Error	Overall Error	No of End Members
Open_Reference	0.0029	0.0023	0.0026	2
Smallest_Rech_volume_5	0.0044	0.0004	0.003	2
Small_Rech_volume_10	0.0039	0.0012	0.0028	2
Small_Rech_volume_15	0.0024	0.0018	0.0021	2
Large_Rech_volume_30	0.002	0.0029	0.0025	2
Large_Rech_volume_40	0.0024	0.0035	0.0031	2
Largest_Rech_volume_50	0.0024	0.0040	0.0034	2
Equal_Water	0.0077	0.0091	0.0085	3
High_Water_Rech_1	0.0264	0.0251	0.0257	3
Higher_Water_Rech_2	0.0897	0.0002	0.0613	3

Table 7.10: Error norm values for the predicted end members of the intentional sampling analysis.

Chapter 8

Supplementary Data

Supplemental material can be accessed at:

Swan, S. (2024, September 30). Master's Thesis: 2D Numerical Simulations of Shallow Crustal Magma Bodies. Zenodo. https://doi.org/10.5281/zenodo.15540075

Declaration of AI use:

I acknowledge the use of ChatGPT 3.5 (Open AI, https://chat.openai.com) [January 2024 and August 2024]. It was used to assist with troubleshooting and debugging MATLAB scripts that processed and plotted model output data. ChatGPT provided explanations for error messages, suggested potential ways of fixing code and in some cases offered code snippets. I critically analysed and edited all code suggestions.

I acknowledge the use of Grammarly (https://www.grammarly.com/) [July 2024 and August 2024]. Grammarly assisted with grammar, spelling, and sentence structure. Grammarly's built-in AI-powered suggestions helped with word choice and the phrasing of individual sentences. These suggestions were reviewed and either accepted or rejected by me.

In alignment with the university's AI policy, I confirm that this thesis represents my own work, critical evaluation, and experience. No part of the AI generated output is presented as original or independent thought. AI tools were used solely as a 'conversational partner' for code debugging and to support improvements in grammar and clarity.

Bibliography

A. Adams. Insights into the source of magmatic hot-lines: Forty years of geophysical studies of the cameroon volcanic line. *Frontiers in Earth Science*, 10:838993, 2022.

J. Al Kubaisy, P. Salinas, and M. D. Jackson. A hybrid pressure approximation in the control volume finite element method for multiphase flow and transport in heterogeneous porous media. *Journal of Computational Physics*, 475:111839, 2023.

L. Alisic, S. Rhebergen, J. F. Rudge, R. F. Katz, and G. N. Wells. Torsion of a cylinder of partially molten rock with a spherical inclusion: Theory and simulation. *Geochemistry, Geophysics, Geosystems*, 17(1):143–161, 2016.

C. Annen. From plutons to magma chambers: Thermal constraints on the accumulation of eruptible silicic magma in the upper crust. *Earth and Planetary Science Letters*, 284(3-4): 409–416, 2009.

C. Annen and R. Sparks. Effects of repetitive emplacement of basaltic intrusions on thermal evolution and melt generation in the crust. *Earth and Planetary Science Letters*, 203(3-4): 937–955, 2002.

C. Annen, J. Blundy, and R. Sparks. The genesis of intermediate and silicic magmas in deep crustal hot zones. *Journal of Petrology*, 47(3):505–539, 2006.

C. Annen, J. D. Blundy, J. Leuthold, and R. S. J. Sparks. Construction and evolution of igneous bodies: Towards an integrated perspective of crustal magmatism. *Lithos*, 230:206–221, 2015.

A. M. M. Ardila, S. R. Paterson, V. Memeti, M. A. Parada, and P. G. Molina. Mantle driven cretaceous flare-ups in cordilleran arcs. *Lithos*, 326:19–27, 2019.

A. A. Bain, A. Jellinek, and R. A. Wiebe. Quantitative field constraints on the dynamics of silicic magma chamber rejuvenation and overturn. *Contributions to Mineralogy and Petrology*, 165:1275–1294, 2013.

V. Balaram. Field-portable analytical instruments in mineral exploration: past, present and future. *Journal of Applied Geochemistry*, 19(4):382–399, 2017.

G. W. Bergantz and R. E. Breidenthal. Non-stationary entrainment and tunneling eruptions: A dynamic link between eruption processes and magma mixing. *Geophysical Research Letters*, 28(16):3075–3078, 2001.

M. I. Billen. Modeling the dynamics of subducting slabs. *Annu. Rev. Earth Planet. Sci.*, 36 (1):325–356, 2008.

M. Blum-Oeste and G. Wörner. Central andean magmatism can be constrained by three ubiquitous end-members. *Terra Nova*, 28(6):434–440, 2016.

J. Blundy and B. Wood. Prediction of crystal–melt partition coefficients from elastic moduli. *Nature*, 372(6505):452–454, 1994.

W. A. Bohrson, F. J. Spera, J. S. Heinonen, G. A. Brown, M. A. Scruggs, J. V. Adams, M. K. Takach, G. Zeff, and E. Suikkanen. Diagnosing open-system magmatic processes using the magma chamber simulator (mcs): part i—major elements and phase equilibria. *Contributions to Mineralogy and Petrology*, 175:1–29, 2020.

A. Bollino, A. Regorda, R. Sabadini, and A. M. Marotta. From rifting to oceanization in the gulf of aden: Insights from 2d numerical models. *Tectonophysics*, 838:229483, 2022.

F. O. Boschetty, D. J. Ferguson, J. A. Cortés, E. Morgado, S. K. Ebmeier, D. J. Morgan, J. E. Romero, and C. Silva Parejas. Insights into magma storage beneath a frequently erupting arc volcano (villarrica, chile) from unsupervised machine learning analysis of mineral compositions. *Geochemistry, Geophysics, Geosystems*, 23(4):e2022GC010333, 2022.

P. Bouilhol, V. Magni, J. van Hunen, and L. Kaislaniemi. A numerical approach to melting in warm subduction zones. *Earth and Planetary Science Letters*, 411:37–44, 2015.

N. L. Bowen. *The evolution of the igneous rocks.* Princeton University Press, 1928.

R. M. Bowen. Theory of mixtures. *Continuum physics*, 1976.

B. L. Browne, J. C. Eichelberger, L. C. Patino, T. A. Vogel, J. Dehn, K. Uto, and H. Hoshizumi. Generation of porphyritic and equigranular mafic enclaves during magma recharge events at unzen volcano, japan. *Journal of Petrology*, 47(2):301–328, 2006.

J. Bryant, G. Yogodzinski, M. Hall, J. Lewicki, and D. Bailey. Geochemical constraints on the origin of volcanic rocks from the andean northern volcanic zone, ecuador. *Journal of petrology*, 47(6):1147–1175, 2006.

F. Bucchi, L. E. Lara, and F. Gutiérrez. The carrán–los venados volcanic field and its relationship with coeval and nearby polygenetic volcanism in an intra-arc setting. *Journal of Volcanology and Geothermal Research*, 308:70–81, 2015.

D. H. Burns, S. L. de Silva, F. J. Tepley, and A. K. Schmitt. Chasing the mantle: Deciphering cryptic mantle signals through earth's thickest continental magmatic arc. *Earth and Planetary Science Letters*, 531:115985, 2020.

I. Campbell. Fluid dynamic processes in basaltic magma chambers. In *Developments in petrology*, volume 15, pages 45–76. Elsevier, 1996.

I. H. Campbell and J. Turner. Fountains in magma chambers. *Journal of Petrology*, 30(4): 885–923, 1989.

L. Caricchi and J. Blundy. The temporal evolution of chemical and physical properties of magmatic systems. *Geological Society, London, Special Publications*, 422(1):1–15, 2015.

B. Carrapa, P. G. DeCelles, M. N. Ducea, G. Jepson, A. Osakwe, E. Balgord, A. L. S. Goddard, and L. A. Giambiagi. Estimates of paleo-crustal thickness at cerro aconcagua (southern central andes) from detrital proxy-records: Implications for models of continental arc evolution. *Earth and Planetary Science Letters*, 585:117526, 2022.

K. V. Cashman, R. S. J. Sparks, and J. D. Blundy. Vertically extensive and unstable magmatic systems: a unified view of igneous processes. *Science*, 355(6331):eaag3055, 2017.

B. Charlier, O. Namur, R. Latypov, and C. Tegner. *Layered intrusions*. Springer, 2015.

C. Chelle-Michou and B. Rottier. Transcrustal magmatic controls on the size of porphyry cu systems: State of knowledge and open questions. 2021.

L. Chen, K. Feng, J. Deng, D. Li, S. Li, and I. Somerville. Geochemical comparison between oceanic and continental arc volcanic rocks: Insights to arc magmatism. *Geological Journal*, 59(1):113–136, 2024.

M. A. Clynne. A complex magma mixing origin for rocks erupted in 1915, lassen peak, california. *Journal of Petrology*, 40(1):105–132, 1999.

R. Coats. Magma type and crustal structure in the aleutian arc. *The crust of the Pacific Basin*, 6:92–109, 1962.

D. S. Coleman, W. Gray, and A. F. Glazner. Rethinking the emplacement and evolution of zoned plutons: Geochronologic evidence for incremental assembly of the tuolumne intrusive suite, california. *Geology*, 32(5):433–436, 2004.

E. Contreras-Reyes, D. Díaz, J. P. Bello-González, K. Slezak, B. Potin, D. Comte, A. Maksymowicz, J. Ruiz, A. Osses, and S. Ruiz. Subduction zone fluids and arc magmas conducted by lithospheric deformed regions beneath the central andes. *Scientific Reports*, 11(1):23078, 2021.

J. Cornet, O. Laurent, J.-F. Wotzlaw, M. A. Antonelli, J. Otamendi, G. W. Bergantz, and O. Bachmann. Reworking subducted sediments in arc magmas and the isotopic diversity of the continental crust: the case of the ordovician famatinian crustal section, argentina. *Earth and Planetary Science Letters*, 595:117706, 2022.

R. A. Daly. The nature of volcanic action. In *Proceedings of the American Academy of Arts and Sciences*, volume 47, pages 47–122. JSTOR, 1911.

J. Dannberg and R. Gassmöller. Chemical trends in ocean islands explained by plume–slab interaction. *Proceedings of the National Academy of Sciences*, 115(17):4351–4356, 2018.

J. P. Davidson, L. Font, B. L. Charlier, and F. J. Tepley. Mineral-scale sr isotope variation in plutonic rocks—a tool for unravelling the evolution of magma systems. *Earth and Environmental Science Transactions of the Royal Society of Edinburgh*, 97(4):357–367, 2008.

P. DeCelles, G. Zandt, S. Beck, C. Currie, M. Ducea, P. Kapp, G. Gehrels, B. Carrapa, J. Quade, and L. Schoenbohm. Cyclical orogenic processes in the cenozoic central andes. *Geological Society of America Memoirs*, 212:MWR212–22, 2014.

W. Degruyter and C. Huber. A model for eruption frequency of upper crustal silicic magma chambers. *Earth and Planetary Science Letters*, 403:117–130, 2014.

D. J. DePaolo. Trace element and isotopic effects of combined wallrock assimilation and fractional crystallization. *Earth and planetary science letters*, 53(2):189–202, 1981.

W. R. Dickinson. Relations of andesites, granites, and derivative sandstones to arc-trench tectonics. *Reviews of Geophysics*, 8(4):813–860, 1970.

M. N. Ducea, J. B. Saleeby, and G. Bergantz. The architecture, chemistry, and evolution of continental magmatic arcs. *Annual Review of Earth and Planetary Sciences*, 43:299–331, 2015.

J. Dufek and O. Bachmann. Quantum magmatism: Magmatic compositional gaps generated by melt-crystal dynamics. *Geology*, 38(8):687–690, 2010.

M. Edmonds and P. J. Wallace. Volatiles and exsolved vapor in volcanic systems. *Elements*, 13(1):29–34, 2017.

M. Edmonds and A. W. Woods. Exsolved volatiles in magma reservoirs. *Journal of Volcanology and Geothermal Research*, 368:13–30, 2018.

M. Edmonds, K. V. Cashman, M. Holness, and M. Jackson. Architecture and dynamics of magma reservoirs, 2019.

J. C. Eichelberger. Origin of andesite and dacite: evidence of mixing at glass mountain in california and at other circum-pacific volcanoes. *Geological Society of America Bulletin*, 86 (10):1381–1391, 1975.

A. Fowler. A mathematical model of magma transport in the asthenosphere. *Geophysical & Astrophysical Fluid Dynamics*, 33(1-4):63–96, 1985.

S. Freire, A. J. Florczyk, M. Pesaresi, and R. Sliuzas. An improved global analysis of population distribution in proximity to active volcanoes, 1975–2015. *ISPRS international journal of geo-information*, 8(8):341, 2019.

D. Garg and P. Papale. High-performance computing of 3d magma dynamics, and comparison with 2d simulation results. *Frontiers in Earth Science*, 9:760773, 2022.

D. Garg, P. Papale, S. Colucci, and A. Longo. Long-lived compositional heterogeneities in magma chambers, and implications for volcanic hazard. *Scientific reports*, 9(1):3321, 2019.

S. Geiger, S. Roberts, S. K. Matthäi, C. Zoppou, and A. Burri. Combining finite element and finite volume methods for efficient multiphase flow simulations in highly heterogeneous and structurally complex geologic media. *Geofluids*, 4(4):284–299, 2004.

T. Gerya. Numerical modeling of subduction: State of the art and future directions. *Geosphere*, 18(2):503–561, 2022.

A. F. Glazner. Thermal limitations on incorporation of wall rock into magma. *Geology*, 35(4): 319–322, 2007.

T. H. Green and A. Ringwood. Genesis of the calc-alkaline igneous rock suite. *Contributions to Mineralogy and Petrology*, 18(2):105–162, 1968.

A. G. Grima and T. W. Becker. The role of continental heterogeneity on the evolution of continental plate margin topography at subduction zones. *Earth and Planetary Science Letters*, 642:118856, 2024.

A. G. Grima, C. Lithgow-Bertelloni, and F. Crameri. Orphaning regimes: The missing link between flattened and penetrating slab morphologies. *Frontiers in Earth Science*, 8:374, 2020.

F. Gutiérrez and M. A. Parada. Numerical modeling of time-dependent fluid dynamics and differentiation of a shallow basaltic magma chamber. *Journal of Petrology*, 51(3):731–762, 2010.

C. J. Hawkesworth, B. Dhuime, A. Pietranik, P. A. Cawood, A. I. Kemp, and C. Storey. The generation and evolution of the continental crust. *Journal of the Geological Society*, 167(2): 229–248, 2010.

C. J. Hawkesworth, P. A. Cawood, and B. Dhuime. The evolution of the continental crust and the onset of plate tectonics. *Frontiers in earth science*, 8:326, 2020.

Y. He, Y. Zhou, T. Wen, S. Zhang, F. Huang, X. Zou, X. Ma, and Y. Zhu. A review of machine learning in geochemistry and cosmochemistry: Method improvements and applications. *Applied Geochemistry*, 140:105273, 2022.

J. S. Heinonen, W. A. Bohrson, F. J. Spera, G. A. Brown, M. A. Scruggs, and J. V. Adams. Diagnosing open-system magmatic processes using the magma chamber simulator (mcs): part ii—trace elements and isotopes. *Contributions to Mineralogy and Petrology*, 175:1–21, 2020.

W. Hildreth. Volcanological perspectives on long valley, mammoth mountain, and mono craters: several contiguous but discrete systems. *Journal of Volcanology and Geothermal Research*, 136(3-4):169–198, 2004.

W. Hildreth and S. Moorbath. Crustal contributions to arc magmatism in the andes of central chile. *Contributions to mineralogy and petrology*, 98:455–489, 1988.

X. Hou, Y. He, and B. T. Jones. Recent advances in portable x-ray fluorescence spectrometry. *Applied Spectroscopy Reviews*, 39(1):1–25, 2004.

H. Hu, M. D. Jackson, and J. Blundy. Melting, compaction and reactive flow: controls on melt fraction and composition change in crustal mush reservoirs. *Journal of Petrology*, 63(11): egac097, 2022.

C. Huber, M. Townsend, W. Degruyter, and O. Bachmann. Optimal depth of subvolcanic magma chamber growth controlled by volatiles and crust rheology. *Nature Geoscience*, 12 (9):762–768, 2019.

H. E. Huppert and R. S. J. Sparks. The fluid dynamics of a basaltic magma chamber replenished by influx of hot, dense ultrabasic magma. *Contributions to Mineralogy and Petrology*, 75(3): 279–289, 1981.

H. E. Huppert and R. S. J. Sparks. The generation of granitic magmas by intrusion of basalt into continental crust. *Journal of Petrology*, 29(3):599–624, 1988.

H. E. Huppert and R. S. J. Sparks. Chilled margins in igneous rocks. *Earth and Planetary Science Letters*, 92(3-4):397–405, 1989.

H. E. Huppert and J. S. Turner. A laboratory model of a replenished magma chamber. *Earth and Planetary Science Letters*, 54(1):144–152, 1981.

H. E. Huppert and A. W. Woods. The role of volatiles in magma chamber dynamics. *Nature*, 420(6915):493–495, 2002.

H. E. Huppert, R. Stephen, J. Sparks, and J. S. Turner. Some effects of viscosity on the dynamics of replenished magma chambers. *Journal of Geophysical Research: Solid Earth*, 89 (B8):6857–6877, 1984.

A. Ismail-Zadeh and P. Tackley. *Computational methods for geodynamics*. Cambridge University Press, 2010.

M. Jackson, J. Blundy, and R. Sparks. Chemical differentiation, cold storage and remobilization of magma in the earth's crust. *Nature*, 564(7736):405–409, 2018.

G. Jacques, K. Hoernle, J. Gill, H. Wehrmann, I. Bindeman, and L. E. Lara. Geochemical variations in the central southern volcanic zone, chile (38–43 s): the role of fluids in generating arc magmas. *Chemical Geology*, 371:27–45, 2014.

D. E. James. Plate tectonic model for the evolution of the central andes. *Geological Society of America Bulletin*, 82(12):3325–3346, 1971.

D. E. James. A combined o, sr, nd, and pb isotopic and trace element study of crustal contamination in central andean lavas, i. local geochemical variations. *Earth and Planetary Science Letters*, 57(1):47–62, 1982.

P. A. Jarvis, M. Pistone, A. Secretan, J. D. Blundy, K. V. Cashman, H. M. Mader, and L. P. Baumgartner. Crystal and volatile controls on the mixing and mingling of magmas. *Crustal magmatic system evolution: Anatomy, architecture, and physico-chemical processes*, pages 125–150, 2021.

A. M. Jellinek and D. J. DePaolo. A model for the origin of large silicic magma chambers: precursors of caldera-forming eruptions. *Bulletin of Volcanology*, 65:363–381, 2003.

O. Karakas, W. Degruyter, O. Bachmann, and J. Dufek. Lifetime and size of shallow magma bodies controlled by crustal-scale magmatism. *Nature Geoscience*, 10(6):446–450, 2017.

L. Karlstrom, J. Dufek, and M. Manga. Magma chamber stability in arc and continental crust. *Journal of Volcanology and Geothermal Research*, 190(3-4):249–270, 2010.

A. Karpatne, I. Ebert-Uphoff, S. Ravela, H. A. Babaie, and V. Kumar. Machine learning for the geosciences: Challenges and opportunities. *IEEE Transactions on Knowledge and Data Engineering*, 31(8):1544–1554, 2018.

R. F. Katz. Porosity-driven convection and asymmetry beneath mid-ocean ridges. *Geochemistry, Geophysics, Geosystems*, 11(11), 2010.

T. Keller. From magma chambers to magma oceans: A unified model for the thermo-chemical-mechanical evolution of magma bodies. 2025.

T. Keller and R. F. Katz. The role of volatiles in reactive melt transport in the asthenosphere. *Journal of Petrology*, 57(6):1073–1108, 2016.

T. Keller and J. Suckale. A continuum model of multi-phase reactive transport in igneous systems. *Geophysical Journal International*, 219(1):185–222, 2019.

S. M. Langemeyer, J. P. Lowman, and P. J. Tackley. Global mantle convection models produce transform offsets along divergent plate boundaries. *Communications Earth & Environment*, 2(1):69, 2021.

R. Latypov, S. Chistyakova, and T. Alapieti. Revisiting problem of chilled margins associated with marginal reversals in mafic–ultramafic intrusive bodies. *Lithos*, 99(3-4):178–206, 2007.

J. M. Lees. Seismic tomography of magmatic systems. *Journal of Volcanology and Geothermal Research*, 167(1-4):37–56, 2007.

Y. Li, A. E. Pusok, T. Davis, D. A. May, and R. F. Katz. Continuum approximation of dyking with a theory for poro-viscoelastic–viscoplastic deformation. *Geophysical Journal International*, 234(3):2007–2031, 2023.

D. Liu, Z. Wang, D. Zhao, H. Hu, and R. Gao. Accretionary wedge, arc magmatism and fluid migration in northern sumatra: Insight from seismic attenuation tomography. *Journal of Geophysical Research: Solid Earth*, 129(12):e2024JB029777, 2024.

A. Longo, M. Vassalli, P. Papale, and M. Barsanti. Numerical simulation of convection and mixing in magma chambers replenished with co2-rich magma. *Geophysical research letters*, 33(21), 2006.

A. Longo, P. Papale, M. Vassalli, G. Saccorotti, C. P. Montagna, A. Cassioli, S. Giudice, and E. Boschi. Magma convection and mixing dynamics as a source of ultra-long-period oscillations. *Bulletin of Volcanology*, 74:873–880, 2012.

A. Longo, D. Garg, P. Papale, and C. P. Montagna. Dynamics of magma chamber replenishment under buoyancy and pressure forces. *Journal of Geophysical Research: Solid Earth*, 128(1): e2022JB025316, 2023.

C. Magee, C. T. Stevenson, S. K. Ebmeier, D. Keir, J. O. Hammond, J. H. Gottsmann, K. A. Whaler, N. Schofield, C. A. Jackson, M. S. Petronis, et al. Magma plumbing systems: a geophysical perspective. *Journal of Petrology*, 59(6):1217–1251, 2018.

F. Mallea-Lillo, M. A. Parada, E. Morgado, C. Contreras, and D. Hübner. Contrasting sources and conditions of shallow magmatic reservoirs of the fui group small eruptive centres associated with the liquiñe-ofqui fault zone (chilean andes). *Journal of South American Earth Sciences*, 117:103875, 2022.

B. D. Marsh. On convective style and vigor in sheet-like magma chambers. *Journal of Petrology*, 30(3):479–530, 1989.

B. D. Marsh. Solidification fronts and magmatic evolution. *Mineralogical Magazine*, 60(398): 5–40, 1996.

B. D. Marsh. On some fundamentals of igneous petrology. *Contributions to Mineralogy and Petrology*, 166:665–690, 2013.

P. Martínez, B. S. Singer, H. M. Roa, and B. R. Jicha. Volcanologic and petrologic evolution of antuco-sierra velluda, southern andes, chile. *Journal of Volcanology and Geothermal Research*, 349:392–408, 2018.

F. Marxer, P. Ulmer, and O. Müntener. Polybaric fractional crystallisation of arc magmas: an experimental study simulating trans-crustal magmatic systems. *Contributions to Mineralogy and Petrology*, 177(1):3, 2022.

J. E. Matzel, S. A. Bowring, and R. B. Miller. Time scales of pluton construction at differing crustal levels: Examples from the mount stuart and tenpeak intrusions, north cascades, washington. *Geological Society of America Bulletin*, 118(11-12):1412–1430, 2006.

D. McKenzie. The generation and compaction of partially molten rock. *Journal of petrology*, 25(3):713–765, 1984.

D. P. McKenzie and R. L. Parker. The north pacific: an example of tectonics on a sphere. *Nature*, 216(5122):1276–1280, 1967.

C. R. McKinney, J. M. McCrea, S. Epstein, H. Allen, and H. C. Urey. Improvements in mass spectrometers for the measurement of small differences in isotope abundance ratios. *Review of Scientific Instruments*, 21(8):724–730, 1950.

N. J. McMillan, R. S. Harmon, S. Moorbath, L. Lopez-Escobar, and D. Strong. Crustal sources involved in continental arc magmatism: A case study of volcan mocho-choshuenco, southern chile. *Geology*, 17(12):1152–1156, 1989.

W. Meurer and A. Boudreau. Compaction of igneous cumulates part i: geochemical consequences for cumulates and liquid fractionation trends. *The Journal of Geology*, 106(3): 281–292, 1998.

J. Michel, L. Baumgartner, B. Putlitz, U. Schaltegger, and M. Ovtcharova. Incremental growth of the patagonian torres del paine laccolith over 90 ky. *Geology*, 36(6):459–462, 2008.

J. S. Miller, J. E. Matzel, C. F. Miller, S. D. Burgess, and R. B. Miller. Zircon growth and recycling during the assembly of large, composite arc plutons. *Journal of Volcanology and Geothermal Research*, 167(1-4):282–299, 2007.

G. Moore and I. Carmichael. The hydrous phase equilibria (to 3 kbar) of an andesite and basaltic andesite from western mexico: constraints on water content and conditions of phenocryst growth. *Contributions to Mineralogy and Petrology*, 130(3):304–319, 1998.

E. Morgado, M. Parada, D. Morgan, F. Gutiérrez, A. Castruccio, and C. Contreras. Transient shallow reservoirs beneath small eruptive centres: Constraints from mg-fe interdiffusion in olivine. *Journal of Volcanology and Geothermal Research*, 347:327–336, 2017.

M. L. Myers, D. J. Geist, M. C. Rowe, K. S. Harpp, P. J. Wallace, and J. Dufek. Replenishment of volatile-rich mafic magma into a degassed chamber drives mixing and eruption of tungurahua volcano. *Bulletin of Volcanology*, 76:1–17, 2014.

M. Oeser, R. Dohmen, I. Horn, S. Schuth, and S. Weyer. Processes and time scales of magmatic evolution as revealed by fe–mg chemical and isotopic zoning in natural olivines. *Geochimica et Cosmochimica Acta*, 154:130–150, 2015.

B. Oliveira, J. C. Afonso, S. Zlotnik, and P. Diez. Numerical modelling of multiphase multicomponent reactive transport in the earth's interior. *Geophysical Journal International*, 212 (1):345–388, 2018.

A. Oyarzún, L. E. Lara, and A. Tassara. Decoding the plumbing system of nevados de chillán volcanic complex, southern andes. *Journal of Volcanology and Geothermal Research*, 422: 107455, 2022.

J.-W. Park, I. H. Campbell, M. Chiaradia, H. Hao, and C.-T. Lee. Crustal magmatic controls on the formation of porphyry copper deposits. *Nature Reviews Earth & Environment*, 2(8): 542–557, 2021.

A. Parmigiani, C. Huber, O. Bachmann, and B. Chopard. Pore-scale mass and reactant transport in multiphase porous media flows. *Journal of Fluid Mechanics*, 686:40–76, 2011.

D. Perugini, G. Poli, and R. Mazzuoli. Chaotic advection, fractals and diffusion during mixing of magmas: evidence from lava flows. *Journal of Volcanology and Geothermal Research*, 124 (3-4):255–279, 2003.

D. Perugini, C. P. De Campos, M. Petrelli, and D. B. Dingwell. Concentration variance decay during magma mixing: a volcanic chronometer. *Scientific reports*, 5(1):14225, 2015.

M. Petrelli, L. Caricchi, and D. Perugini. Machine learning thermo-barometry: Application to clinopyroxene-bearing magmas. *Journal of Geophysical Research: Solid Earth*, 125(9): e2020JB020130, 2020.

T. Pettke, F. Oberli, and C. A. Heinrich. The magma and metal source of giant porphyry-type ore deposits, based on lead isotope microanalysis of individual fluid inclusions. *Earth and Planetary Science Letters*, 296(3-4):267–277, 2010.

T. Phemister. The role of water in basaltic magma i. *Zeitschrift für Kristallographie, Mineralogie und Petrographie*, 45:19–77, 1934.

A. R. Philpotts and J. J. Ague. *Principles of igneous and metamorphic petrology.* Cambridge University Press, 2009.

T. Plank and C. H. Langmuir. An evaluation of the global variations in the major element chemistry of arc basalts. *Earth and Planetary Science Letters*, 90(4):349–370, 1988.

T. Plank, K. A. Kelley, M. M. Zimmer, E. H. Hauri, and P. J. Wallace. Why do mafic arc magmas contain 4 wt% water on average? *Earth and Planetary Science Letters*, 364:168–179, 2013.

R.-G. Popa, O. Bachmann, and C. Huber. Explosive or effusive style of volcanic eruption determined by magma storage conditions. *Nature Geoscience*, 14(10):781–786, 2021.

M. Pritchard, S. De Silva, G. Michelfelder, G. Zandt, S. R. McNutt, J. Gottsmann, M. West, J. Blundy, D. Christensen, N. Finnegan, et al. Synthesis: Plutons: Investigating the relationship between pluton growth and volcanism in the central andes. *Geosphere*, 14(3):954–982, 2018.

Z. Qin and J. Suckale. Direct numerical simulations of gas–solid–liquid interactions in dilute fluids. *International Journal of Multiphase Flow*, 96:34–47, 2017.

H. Rawson, T. Keller, K. Fontijn, D. M. Pyle, T. A. Mather, V. C. Smith, and J. A. Naranjo. Compositional variability in mafic arc magmas over short spatial and temporal scales: evidence for the signature of mantle reactive melt channels. *Earth and Planetary Science Letters*, 456:66–77, 2016.

G. Rosenbaum, J. T. Caulfield, T. Ubide, J. F. Ward, D. Sandiford, and M. Sandiford. Spatially and geochemically anomalous arc magmatism: Insights from the andean arc. *Geochemistry, Geophysics, Geosystems*, 22(6):e2021GC009688, 2021.

S. S. Rout, M. Blum-Oeste, and G. Wörner. Long-term temperature cycling in a shallow magma reservoir: insights from sanidine megacrysts at taápaca volcano, central andes. *Journal of Petrology*, 62(9):egab010, 2021.

P. Ruprecht, G. W. Bergantz, and J. Dufek. Modeling of gas-driven magmatic overturn: Tracking of phenocryst dispersal and gathering during magma mixing. *Geochemistry, Geophysics, Geosystems*, 9(7), 2008.

D. Ruscitto, P. Wallace, E. Johnson, A. Kent, and I. Bindeman. Volatile contents of mafic magmas from cinder cones in the central oregon high cascades: Implications for magma formation and mantle conditions in a hot arc. *Earth and Planetary Science Letters*, 298(1-2): 153–161, 2010.

D. M. Ruscitto, P. J. Wallace, L. B. Cooper, and T. Plank. Global variations in h2o/ce: 2. relationships to arc magma geochemistry and volatile fluxes. *Geochemistry, Geophysics, Geosystems*, 13(3), 2012.

N. Sainlot, I. Vlastélic, F. Nauret, S. Moune, and F. Aguilera. Sr–pb isotopes signature of lascar volcano (chile): Insight into contamination of arc magmas ascending through a thick continental crust. *Journal of South American Earth Sciences*, 101:102599, 2020.

P. Samaniego, H. Martin, M. Monzier, C. Robin, M. Fornari, J.-P. Eissen, and J. Cotten. Temporal evolution of magmatism in the northern volcanic zone of the andes: the geology and petrology of cayambe volcanic complex (ecuador). *Journal of petrology*, 46(11):2225–2252, 2005.

H. Schmeling, A. Babeyko, A. Enns, C. Faccenna, F. Funiciello, T. Gerya, G. Golabek, S. Grigull, B. Kaus, G. Morra, et al. A benchmark comparison of spontaneous subduction models—towards a free surface. *Physics of the Earth and Planetary Interiors*, 171(1-4): 198–223, 2008.

B. Schoene, U. Schaltegger, P. Brack, C. Latkoczy, A. Stracke, and D. Günther. Rates of magma differentiation and emplacement in a ballooning pluton recorded by u–pb tims-tea, adamello batholith, italy. *Earth and Planetary Science Letters*, 355:162–173, 2012.

A. Schöpa and C. Annen. The effects of magma flux variations on the formation and lifetime of large silicic magma chambers. *Journal of Geophysical Research: Solid Earth*, 118(3):926–942, 2013.

B. Schurr, G. Asch, A. Rietbrock, R. Trumbull, and C. Haberland. Complex patterns of fluid and melt transport in the central andean subduction zone revealed by attenuation tomography. *Earth and Planetary Science Letters*, 215(1-2):105–119, 2003.

D. R. Scott and D. J. Stevenson. Magma ascent by porous flow. *Journal of Geophysical Research: Solid Earth*, 91(B9):9283–9296, 1986.

Z. Sharp. Principles of stable isotope geochemistry. 2017.

D. N. Shirley. Compaction of igneous cumulates. *The Journal of Geology*, 94(6):795–809, 1986.

R. H. Sillitoe. A plate tectonic model for the origin of porphyry copper deposits. *Economic geology*, 67(2):184–197, 1972.

R. H. Sillitoe. Porphyry copper systems. *Economic geology*, 105(1):3–41, 2010.

D. A. Singer, V. I. Berger, and B. C. Moring. Porphyry copper deposits of the world: Database and grade and tonnage models, 2008. Technical report, US Geological Survey, 2008.

N. H. Sleep. Segregation of magma from a mostly crystalline mush. *Geological Society of America Bulletin*, 85(8):1225–1232, 1974.

J. Solano, M. Jackson, R. Sparks, J. D. Blundy, and C. Annen. Melt segregation in deep crustal hot zones: a mechanism for chemical differentiation, crustal assimilation and the formation of evolved magmas. *Journal of Petrology*, 53(10):1999–2026, 2012.

C. Spandler and C. Pirard. Element recycling from subducting slabs to arc crust: A review. *Lithos*, 170:208–223, 2013.

R. Sparks and L. Marshall. Thermal and mechanical constraints on mixing between mafic and silicic magmas. *Journal of volcanology and Geothermal Research*, 29(1-4):99–124, 1986.

R. Sparks, C. Annen, J. Blundy, K. Cashman, A. Rust, and M. Jackson. Formation and dynamics of magma reservoirs. *Philosophical Transactions of the Royal society A*, 377(2139): 20180019, 2019.

R. S. J. Sparks and H. E. Huppert. Density changes during the fractional crystallization of basaltic magmas: fluid dynamic implications. *Contributions to Mineralogy and Petrology*, 85:300–309, 1984.

R. S. J. Sparks, H. E. Huppert, R. Kerr, D. McKenzie, and S. R. Tait. Postcumulus processes in layered intrusions. *Geological Magazine*, 122(5):555–568, 1985.

F. Spera. Thermal evolution of plutons: a parameterized approach. *Science*, 207(4428):299–301, 1980.

C. Stein, M. Mertens, and U. Hansen. A numerical study of thermal and chemical structures at the core-mantle boundary. *Earth and Planetary Science Letters*, 548:116498, 2020.

K. Stemmer, H. Harder, and U. Hansen. A new method to simulate convection with strongly temperature-and pressure-dependent viscosity in a spherical shell: Applications to the earth's mantle. *Physics of the Earth and Planetary Interiors*, 157(3-4):223–249, 2006.

C. R. Stern. Active andean volcanism: its geologic and tectonic setting. *Revista geológica de Chile*, 31(2):161–206, 2004.

P. J. Tackley, D. J. Stevenson, G. A. Glatzmaier, and G. Schubert. Effects of an endothermic phase transition at 670 km depth in a spherical model of convection in the earth's mantle. *Nature*, 361(6414):699–704, 1993.

Y. Tatsumi and T. Kogiso. The subduction factory: its role in the evolution of the earth's crust and mantle. *Geological Society, London, Special Publications*, 219(1):55–80, 2003.

F. Tepley, J. Davidson, and M. Clynne. Magmatic interactions as recorded in plagioclase phenocrysts of chaos crags, lassen volcanic center, california. *Journal of Petrology*, 40(5): 787–806, 1999.

J. Thomas and A. Sinha. Field, geochemical, and isotopic evidence for magma mixing and assimilation and fractional crystallization processes in the quottoon igneous complex, northwestern british columbia and southeastern alaska. *Canadian Journal of Earth Sciences*, 36 (5):819–831, 1999.

R. Tilling. Volcanism and associated hazards: the andean perspective. *Advances in Geosciences*, 22:125–137, 2009.

A. Toramaru, A. Ishiwatari, M. Matsuzawa, M. Nakamura, and S. Arai. Vesicle layering in solidified intrusive magma bodies: a newly recognized type of igneous structure. *Bulletin of volcanology*, 58:393–400, 1996.

K. Torrance and D. Turcotte. Thermal convection with large viscosity variations. *Journal of Fluid Mechanics*, 47(1):113–125, 1971.

J. Turner and I. Campbell. Convection and mixing in magma chambersearth sci, 1986.

S. J. Turner and C. H. Langmuir. The global chemical systematics of arc front stratovolcanoes: Evaluating the role of crustal processes. *Earth and Planetary Science Letters*, 422:182–193, 2015a.

S. J. Turner and C. H. Langmuir. What processes control the chemical compositions of arc front stratovolcanoes? *Geochemistry, Geophysics, Geosystems*, 16(6):1865–1893, 2015b.

K. Ueki, H. Hino, and T. Kuwatani. Geochemical discrimination and characteristics of magmatic tectonic settings: A machine-learning-based approach. *Geochemistry, Geophysics, Geosystems*, 19(4):1327–1347, 2018.

J. van Hunen and M. B. Allen. Continental collision and slab break-off: A comparison of 3-d numerical models with observations. *Earth and Planetary Science Letters*, 302(1-2):27–37, 2011.

E. A. R. Vera, A. Folguera, G. Z. Valcarce, G. Bottesi, and V. A. Ramos. Structure and development of the andean system between 36 and 39 s. *Journal of Geodynamics*, 73:34–52, 2014.

T. A. Vogel, P. J. Hidalgo, L. Patino, K. S. Tefend, and R. Ehrlich. Evaluation of magma mixing and fractional crystallization using whole-rock chemical analyses: Polytopic vector analyses. *Geochemistry, Geophysics, Geosystems*, 9(4), 2008.

L. Vonopartis, R. Booysen, P. Nex, J. Kinnaird, and L. Robb. Combined satellite and portable xrf exploration mapping of the zaaiplaats tin field, south africa. *South African Journal of Geology 2022*, 125(1):45–60, 2022.

P. J. Wallace, T. Plank, M. Edmonds, and E. H. Hauri. Volatiles in magmas. In *The encyclopedia of volcanoes*, pages 163–183. Elsevier, 2015.

S. F. Watt, D. M. Pyle, T. A. Mather, and J. A. Naranjo. Arc magma compositions controlled by linked thermal and chemical gradients above the subducting slab. *Geophysical Research Letters*, 40(11):2550–2556, 2013.

G. Weber and J. Blundy. A machine learning-based thermobarometer for magmatic liquids. *Journal of Petrology*, 65(4):egae020, 2024.

D. A. White, D. H. Roeder, T. H. Nelson, and J. C. Crowell. Subduction. *Geological Society of America Bulletin*, 81(11):3431–3432, 1970.

Y.-Q. Wong and T. Keller. A unified numerical model for two-phase porous, mush and suspension flow dynamics in magmatic systems. *Geophysical Journal International*, 233(2):769–795, 2023.

A. W. Woods and A. Cowan. Magma mixing triggered during volcanic eruptions. *Earth and Planetary Science Letters*, 288(1-2):132–137, 2009.

G. F. Zellmer, M. Pistone, Y. Iizuka, B. J. Andrews, A. Gómez-Tuena, S. M. Straub, and E. Cottrell. Petrogenesis of antecryst-bearing arc basalts from the trans-mexican volcanic belt: Insights into along-arc variations in magma-mush ponding depths, h2o contents, and surface heat flux. *American Mineralogist*, 101(11):2405–2422, 2016.

P. Zhang and M. S. Miller. Seismic imaging of the subducted australian continental margin beneath timor and the banda arc collision zone. *Geophysical Research Letters*, 48(4): e2020GL089632, 2021.

D. Zhao, J. Wang, Z. Huang, and X. Liu. Seismic structure and subduction dynamics of the western japan arc. *Tectonophysics*, 802:228743, 2021.

M. M. Zimmer, T. Plank, E. H. Hauri, G. M. Yogodzinski, P. Stelling, J. Larsen, B. Singer, B. Jicha, C. Mandeville, and C. J. Nye. The role of water in generating the calc-alkaline trend: new volatile data for aleutian magmas and a new tholeiitic index. *Journal of Petrology*, 51(12):2411–2444, 2010.